DISCLAIMER

U. S. Department of Energy

National Energy Technology Laboratory

Federal Grant #: DE-FE0031912

Report Title: Passive Wireless Sensors for Realtime Temperature and Corrosion Monitoring of Coal Boiler Components Under Flexible Operation

Type of Report: Final Scientific/Technical

Reporting Period Start Date: October 1, 2020

Reporting Period End Date: May 15, 2025

Principal Author(s): Edward M. Sabolsky

Date Report was Issued: August 13, 2025

DOE Award Number: DE-FE0031912

Name and Address of Submitting Organization:

West Virginia University Research Corporation
86 Chestnut Ridge Road
PO Box 6845
Morgantown, WV 26506-6845
Telephone: 304-293-3998
Fax: 304-293-7435

Signature of Submitting Official: Edward M. Sabolsky 8-13-25

ABSTRACT:

Researchers at West Virginia University (WVU) propose to demonstrate inexpensive wireless, high-temperature sensors for real-time monitoring of the temperature and corrosion of metal components, which are commonly used in coal-fired boilers. This study presents the development of cost-effective wireless high-temperature sensors for real-time temperature and corrosion monitoring in coal-fired boilers' metal components. The focus is on fabricating and evaluating chipless radio-frequency identification (RFID) sensors capable of operating between 25-1300 ºC. Efforts were directed towards designing passive RFID sensor and interrogator antenna with a broad frequency range, optimizing a microstrip patch antenna sensor integrated into a "peel-and-stick" format for efficient application to various metal specimens without altering their geometry.

Additionally, this research aimed to assess the sensor responses under accelerated high-temperature conditions, correlating corrosion and cracking mechanisms with sensor data. An investigation of through-wall data acquisition techniques was also planned, facilitating unobtrusive monitoring of sensor responses housed within metal enclosures. Ultimately, this work sought to establish a robust passive wireless sensor system for the continuous health monitoring of metal components in operational settings, thereby contributing to enhanced safety and efficiency in coal-fired power plants.

TABLE OF CONTENTS:

FIGURES LIST:

Task 1 Figures

None

Task 2 Figures

Figure 2.8: (a) 50-120 MHz, (b) 160-180 MHz of ANSYS HFSS simulation results of LC sensor design by varying the relative permittivity of the Al2O3 dielectric layer and Pt conductivity depending on temperature.

Figure 2.9: (a) 50-120 MHz and (b) 160-180 MHz ANSYS HFSS simulation results of LC sensor with an increase in the copper oxide layer between the ground plane and the dielectric layer of the simulation from 25 to 125 μm.

Task 3 Figures

Figure 3.1: Thickness changes of stainless-steel samples after harsh environment exposure on a period of one to five days for one mm samples.

Figure 3.2: Pre corrosion SEM image of 1 mm thick stainless steel sample.

Figure 3.3: Post corrosion SEM image of 1 mm thick stainless steel sample with oxide growth identified in red.

Figure 3.4: Geometry of large three turn and five turn inductors respectively.

Figure 3.5: Geometry of small square inductor and small coiled inductor respectively.

Figure 3.6: Optical images of 5 turn glass ceramic sensor

Figure 3.7: Schematic picture of the boundary conditions for the various EM inputs for the ANSYS simulation model of 5-turn silver inductor printed on alumina with a silver ground plane.

Figure 3.8: Optical image of 5-turn sensor after bonding the Ag inductor pattern onto the Al_2O_3 substrate.

Figure 3.9: Optical image of 5-turn sensor after bonding the Pt inductor pattern onto the Al_2O_3 substrate.

Figure 3.10: Peel and stick process (a) Ag screen printing and acrylic spray coating, (b) Sintered Ag on flat Al_2O_3 substrate.

Figure 3.11: Peel and stick process sintered Ag on curvature Al_2O_3 substrate.

Figure 3.12: Passive wireless sensor heating and cooling furnace results on the Coppers ground plane (Peel and Stick method). (a) The sensor heating stage from room temperature to 800 °C at a rate of 120 °C/h. (b) The sensor maximum temperature hold at 800 °C for 4h. (c) The sensor cooling stage from 800 °C to room temperature at a rate of-120 °C/h

Task 4 Figures

Figure 4.1: 2D illustration of the cuts made on the copper ground planes to evaluate the effects of structural integrity on the ground plane.

Figure 4.2: Arrhenius plot for the oxidation of copper in different temperatures

Figure 4.3: Copper oxide thickness growth obtained in TGA curves during (a) the heating stage from room temperature to 800 °C, and (b) the temperature isothermal hold at 800 °C for 4 h.

Figure 4.4: SEM cross-sectional image of oxide layers on copper oxidized under air atmosphere for 4 h at 800 °C.

Figure 4.5: Arrhenius plot for the oxidation of SS304H in different temperatures

Figure 4.6: SEM cross-sectional image of oxide layers on SS304H oxidized under air atmosphere for 4 h between 950-1050 °C.

Figure 4.7: SEM cross-sectional image of oxide layers on SS304H oxidized under air atmosphere different coating times 4h, 24h, 48h, and 72h at 1000 °C.

Figure 4.8: (a) SEM topographic image of Pt inductor, (b) Cross-sectional SEM image of Pt inductor bonded to alumina substrate.

Figure 4.9: Passive wireless sensor heating and cooling results of the copper ground plane with no surface defects. (a) Sensor data for the heating stage from room temperature to 800 °C at a rate of 120 °C/h. (b) Sensor data at 800 °C isothermal hold for 4 h. (c) Sensor data for the cooling stage from 800 °C to room temperature at a rate of −120 °C/h

Figure 4.10: Passive wireless sensor responses for copper oxidation during the isothermal holding period at 800 °C for ground planes with varying levels of pre-existing surface defects. (a) Ground plane without defects, (b) ground plane with minimal defects, and (c) ground plane with maximum defects.

Figure 4.11: Passive wireless sensor frequency plotted against temperature during the heating and cooling stages of the experiment for ground planes with varying levels of pre-existing surface defects. (a) Ground plane without defects. (b) Ground plane with minimal defects. (c) Ground plane with maximum defects.

Figure 4.12: Passive wireless repeat sensor at low frequency (triple-layer platinum) heating, cooling, and maximum temperature hold furnace results. The top window (a) The multi-sensor response when heated from room temperature to 1000°C at a rate of 120°C/hour with data captured in 30-minute intervals. (b) The multi-sensor response when held at 1000°C for 72 hours with data captured in 20-minute intervals. And (c) The multi-sensor response when cooled from 1000 °C to room temperature at a rate of -120 °C/hour with data captured in 30-minute intervals.

Figure 4.13: Passive wireless repeat sensor at low frequency (triple-layer platinum) heating, cooling, and maximum temperature hold furnace results. The top window (a) The multi-sensor response when heated from room temperature to 1050 °C at a rate of 120°C/hour with data captured in 30-minute intervals. (b) The multi-sensor response when held at 1000°C for 72 hours with data captured in 20-minute intervals. And (c) The multi-sensor response when cooled from 1050 °C to room temperature at a rate of -120 °C/hour with data captured in 30-minute intervals.

Figure 4.14: Passive wireless repeat sensor at high frequency (triple-layer platinum) heating, cooling, and maximum temperature hold furnace results. The top window (a) The multi-sensor

response when heated from room temperature to 900°C at a rate of 120°C/hour with data captured in 30-minute intervals. (b) The multi-sensor response when held at 900°C for 72 hours with data captured in 20-minute intervals. And (c) The multi-sensor response when cooled from 900 °C to room temperature at a rate of -120 °C/hour with data captured in 30-minute intervals.

Figure 4.15: Passive wireless repeat sensor at high frequency (triple-layer platinum) heating, cooling, and maximum temperature hold furnace results. The top window (a) The multi-sensor response when heated from room temperature to 950°C at a rate of 120°C/hour with data captured in 30-minute intervals. (b) The multi-sensor response when held at 950°C for 72 hours with data captured in 20-minute intervals. And (c) The multi-sensor response when cooled from 950 °C to room temperature at a rate of -120 °C/hour with data captured in 30-minute intervals.

Figure 4.16: Passive wireless repeat sensor at high frequency (triple-layer platinum) heating, cooling, and maximum temperature hold furnace results. The top window (a) The multi-sensor response when heated from room temperature to 1000 °C at a rate of 120°C/hour with data captured in 30-minute intervals. (b) The multi-sensor response when held at 1000 °C for 72 hours with data captured in 20-minute intervals. And (c) The multi-sensor response when cooled from 1000 °C to room temperature at a rate of -120 °C/hour with data captured in 30-minute intervals.

Figure 4.17: Passive wireless repeat sensor at high frequency (triple-layer platinum) heating, cooling, and maximum temperature hold furnace results. The top window (a) The multi-sensor response when heated from room temperature to 1050°C at a rate of 120°C/hour with data captured in 30-minute intervals. (b) The multi-sensor response when held at 1050°C for 72 hours with data captured in 20-minute intervals. And (c) The multi-sensor response when cooled from 1050 °C to room temperature at a rate of -120 °C/hour with data captured in 30-minute intervals.

Figure 4.18: (a)–(c): Frequency response of the corrected sensor-only signal during the heating (ramp-up), isothermal hold, and cooling (ramp-down) phases at 1000 °C, (d)–(f): Comparison of the corrected sensor data and sensor + antenna + SS304H response as a function of temperature and time during the respective thermal cycles.

Figure 4.19: Physical layout of the horizontal distance vs. power room temperature experiment

Figure 4.20: Results of the horizontal distance vs. power room temperature experiment. The figure 4.20 on the left shows the frequency response of the experiment, and the figure on the right shows the signal magnitude vs. distance from the sensor**.**

Figure 4.21: Physical layout of the multi-sensor experiments with ground planes.

Figure 4.22: Results of the multi-sensor experiment with ground planes. The blue segment on the left represents shifting the sensor 0-1.5 cm in one direction, and the red segment on the right represents shifting the sensor 0-1.5 cm in the other direction.

Figure 4.23: Physical layout of the multi-sensor experiments with NO ground planes.

Figure 4.24: Results of the multi-sensor experiment with NO ground planes. The top figure represents the sensor reading with one sensor removed at the offset displayed in Figure 4.9, the

middle figure represents the same process with the other sensor, and the bottom figure displays the reading of both the sensors simultaneously.

Figure 4.25: Passive wireless multi-sensor heating, cooling, and maximum temperature hold furnace results. The top window **(a)** The multi-sensor response when heated from room temperature to 800°C at a rate of 120°C/hour with data captured in 30-minute intervals. **(b)** The multi-sensor response when held at 800°C for 4 hours with data captured in 20-minute intervals. And **(c)** The multi-sensor response when cooled from 800°C to room temperature at a rate of -120°C/hour with data captured in 30-minute intervals.

Figure 4.26: Passive wireless sensor heating and cooling furnace results on the stain less steel ground plane. (a) The sensor heating stage from room temperature to 1000 °C at a rate of 120 °C/h. (b) The sensor maximum temperature hold at 1000 °C for 120 h. (c) The sensor cooling stage from 1000 °C to room temperature at a rate of-120 °C/h

Task 5 Figures

Figure 5.1: Background measurement of interrogator antenna with no sensor present.

Figure 5.2: Measured S11 response of LC sensor through air.

Figure 5.3: Measured S11 response of LC sensor through stainless steel.

Figure 5.4 : Measured S11 response of LC sensor through galvanized steel.

Figure 5.5: Measured S11 response of LC sensor through aluminum.

Figure 5.6: ANSYS simulation results of measuring the sensor response with increased thickness of alumina being added to the bottom of the ground plane. The top figure is the frequency response, the middle figure is the magnitude vs. thickness of alumina, and the bottom layer is the frequency vs. thickness of alumina.

Figure 5.7: Experimental results of measuring the sensor response with increased thickness of alumina being added to the bottom of the ground plane. The top figure is the frequency response, the middle figure is the magnitude vs. thickness of alumina, and the bottom layer is the frequency vs. thickness of alumina.

Figure 5.8: Experimental results of testing different metallic barriers obstructing the view of the sensor and the interrogator antenna. The chosen materials were 3.5 mm galvanized steel, 3.35 mm stainless steel, and 0.7 mm aluminum.

Figure 5.9. ANSYS simulation results of the category 1 thin oxide growth on the **through-wall testing environment** ANSYS model (oxidation only on the bottom).

Figure 5.10. ANSYS simulation results of the category 2 thick oxide growth on the **through-wall testing environment** ANSYS model (oxidation only on the bottom).

TABLES LIST:

Task 1 Tables

None

Task 2 Tables

Table 2.2: Parameters of antenna simulation optimization

Table 2.3: The material property values used in the ANSYS simulations represent the different materials utilized in the sensor design. The usage of each material is explained as follows: The sensor was simulated in the following environments: air, copper-ground plane, copper oxide-oxide layer, alumina-dielectric layer, platinum-interrogator antenna, and silver-5-turn inductor.

Task 3 Tables

None

Task 4 Tables

Table 4.1: Calculated oxidation parabolic constants (k") for Cu samples in $g^2\ cm^{-4}\ s^{-1}$.

Table 4.2: Calculated oxidation parabolic constants (k") for SS304H samples in $g^2\ cm^{-4}\ s^{-1}$.

Task 5 Tables

None.

Task6 Tables

None.

EXECUTIVE SUMMARY:

The objective of the work was to demonstrate a wireless, high-temperature sensors for real-time monitoring of the temperature and corrosion of metal components which are commonly used in coal-fired boilers. The work was to focus on fabricating and evaluating chipless radio-frequency identification (RFID) sensors capable of operating at high-temperature. In efforts were to be directed towards designing passive RFID sensor and interrogator antennas with a broad frequency range, optimizing a microstrip patch antenna sensor integrated into a "peel-and-stick" format for efficient application to various metal specimens without altering their geometry. In addition, the research aimed to assess the sensor responses under accelerated high-temperature conditions, correlating corrosion and cracking mechanisms with sensor data. The achievements of the program can be best summarized by reviewing each task in order.

Task 1 was a project management task that possessed no technical milestones/deliverables. In the case of Task 2, passive RFID sensors were to be designed and initial benchtop testing at room temperature were to be completed. Models and simulations were created using ANSYS HFSS Electronics software (Canonsburg, PA, USA). An optimization plan (experimental matrix) was constructed to get the highest performing version of the sensor design. This plan was constructed to create variations of the sensor design (and antennae). Variables included line width, electrode height, line spacing, sensor scale, inductor side number, inductor turn number, electrode composition, and ground plane material. In addition, the antenna design was also evaluated, which included loop diameter, wire thickness, wire length, loop number, and antenna material. A partial factorial experimental matrix was complete for each part of the sensor/antenna combination. The modeling task led to an LC sensor design that centered on a 5-turn square sensor printed on an Al_2O_3 substrate with a resonant frequency centering near 60 MHz. The LC sensor was then computationally modelled at various temperatures (by altering the material properties of the conductor and the dielectric support substrate as a function of temperature), which showed a predictable shift to lower frequencies with an increase in temperature. The modeling was then completed for the same sensor design, where it was set onto a metal ground plate and an oxidation of that plate was represented with an additional layer increasing in thickness between the sensor and the ground plane. An initial ground plane of copper (Cu) was chosen as a surrogate material, since the oxidation of this metal can be completed more rapidly (over high-temperature stainless steels). Later modeling experiments focused on SS304H as the metal of interest for the boiler application. Modelling showed that the oxidation of the base ground metal plate would show a predictable movement of the resonance peak to lower frequencies (with decreased magnitude of the response, with increased oxide growth). In addition, in the design of the sensor for higher temperatures (for the oxidation of the stainless steel), the sensor material printed on the alumina dielectric needed to be replaced by platinum (Pt) over the initial silver (Ag) composition, due to the melting limitation of silver. The modeling results showed that Pt may be applied for this application, but the signal magnitude would be low. The modeling also showed that materials with lower conductivity than Pt (such as the proposed electroceramic materials) would not be applicable for this sensor design (since the conductivity would be too low for optimal signal measurement).

In Task 3 and 4, the LC resonator was successfully manufactured and tested at both room temperature and temperatures up to 1200 °C. The initial sensor that was used to measure the corrosion of the surrogate Cu substrates was fabricated through the screen printing of Ag-based inks on dense polycrystalline Al_2O_3 substrates. The wireless response of the LC was interrogated and received by a radio frequency signal generator and spectrum analyzer at temperatures from 50-800 °C in real-time. The corrosion kinetics of the Cu 110 were characterized through thermogravimetric (TGA) analysis and microscopy images, and the oxide thickness growth was then correlated to the wireless sensor signal under isothermal conditions at 800 °C. The results showed that the wireless signal was consistent with the corrosion kinetics and temperature, indicating that these two characteristics can be further deconvoluted in the future. In addition, the sensor also showed a magnitude- and frequency-dependent response to crack/spallation events in the oxide corrosion layer, permitting in situ wireless identification of these catastrophic events on the metal surface at high temperatures. In addition, a method to print the LC sensor design onto a fugitive wet decal ("peel-and-stick") was developed, and the sensor pattern was successfully transferred to the dielectric substrate and sintered/bonded; the sensor testing showed similar performance as that shown for the screen-printed sensor designs.

After the successful demonstration of the Ag-based sensor on a corroding Cu metal, the Pt-based sensor was fabricated to evaluate its application on the SS304H material. As in the Ag-based sensor, a dense polycrystalline Al_2O_3 substrate was used as the dielectric, and the Pt ink was screen-printed onto the surface to create an inductor-capacitor (LC) resonator sensor (to different thicknesses to optimize the total sensor conductance). The sensor was tested at temperatures between 20 and 1050 °C using a spectrum analyzer. The temperature was limited to 1050 °C, since phase changes in the SS304H would cause excessive spallation, eliminating the ability to sense the oxide growth. As predicted by the computational modeling, the resonant peak was difficult to read due to the high signal-to-noise ratio in the 70-100 MHz range. Interestingly, a secondary peak was identified at a slightly higher level near 160-175 MHz that tracked well with temperature change and stainless-steel oxidation. This band of frequency was used to correlate with the oxidation process for the stainless steel at high temperatures. Similar to previous work, TGA analysis and SEM images were used to investigate the corrosion kinetics of the SS304H stainless steel material, and the measured oxide thickness was then correlated with the wireless sensor signal under isothermal conditions at various temperatures. The work showed that the technology could work as it stands for high-temperature metals above 800 °C, but more work is needed to define a better material system and design that would produce a better signal-to-noise ratio.

In Task 5, experiments to evaluate a method for through-wall signal transmission of the RFID passive wireless sensors were to be tested. Simulated LC sensors were fabricated using a printed circuit board (PCB) purchased from a vendor with the Cu coating. The PCB board was fabricated from FR-4 glass-reinforced epoxy laminate. The same sensor pattern modeled in Task 2 was fabricated through an acid etch process, leaving the Cu sensor pattern on the surface. The sensor was placed within various steel pipes of different diameters and wall thicknesses — specifically 3.5 mm galvanized steel, 3.35 mm stainless steel (both magnetic and non-magnetic), and 0.7 mm aluminum — and the sensor antenna was placed at various distances from the pipe. Although

various publications indicated a very slight measurement of signal, the current work showed a complete absence of detectable resonant peaks through these metallic materials. The findings confirm that metal effectively shields electromagnetic waves, preventing information transfer from the sensor. Despite observing strong responses in air, the sensor's inability to transmit data through various metallic layers underscores the challenges faced in high-temperature applications involving metallic components.

Additional testing included systematic variation of pipe wall thickness and diameter to determine threshold conditions for partial signal penetration. Figures 5.2 through 5.5 illustrate comparative S11 responses for air, thin-walled, and thick-walled metallic enclosures. These results consistently demonstrated that even minimal metallic shielding significantly attenuated the signal, reducing peak magnitude below detectable limits. Control measurements with non-metallic barriers (ceramic tubes and composite sleeves) confirmed that the resonance peak remained stable in magnitude and frequency, indicating that the observed losses were solely due to metallic shielding. The outcomes from Task 5 highlight a critical limitation for deploying passive wireless sensors in enclosed or metallic environments and emphasize the necessity for alternative antenna designs, frequency bands, or coupling strategies to enable reliable through-wall communication in future high-temperature sensor systems.

In Task 6, the goal was to implement the passive wireless sensor array into a demonstration. The original goal was to implement a coal power plant, but due to changes in plant ownership (since the proposal date), and new restrictions after COVID, the ability to find a willing power plant to permit the demonstration was limited. Instead, a surrogate industrial/manufacturing plant was approached to insert our technology, where the plant had many areas that also included high-temperature piping and reactors (Calgon Carbon in Neville Island, PA). A micro-VNA system connected to a miniature microprocessor was developed by the team to be able to read in situ the frequency band of interest. A sensor was installed on a high-temperature stainless steel cyclone reactor, where the internal temperature ranges between 400-800 °C. Issues encountered during the demonstration related to protection against the weather elements and other high temperatures within the local area for the electronics to support the antenna reader. The sensor was permitted to run for a few weeks. Due the above discussed issues, the initial demonstration was shown to be a failure, and the team is waiting for permission to re-enter the plant for another installation within the month of September 2025. The system showed plausible response within a lab setting, so it is expected to work successfully when re-installed within the demonstration plant. Regardless, the technology showed promise, but more work is needed to better connect the sensor to the metal component and a better method to deploy the reader antennae.

REPORT DETAILS

Overall Objectives:

The specific project objectives were as follows:

Researchers at West Virginia University (WVU) aim to demonstrate affordable wireless high-temperature sensors for real-time monitoring of the temperature and corrosion in metal components typically used in coal-fired boilers. The key focus areas of this project include:

Fabrication and Testing: Development and evaluation of harsh-environment, chipless radio-frequency identification (RFID) sensors that operate effectively within a temperature range of 25-1300ºC in high steam and/or flue gas conditions.

Sensor Arrays: Assessment of sensor arrays, where each RFID sensor is specifically engineered to operate within designated frequency bands, enabling spatial differentiation of the testing sites on the metal specimens.

Through-Wall Data Acquisition: Exploration of through-wall data acquisition capabilities, allowing the sensor, housed within a metal tube or enclosure, to transmit its response without the need for drilling access ports.

Sensor Placement Methodology: Development of a "peel-and-stick" method for depositing single or multiple sensors using a decal. This technique will facilitate the economical and precise application of sensors onto components of various shapes and sizes, without disrupting the geometry or functional features of the manufactured item and without requiring removal or decommissioning for installation.

The subsections that will follow will be organized by Task, and the required report content (Introduction, Experimental Methods, Results and Discussion, and Conclusions) will be included with each distinct subsection defined by these tasks. The tasks for this work were as follows:

Task 1: Project Management and Planning

Task 2: Passive RFID Sensor Design and Initial Benchtop Testing

Task 3: Fabrication of Wireless Sensors and Development of Inexpensive Transfer Process

Task 4: Cyclic Passive Wireless Sensor Testing

Task 5: Through-Wall Signal Transmission for RFID Wireless Sensor Testing

Task 6: Implementation of Passive Wireless Sensor Arrays into Power Plant Demonstration

Task 1: Project Management and Planning

1.1 Introduction:

As dictated by the original solicitation, the following was the objective of this task:

"This task shall include all work elements required to maintain and revise the Project Management Plan, and to manage and report on activities in accordance with the plan. It shall also include the necessary activities to ensure coordination and planning of the project with DOE/NETL and other project participants. These shall include, but are not limited to, the submission and approval of required NEPA documentation."

1.2 Experimental Methods:

None

1.3 Results and Discussion:

None

1.4 Conclusions:

As required by the contact, all review meetings, peer-review meetings, and associated documentation (which includes written quarterly reports and the final report) were delivered to DOE in timely manner. The team also completed additional meetings set by the project manager and industrial partner in order to keep close communication between all parties, and to ensure proper planning of all tasks, milestones, and deliverables.

Task 2: Passive RFID Sensor Design and Initial Benchtop Testing

2.1 Introduction:

This project focuses on designing and fabricating advanced signal-processing techniques for passive wireless sensors. Initially, a chipless RFID microstrip patch antenna design will be developed using the ANSYS Maxwell modeling package. The sensor design will investigate how the conductive pattern's geometry and the insulating layer's dielectric properties influence frequency behavior, which is related to temperature variations, corrosion, and corrosion-induced cracking. Following the design phase, sensors will be fabricated using metallic inks on polymer or ceramic substrates. These sensors will be tested under low-temperature conditions inside and outside the proposed metal tubes, examining the effects of magnetic and electric fields. Two main signal processing approaches—non-parametric and parametric—will extract measurement parameters such as temperature, corrosion level, and cracking from the acquired signals. Ultimately, this work aims to lay a crucial foundation for advancements in wireless sensor technologies, and the obtained data will inform future high-temperature testing procedures.This strategy will be discussed further in Subtask 2.1, 2.2 and 2.3.

Subtask 2.1 Passive Wireless Design. The recipient will design appropriate RFID sensor using ANSYS modelling package. The initial sensor design will focus upon the chipless passive RFID esign, where the geometry of the conductive pattern on the specimen and the dielectric properties (and thickness) of the insulating layer will alter the frequency behavior, which is proportional to temperature variation, corrosion, and corrosion induced cracking. Different shapes and/or physical lengths will be evaluated in the modelling, in order to evaluate the backscatter signal and frequency range. The optimal designs will be fabricated and initially tested in Task 2.2 and the passed to Task 3 for actual fabrication.

Subtask 2.2 Wireless Sensor Fabrication on Polymer/Ceramic Substrates and Benchtop Testing. Once the basic sensor designs are modelled, screen/ink-jet printing techniques will be used to fabricate the sensors using metallic (Ag, Pt, etc.) inks on polymer or non-conductive substrates. Both the sensors and interrogator designs will be tested at low temperature (<100°C) both outside and inside the proposed metal tubes. The sensors/antenna pairs will be tested parallel to each other at various lengths, offset distances, and related orientations. Of particular interest will be the impact of the substrate on the magnetic fields (inductive coupling), electric fields (capacitive coupling), and radiofrequency far-field transmissions (RF backscatter coupling) that will be used to send measurement data wirelessly to the receiving device. The data acquired will permit remodeling of the specific sensor/antenna characteristics and will feed into Task 3 fabrication and Task 4 high-temperature, cyclic testing.

Subtask 2.3 Advanced Signal Processing Methods for Deconvoluting the Wireless Response. The best measurement mode for the sensing task will be determined. If frequency response is considered a measurement mode, then the frequency response will be considered function of each

of the measurement parameters, i.e., X(f, t) = g(T, c, s, f, t), where t is the current time, X(f,t) is the frequency response of the sensor at time t and frequency f, T is the current temperature, c is the current corrosion level, and s describes corrosion-induced cracking. The goal will be to measure combinations of c, s, and T using X(f, t). Other measurement modes may also be considered by projecting the received signal onto various basis sets. A mode that provides good discrimination (ability to separate and measure each measurement parameter) will be determined.

2.2 Experimental Methods:

Subtask 2.1 Passive Wireless Design

The foundation of this technology lies in a passive three-layer LC wireless sensor design. This design comprises an upper conductive inductor layer, a middle dielectric layer, and a lower conductive ground plane layer. An interrogator antenna connected to a power source must wirelessly activate the sensor to establish communication with the sensor. Subsequently, the sensor transmits data through inductive coupling. This communication system can be characterized as an RLC circuit. Details are shown in Figure 2.1.

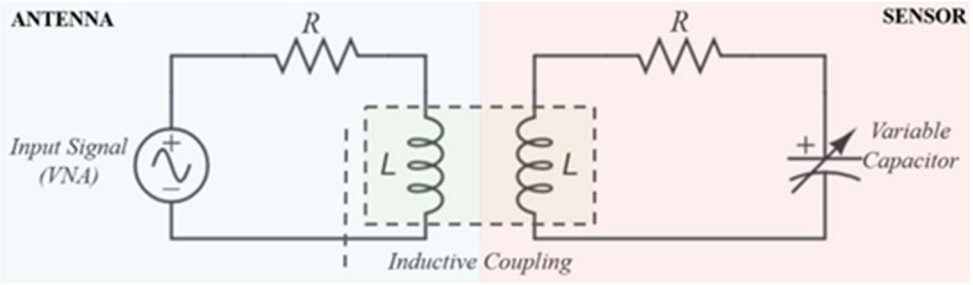

Figure 2.1: Schematic and interaction between the interrogator antenna (left half) and the sensor (right half). The resistance "R" is the resistance embedded in the combined materials.

The top inductor layer of the sensor represents the inductor "L" on the Sensor side of the schematic, while the loop in our loop antenna represents the inductor "L" on the Antenna side of the schematic. Since the sensor has a dielectric layer between the inductor and the ground plane, this system also has an observed capacitance which is represented on the Sensor side of the schematic as the variable capacitor. This sensor design is effective because it represents an RLC circuit, and every RLC circuit has a resonant frequency (f) which is given by [1]:

$$f = \frac{1}{2\pi\sqrt{LC}} \quad (1)$$

In equation 1, the L and C are the inductance and capacitance of the resonator, respectively. Observing changes to this resonant frequency is how changes in temperature and corrosion are communicated. In addition to the resonant frequency, the quality factor Q of the resonator is also a consideration and is given by [1]:

$$Q = \frac{1}{R}\sqrt{\frac{L}{C}} \quad (2)$$

In equation 2, R is the embedded resistance in the resonator materials. A higher quality factor indicates a larger amplitude response when a resonator is coupled by a sinusoidally excited circuit. A higher quality factor also indicates a smaller signal bandwidth. This is ideal for this circuit because a large bandwidth is not necessary when information is communicated by tracking the resonant frequency. Therefore, this circuit is designed to have low resistance and capacitance, and high inductance to maximize the quality factor.

The capacitance generated between the ground plane and the square planar inductor cannot be calculated by the general equation for capacitance between two plates because that assumes each capacitive plate is in a closed circuit. For this sensor, the loop antenna is connected to the vector network analyzer (VNA) through a closed circuit, but neither the inductor nor capacitor is physically connected to the source or the ground. Therefore, they represent floating conductors, and the capacitance seen at the interrogator antenna can be expressed purely as the parasitic capacitance between them. This value is calculated primarily through simulation. Though the capacitance of the sensor cannot be calculated directly using an equation, it is still important to realize that the capacitance of any capacitor is still a function of the relative permittivity, which is the basis of the temperature-sensing ability of the sensor. This equation is given by [2]:

$$C = \frac{\varepsilon_0 \varepsilon_r A}{d} \quad (3)$$

In equation 3, ε_o is the permittivity of free space (8.854×10^{-12} F/m), ε_r is the relative permittivity of the dielectric material, A is the area of the capacitive plates, and d is the distance between the capacitive plates. The inductance is only a factor of the inductor's shape. Therefore, it can be calculated directly. The inductance of the square planar inductor is given by [3]:

$$L = \frac{1.27\mu_0 n^2 \, d_{avg}}{2}\left[\ln\frac{2.07}{\rho} + 0.18\rho + 0.13\rho\right]^{-1} \quad (4)$$

In equation 4, μ_o is the permeability of free space (12.57×10^{-7} H/m), n is the number of turns of the inductor, d_{avg} is the average diameter of the inductor coil, and ρ is the filling ratio which indicates what portion of space within the inductor corresponds to air or coil. d_{avg} is given by [4]:

$$d_{avg} = \frac{d_{in} + d_{out}}{2} \quad (5)$$

n equation 5, d_in is the inner diameter of the inductor, and d_out is the outer diameter of the inductor. The filling ratio ρ is given by [4]:

$$d_{avg} = \frac{d_{out} - d_{in}}{d_{in} + d_{out}} \quad (6)$$

The temperature and corrosion information are both communicated through different means. The sensor resonant frequency is a function of the relative permittivity of the dielectric layer, and this permittivity is a linear function of the temperature of its environment. Therefore, as the temperature increases, there is a direct effect on the resonant frequency of the sensor. The corrosion is communicated by the fact that the dielectric layer's thickness increases as a corrosion layer is added between the dielectric and the ground plane at high temperatures, and the overall dielectric

constant is changed by the mixture between dielectric materials in this layer. The addition of this layer changes the capacitance of the system, and the resonant peak of the sensor is directly affected by the system capacitance as observed in the previous equations.

Subtask 2.2 Wireless Sensor Fabrication on Polymer/Ceramic Substrates and Benchtop Testing.

Sensor models and simulations were performed using ANSYS HFSS Electronics Desktop (Canonsburg, PA, USA), a 3D electromagnetic simulation software integrating ECAD and MCAD modeling. Both low- and high-frequency solvers were used to analyze electromagnetic radiation, surface current distribution, and backscatter behavior. The focus was placed on the S-parameters, particularly S11, which represents the proportion of reflected energy from the sensor port. Simulation-based optimization studies were conducted to identify the most sensitive sensor designs by varying inductor line width, spacing, turn count, and capacitor geometry. Two baseline designs were compared: one incorporating an external capacitor plate in series with the inductor loop, and the other relying solely on inter-turn parasitic capacitance. The sensor performance was assessed under varying conditions of ground plane material (magnetic vs. non-magnetic), geometry, and separation. These parameters influenced field coupling and backscatter response. Furthermore, simulations modeled temperature- and corrosion-induced changes in dielectric thickness and permittivity to assess frequency shifts and amplitude changes in the S11 signal. The sensor design with the highest SNR at resonant frequency was selected for benchtop fabrication and testing using inkjet or screen printing of Ag or Pt-based conductive inks on flexible polymer and rigid ceramic substrates. These sensors were interrogated using a VNA in both free-space and embedded configurations to assess real-world coupling strength and repeatability across various distances and angular offsets.

Subtask 2.3 Advanced Signal Processing Methods for Deconvoluting the Wireless Response.

Signal processing methodology is essential to interpret the multi-parameter dependencies of the resonant response. The sensor's frequency response can be expressed as a function:

$$X(f, t) = g(T, c, s, f, t),$$

where t is the current time, X(f,t) is the frequency response of the sensor at time t and frequency f, T is the current temperature, c is the current corrosion level, and s describes corrosion-induced cracking. The goal will be to measure combinations of c, s, and T using X(f, t). The detailed signal processing methodology used to separate overlapping effects in the frequency domain and isolate individual degradation metrics will be comprehensively described in **Task 4.1**. This will include feature deconvolution and basis projection techniques, enabling robust interpretation of sensor responses even under complex field conditions where multiple environmental and structural variables are active simultaneously.

2.3 Results and Discussion:

Subtask 2.1 Passive Wireless Design and Subtask 2.2 Wireless Sensor Fabrication on Polymer/Ceramic Substrates and Benchtop Testing.

An optimization plan was constructed to get the highest performing version of this new sensor design. This plan was constructed to create variations of the current new design and compare them with each other. Variations that perform better than others would then move on to be modified further. This process is continued through five different matrices of sensor variations. This ultimately yields the highest performing sensors at the end of the five matrices. This process could very simply be thought of as an optimization algorithm with the only difference being, instead of changing a constant variable, each change corresponds to a geometric change of the ANSYS model. A visualization of this process, as well as the examined variations, can be seen in Figure 2.2.

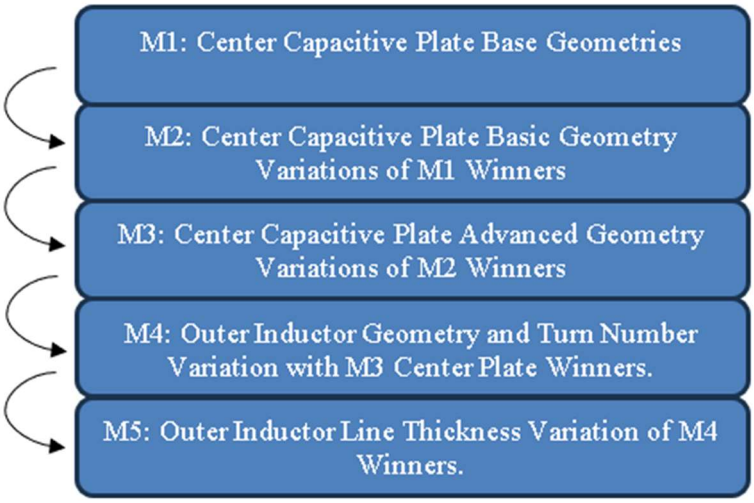

Figure 2.2: Sensor optimization flow diagram.

The initial sensor design to be analyzed features an additional capacitive plate mounted on it. The inductive component, dielectric material, and overall dimensions remain constant during the optimization process. Furthermore, the operating environment is air at room temperature, and the sensor's orientation and the interrogator antenna—an ideal silver loop antenna with a diameter of 52 mm—are also held steady. The only variable in this setup is the capacitive plate's design, which is located at the sensor's center. The constant sensor configuration comprises an alumina substrate supporting a 5-turn silver inductor with a line width of 1.0 mm and a 1.0 mm gap between the lines. The lines are 0.05 mm thick, resting on a square alumina substrate with a side length of 5.11 cm.

The optimization pathway is illustrated on the left side of the accompanying figure, originating with the simulation of various basic geometric shapes, such as circles and squares. The highest-performing geometries from this initial stage are then subjected to further refinement, focusing on aspects like the curvature of shape corners and scaling. This iterative process is depicted in Figure 2.3, which outlines the optimization steps for each sensor design. The sensor design labeled “M1,”

which exhibited a high signal-to-noise ratio (SNR), produced variations that led to the design showcased in column "M2." This iterative design refinement continues until the optimization process's conclusion, resulting in several actual sensor models developed throughout this procedure.

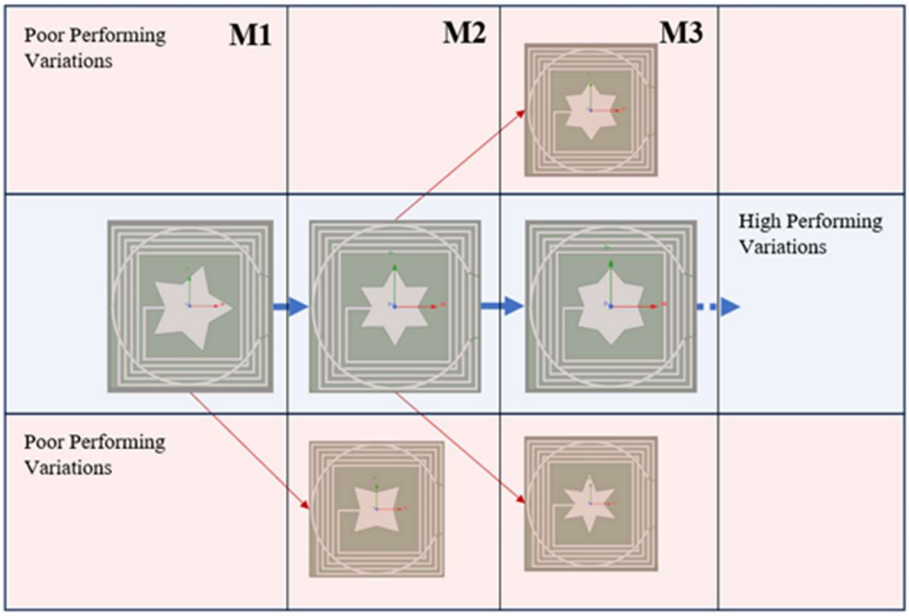

Figure 2.3: Diagram showing how the original sensor design was optimized. The best-performing designs advance to the following level and serve as the foundation for the new designs.

The subsequent optimization process involved refining the sensor's baseline inductor, which does not incorporate a capacitive plate. Table 2.1 comprehensively summarizes the various sensor component variations examined to identify the optimal design. A detailed explanation of this table includes the following components:

- Table 2.1(a) describes the horizontal print width of the inductor lines.
- Table 2.1(b) indicates the thickness of the inductor lines.
- Table 2.1(c) refers to the distance between each adjacent printed inductor line.
- Table 2.1(d) outlines the scale size of the entire sensor, including all components, such as the inductor, dielectric, and ground plane.
- Table 2.1(e) denotes the number of sides of the inductor, with three sides indicating a triangular shape and four sides a square shape.
- Table 2.1(f) specifies the number of turns or loops in the inductor.

Throughout this optimization process, while one parameter was varied according to the specifications in Table 2.1, all other parameters were held constant at predetermined values. Consequently, not every possible combination of variables listed in this table was simulated; each variable was isolated to observe its effect on the sensor's wireless response. Figure 2.4 visually represents several examples of these design variations generated using ANSYS HFSS software.

Table 2.1: Sensor simulation optimization parameters

(a) Line width (mm)	0.4	0.6	0.8	1.0	1.2	1.4	1.6
(b) Electrode height (μm)	20	30	40	50	60	70	80
(c) Line spacing (mm)	0.1	0.4	0.7	1.0	1.3	1.6	1.9
(d) Sensor scale (%)	55	70	85	100	115	130	145
(e) Inductor side number	3	4	5	6	7	8	circle
(f) Inductor turn number	1	2	3	4	5	6	7

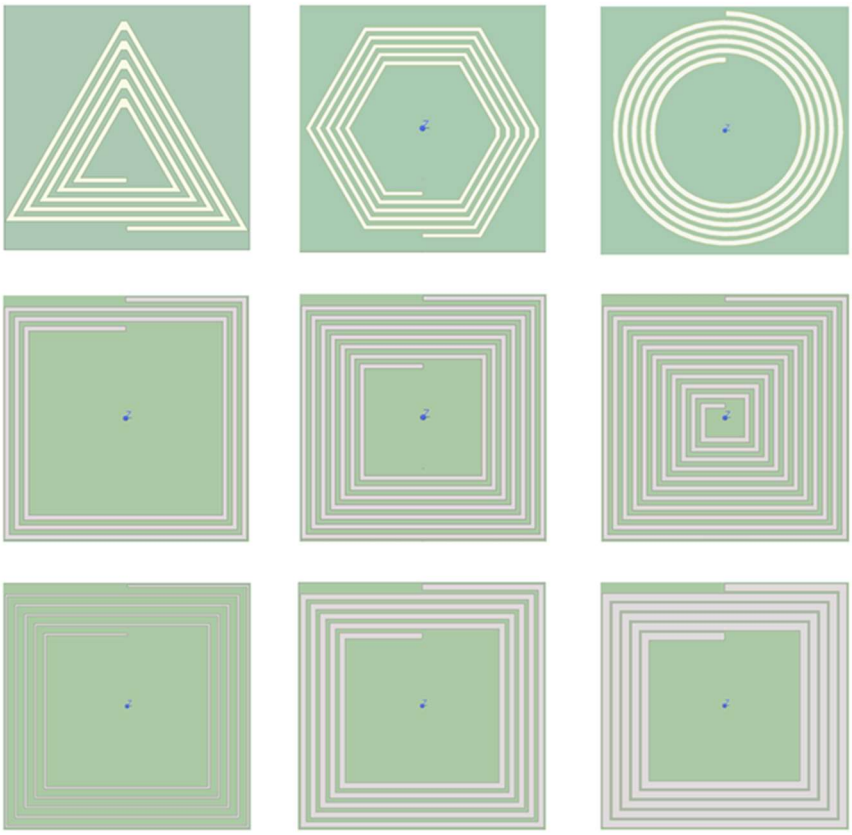

Figure 2.4: Three of the eight sensor variables that were simulated. The sensor counts the inductor's sides (top row), turns (middle row), and line thickness (bottom row). The ANSYS HFSS software was used to create and simulate each model.

Optimization was not limited to the sensors; the antenna was also subjected to a similar process using ANSYS software, followed by experimental validation. The antenna features considered during this optimization are summarized in Table 2.2. Specifically, for the single-loop antenna, the following parameters were simulated: loop diameter, wire thickness, length, and the number of loops. As in previous optimization efforts, while one parameter was adjusted according to the specifications in Table 2.2, all other parameters were maintained at constant values. This approach meant that not every possible combination of the variables listed in the table was simulated; each variable was isolated to examine its impact on performance. Figure 2.5 illustrates several examples of these design variations; all created using the ANSYS HFSS software.

Table 2.2: Parameters of antenna simulation optimization

(a) Loop diameter (mm)	25	35	48	60	70
(b) Wire thickness (mm)	0.1	0.2	0.3	0.4	0.5
(c) Wire length (mm)	5	35	70	105	150
(d) Loop number	1	2	3	4	5

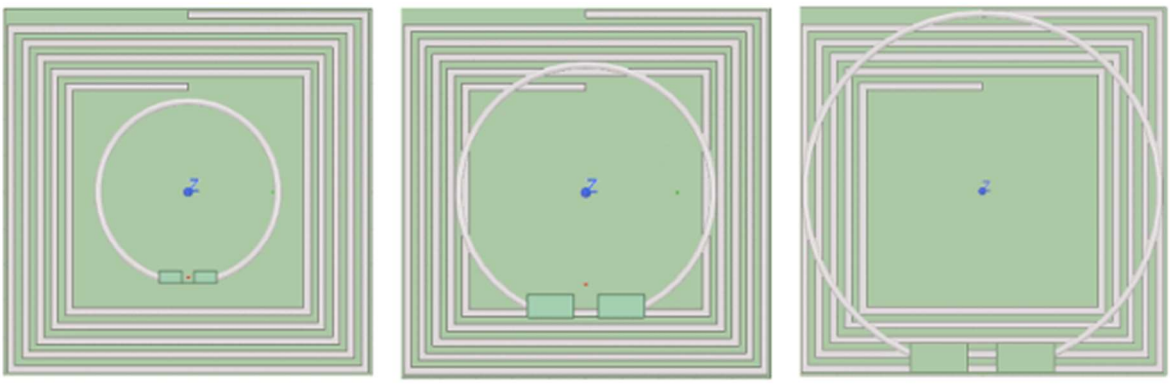

Figure 2.5: One of the four antenna variables that were simulated. Single loop antenna diameters are 25 mm on the left, 35 mm on the middle, and 48 mm on the right. The software ANSYS HFSS was used to create and simulate each model.

After evaluating the sensor and antenna optimization results, the chosen sensor design lacked additive capacitive plating. In contrast, the selected antenna was a single-loop platinum design with a diameter of 52 mm, a thickness of 0.2 mm, and a total length of 18 cm from the SMA connector to the loop. This configuration provided the best sensitivity to temperature and corrosion changes, yielding the most considerable received signal magnitude and significant frequency variations, which linked sensor output to these parameters.

The schematic of the sensor and antenna, modeled to scale in ANSYS, is presented in Figure 2.6. The sensor is a planar inductor, printed on a dielectric substrate, positioned on a corroding metal as the ground plane. The inductor, made of silver (Ag) for its high conductivity, is a square planar coil with five turns, 1 mm line width and spacing, 0.05 mm thickness, and diameters of 3.1 cm and 5.1 cm. This inductor is printed on an alumina (Al_2O_3) substrate measuring 5.11 cm square and 0.5 mm thick, while the ground plane is a copper piece of 7.6 cm square and 1 cm thick.

The system is interrogated via a platinum single-loop antenna connected to an SMA connector with similar diameter and transmission line length specifications. Material properties, including relative permittivity, permeability, and conductivity, are detailed in Table 2.3.

To further explore the impact of the ground plane material on sensor response, simulations were conducted using three materials (copper, aluminum, and stainless steel) at three sizes (2.1 in, 2.5 in, and 3.0 in), all at a uniform thickness of 1.0 cm. The study aimed to understand how different metallic surfaces reflect electromagnetic waves, affecting sensor response while preventing excitation of the sensor itself. The silver single-loop antenna evaluated the sensor's response at a consistent interrogation distance of 0.5 cm.

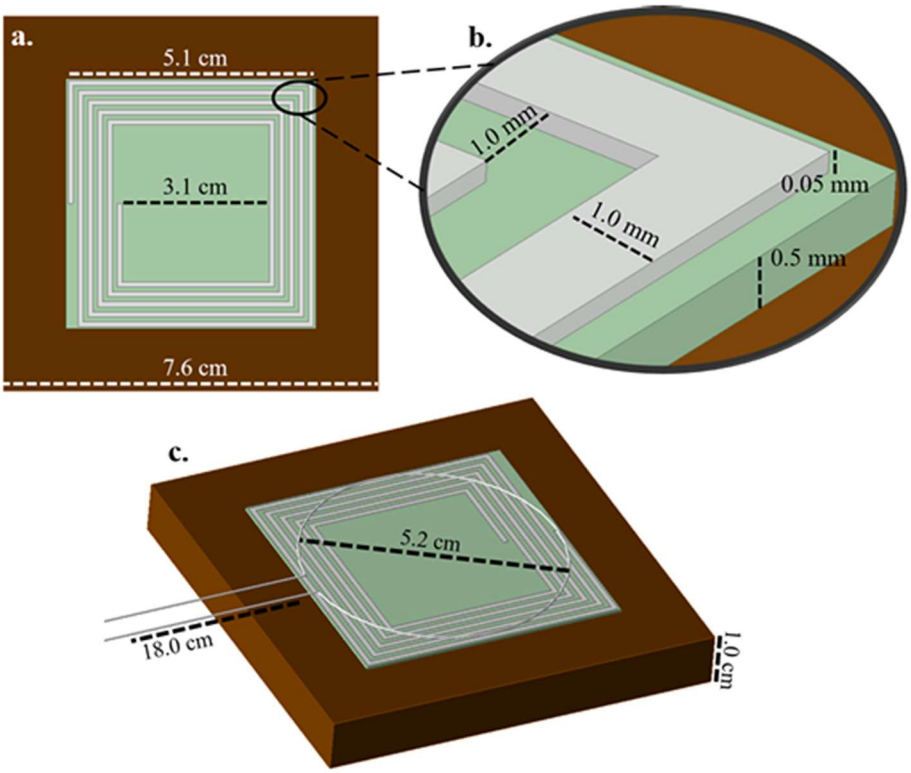

Figure 2.6: The ANSYS HFSS program generates the 3D geometry of the sensor design on a copper ground plane. (a) top-down view of the sensor. (b) A close-up of the printed lines from the sensor. (c) The interrogator loop antenna in the sensor's isometric view.

The sensor geometry was built again in ANSYS HFSS, and the material composition of its layers was given using the material parameters listed in Table 2.3 to model the consequences of raising the temperature of the sensor's environment. After that, the sensor was put into a perfect airbox. The only change was to the dielectric material Al_2O_3's relative permittivity, which was adjusted from 9.8 to 11. The relative permittivity of the material at room temperature and 800 °C is represented by these values, which are displayed in Table 2.3. Figure 2.7(a) shows the sensor's ANSYS HFSS simulation results with the relative permittivity of alumina at 9.8, which corresponds to room temperature alumina, 10.3, which corresponds to 400 °C alumina, and 11, which corresponds to 800 °C alumina. The sensor's resonant frequency dropped from 62 to 55 MHz in an essentially linear connection, with the dielectric material's relative permittivity rising from 9.8 to 11. Equation (3), which demonstrates a proportionate linear relationship between the sensor's capacitance and the dielectric material's relative permittivity, is connected to this and forms the basis of the sensor's temperature-sensing capability. Along with the frequency shift, there is a minor attenuation (reduction in magnitude) in the frequency response's magnitude. Since capacitance is directly correlated with the quality factor, which is inversely proportional to capacitance and provided in Equation (4), this results from the system's changed capacitance. This outcome served as the basis for the sensor's temperature sensing theory and a means of verifying the sensor's experimental performance.

A homogeneous layer of copper oxide (CuO) was added between the ground plane and the sensor's alumina dielectric to simulate the impact of oxidation on the ground plane. This layer displayed a varied thickness but was the same length and width as the ground plane (7.6 cm × 7.6 cm). These preliminary calculations at 800 °C for 4 hours suggested a maximum copper oxide layer of 170 μm. This was determined through the corrosion kinetics borrowed from the literature initially [6]. This oxidation layer was added to the sensor at a minimum of 5 μm and was increased over seven increments to a maximum thickness of 170 μm. The results of this increasing thickness are observed in Figure 2.7(b), which shows the ANSYS HFSS simulation results of the sensor with increasing copper oxide layer thickness. The frequency changed from 61 MHz to around 52 MHz, and the S11 response's magnitude rose from −2.5 dB to −4.25 dB as the copper oxide layer's thickness increased. The relationship between these two parameters and the oxidation thickness is almost linear. The oxidation layer on the sensor's ground plane has a trackable relationship with the frequency and magnitude of the S11 response, as seen by this simulation, which also depicts the sensor's physical properties during the maximum temperature hold. This results shows that the growth of CuO layer on the Cu plate could be accurately tracked using the Ag-based 5-turn surface-printed inductor on the alumina substrate. The fabrication and testing of this type of sensor will be further discussed in Task 3 and 4 discussion below.

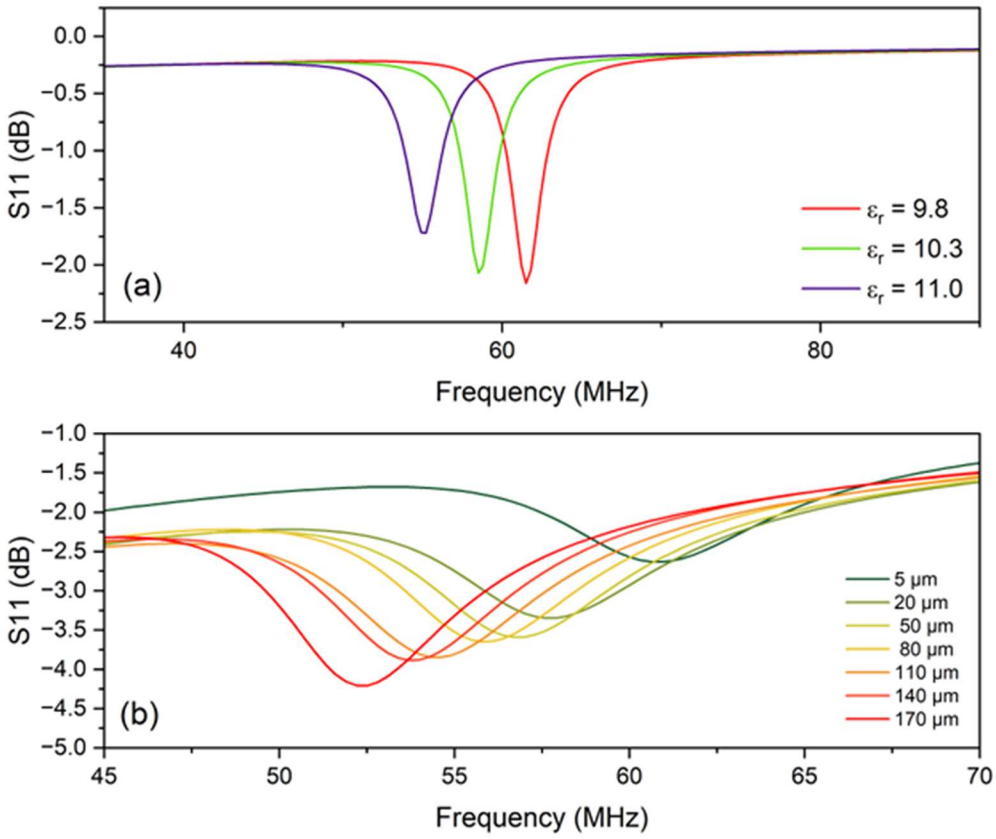

Figure 2.7: (**a**) ANSYS HFSS simulation results of LC sensor design by varying the relative permittivity of the Al_2O_3 dielectric layer from 9.8 to 11. (**b**) ANSYS HFSS simulation results of of LC sensor with increasing the copper oxide layer between the ground plane and the dielectric layer of the simulation from 5-170 µm

The temperature-dependent electromagnetic response of a sensor with a 5-turn platinum antenna was investigated using ANSYS HFSS simulations over two frequency ranges: Figure 2.8 shows the results of (a) 50–120 MHz and (b) 160–180 MHz. Simulations were conducted at 25°C, 400°C, 800°C, and 1000°C by adjusting the Al_2O_3 dielectric constant (9.8 to 11.4) and Pt conductivity (9.30×10^6 to 6.90×10^6 S/m) to reflect thermal effects. Results indicated a clear resonance frequency shift from ~62.5 MHz to ~57.5 MHz in the 50–120 MHz range as temperature increased, attributed to enhanced dielectric permittivity and thus increased system capacitance. Despite reduced conductivity leading to higher losses, a modest increase (~0.08 dB) in signal amplitude was observed, likely due to improved coupling at lower resonance frequencies. No distinct resonance behavior was detected in the 160–180 MHz band across the temperature range.

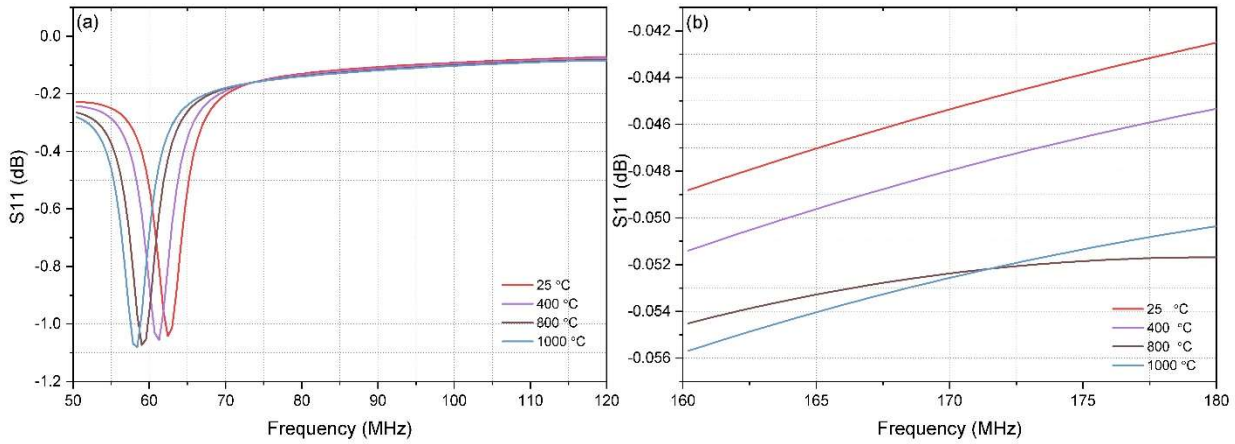

Figure 2.8: (a) 50-120 MHz, (b) 160-180 MHz of ANSYS HFSS simulation results of LC sensor design by varying the relative permittivity of the Al_2O_3 dielectric layer and Pt conductivity depending on temperature.

The influence of oxidation on sensor response was simulated by introducing a homogeneous Fe_2O_3 layer of varying thickness (25–125 µm) between the alumina dielectric and the SS304H ground plane, maintaining a fixed lateral dimension of 7.6 cm × 7.6 cm. Figure 2.9 shows the results of (a) 50–120 MHz and (b) 160–180 MHz. ANSYS HFSS simulations revealed a progressive downshift in resonance frequency from ~60 MHz to ~57.5 MHz within the 50–120 MHz band as oxide thickness increased, attributed to added dielectric loading from the Fe_2O_3 layer. This layer also caused signal attenuation, with amplitude decreasing from −2.6 dB to −3.1 dB, due to heightened dielectric losses and diminished coupling efficiency. No notable resonance behavior was observed in the 160–180 MHz range.

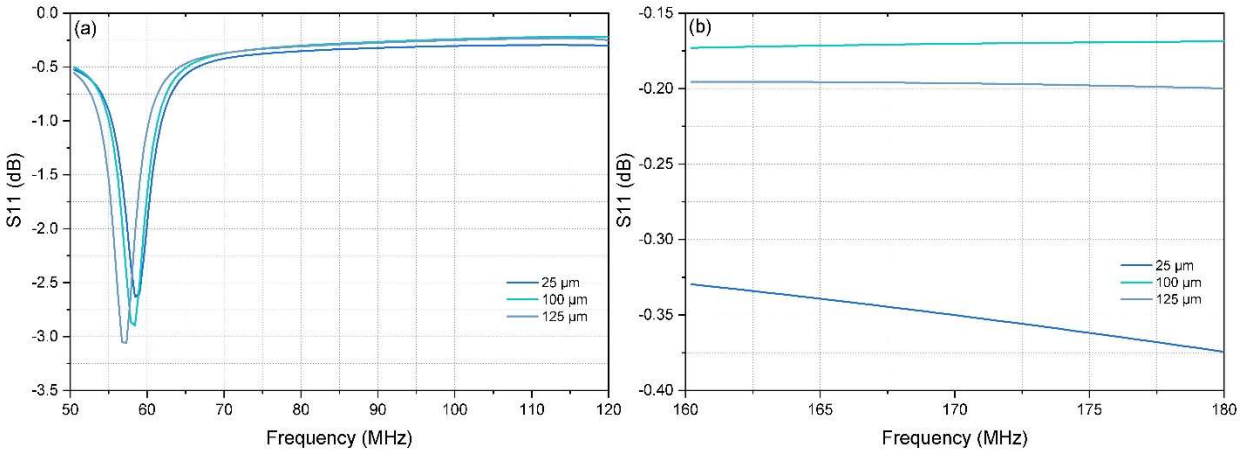

Figure 2.9: (a) 50-120 MHz and (b) 160-180 MHz ANSYS HFSS simulation results of LC sensor with an increase in the copper oxide layer between the ground plane and the dielectric layer of the simulation from 25 to 125 µm.

Table 2.3: The material property values used in the ANSYS simulations represent the different materials utilized in the sensor design. The usage of each material is explained as follows: The sensor was simulated in the following environments: air, copper-ground plane, copper oxide-oxide layer, alumina-dielectric layer, platinum-interrogator antenna, and silver-5-turn inductor [6-9].

Material	Permittivity	Permeability	Conductivity
Silver	1	0.99998	6.10E+07
Air	1.0006	1	0
Stainless Steel 304H	1	1	1.10E+06
Fe_2O_3	1.54	1	8.72E-04
Platinum – 25 °C	1	1	9.30E+06
Platinum - 400 °C	1	1	8.26E+06
Platinum - 800 °C	1	1	7.30E+06
Platinum - 1000 °C	1	1	6.90E+06
Al_2O_3 – 25 °C	9.8	1	1.00E-04
Al_2O_3 – 400 °C	10.3	1	1.00E-04
Al_2O_3 – 800 °C	11	1	1.00E-04
Al_2O_3 – 1000 °C	11.4	1	1.00E-04
Copper	1.000	0.999	5.8106
Copper Oxide	12.00	1.0	1

Material	Permittivity	Permeability	Conductivity
Silver	1	0.99998	6.10E+07
Air	1.0006	1	0
Stainless Steel 304H	1	1	1.10E+06
Fe2O3	1.54	1	8.72E-04
Platinum – 25 °C	1	1	9.30E+06
Platinum - 400 °C	1	1	8.26E+06
Platinum - 800 °C	1	1	7.30E+06
Platinum - 1000 °C	1	1	6.90E+06
Al2O3 – 25 °C	9.8	1	1.00E-04
Al2O3 – 400 °C	10.3	1	1.00E-04
Al2O3 – 800 °C	11	1	1.00E-04
Al2O3 – 1000 °C	11.4	1	1.00E-04
Copper	1.000	0.999	5.8106
Copper Oxide	12.00	1.0	1
Alumina (25 °C)	9.800	1.000	110-4
Alumina (800 °C)	11.00	1.000	110-4

Copper was used as the original ground, and the target corroding material, so that a surrogate metal that oxidizes quite readily could be used to prove out the technology. In the case of high-temperature metals, such as SS304H, the oxidation kinetics is quite slow and the available test time would limit the team's ability to demonstrate the technology multiple times over the project period. The team thought that copper would be the perfect surrogate to develop the technology

due to it fast oxidation kinetic, which is well-documented in published literature. After the Cu modeling was completed, then modeling was then focused upon SS304H metal as the ground plane.

Subtask 2.3 Advanced Signal Processing Methods for Deconvoluting the Wireless Response.

In this task, the foundational parameters influencing the sensor's frequency response—namely temperature variation, corrosion progression, and corrosion-induced cracking—were conceptually defined as components contributing to a complex, multi-variable signal profile. Although the physical sensor design and benchtop characterization were emphasized in Subtasks 2.1 and 2.2, the analytical techniques required to deconvolute overlapping signal effects and isolate individual degradation modes remain essential to ensure robust sensor interpretation in practical environments.

The detailed methodology for signal deconvolution, including the mathematical framework, feature extraction, and transformation-based approaches (e.g., basis projection), will be comprehensively addressed in Task 4.1. This subsequent section will outline how these methods are applied to discriminate between temperature effects, oxide growth, and structural damage signatures, thereby enabling accurate mapping of sensor outputs to specific degradation mechanisms.

2.4 Conclusions:

This study presents a novel LC-based passive wireless sensor system designed for the simultaneous monitoring of temperature, oxidation, and structural degradation in high-temperature environments. Through comprehensive parametric optimization and electromagnetic modeling using ANSYS HFSS, the sensor geometry and materials were refined to enhance sensitivity and signal stability across a broad operating range.

Simulation and experimental findings confirmed that both temperature and oxide layer growth significantly influence the sensor's resonant frequency. Specifically, temperature-induced changes in the dielectric constant of the Al_2O_3 substrate and the electrical conductivity of the Pt antenna were found to lower the resonance frequency from approximately 62.5 MHz at 25 °C to 57.5 MHz at 1000 °C. Similarly, the addition of a Fe_2O_3 oxidation layer between the dielectric and ground plane produced a measurable frequency shift—decreasing from ~60 MHz to 57.5 MHz—as the oxide thickness increased from 25 to 125 µm. These results validated the sensor's dual sensitivity to both temperature and corrosion effects.

Experimental evaluations further demonstrated the sensor's robustness under controlled thermal and environmental conditions. The device achieved a temperature sensitivity of approximately 0.013 MHz/°C between 25 °C and 800 °C, and a corrosion sensitivity of ~0.05 MHz/µm across oxide growth up to 170 µm. Additionally, the signal amplitude remained sufficiently strong to preserve a discernible resonance peak despite increasing dielectric losses at elevated temperatures.

Two sensing strategies were evaluated: a single-sensor system and a distributed multi-sensor model. The multi-sensor configuration provided redundancy and improved accuracy in temperature tracking, while also aiding in the separation of oxidation-induced responses from

thermal effects. This approach enhances the reliability of real-time diagnostics in complex environments.

Collectively, the outcomes of Task 2 establish the feasibility and performance potential of the proposed LC sensor design. These findings lay the groundwork for subsequent tasks focused on sensor fabrication (Task 3) and advanced signal processing (Task 4), where real-world implementation and response deconvolution will be further explored.

Task 3: Fabrication of Wireless Sensors and Development of Inexpensive Transfer Process

3.1 Introduction:

This section investigates various material systems, including refractory metals, electroceramic oxides, and ceramic composites, within a temperature range of 500°-1300°C, varying humidity levels, and system pressure conditions. The material systems will be evaluated based on their electrical conductivity, corrosion resistance, chemical and thermal stability, and susceptibility to temperature, electric, and magnetic fields. The proposed sensor design would be fabricated onto a planar metal/ceramic substrate using materials chosen from Subtask 3.1. Printable inks would be developed to meet permissible surface tension and viscosity levels, with varying solid loadings of metal/ceramic particles synthesized and controlled for viscosity. Initial substrates will include metals coated with insulating barrier layers, ceramic wafers representing insulating surfaces, and organic films with polymer binder coatings for "peel-and-stick" technology. Electrical performance testing of sensors transferred onto metal tubing will be conducted at >500 °C in varying atmospheres, following ASTM standards for precision and quality assurance. The specific subtasks were as follows.

Subtask 3.1 Investigation of Various Material Systems for the Wireless Sensor Fabrication

Material systems were characterized to fabricate the sensor design on the dielectric material. The material systems that shows high electrical conductivity, good corrosion resistance, better chemical and thermal stability, and low electric and magnetic susceptibility will be chosen for further fabrication of the wireless sensor in Subtask 3.2.

Subtask 3.2 Fabrication of RFID and Patch Antenna Sensors Directly onto Planar Metal/Ceramic Substrates.

The sensor design proposed in Task 2 would be fabricated onto a planar metal/ceramic substrate with the materials system chosen from Subtask 3.1. Patterning and deposition techniques will be investigated based on the geometrical form factor of the sensor/arrays. Printable inks will be fabricated within a permissible surface tension and viscosity level required for printing. Inks at various solid loadings (metal/ceramic particles) will be synthesized, and viscosity will be controlled (by solvent or binder content). Initial substrates will include metal coated with an insulating barrier layer, ceramic wafers (to represent insulating-barrier coating surfaces) and the organic films (with the various polymer binder coatings that will be used for the transfer decal paper) for the "peel-and-stick" technology (see Subtask 3.3).

Subtask 3.3 Development of Inexpensive Transfer Process and Baseline Testing

The designs and fabrication process developed in Subtask 3.1 will be used in this task. This subtask will investigate methods to transfer the sensor to the active energy system component. The work

will investigate (but not be limited to): the effect of ink/paste characteristics on wetting and transfer of the patterns, organic overlay effect on "sticking" to metal surfaces, pyrolysis of fugitive under- and over-lay coatings, bonding of print after carrier pyrolysis.

Subtask 3.4: Direct Transfer of Sensor to Metal Tubing and Thermal Processing Development.

Three initial sensor configurations (without a passive communication circuit) will be designed, with focus on temperature, corrosion, and corrosion crack tests. The electrical performance testing of the sensors directly transferred on metal tubing via decal transfer process will be completed at 500°-1300°C in varying atmospheres in WVU's existing automated sensor test stands. Baseline electrical performance will be assessed, and the optimized designs will be completed and combined with the sensor in Subtask 5.1.

3.2 Experimental Methods:

3.2.1 Investigation of Various Material Systems for the Wireless Sensor Fabrication.

In accordance with Subtask 3.1, a systematic evaluation of candidate material systems was conducted to enable the fabrication of wireless sensors on dielectric substrates for high-temperature applications. The experimental focus was placed on materials exhibiting high electrical conductivity, robust corrosion resistance, superior thermal and chemical stability, and minimal electric and magnetic susceptibility.

Several classes of materials, including refractory metals, electroceramic oxides, and ceramic composites, were subjected to thermal exposure and corrosion testing. Stainless steel samples with thicknesses of 1 mm, 0.5 mm, and 0.25 mm were selected and subjected to oxidation environments. Each sample was placed in a ceramic crucible and heated in ambient air at a rate of 2 °C/min to a setpoint of 600 °C. Exposure durations ranged from one to five days.

Post-exposure characterization was carried out using scanning electron microscopy (SEM). Prior to imaging, the samples were polished to ensure clear visualization of the oxide layer interfaces. To reduce measurement uncertainty, image contrast and brightness were adjusted, and oxide thicknesses were quantified using ImageJ software. The use of thinner steel coupons facilitated higher SEM magnification and improved boundary resolution. A consistent oxide growth trend was observed, with the 1 mm thick samples demonstrating approximately 30 µm of oxide layer formation per 24 hours.

In parallel, fabrication parameters were optimized for the deposition of conductive sensor patterns. Direct ink writing and RF sputtering techniques were employed to print various inductor geometries—specifically, large three-turn and five-turn square inductors, as well as smaller configurations such as miniaturized square and coiled inductors. Due to equipment limitations, thin-film deposition methods were adapted for smaller geometries. The resulting reduction in inductor size produced a corresponding upshift in the resonant frequency, transitioning from the 40–200 MHz range to 1.4–3.4 GHz.

Silver-based inkjet inks were used for patterning the sensor geometries. These inks were selected due to their high conductivity and compatibility with ceramic and polymer substrates. However, limitations in film uniformity at large sizes led to the adaptation of thin-film alternatives for certain geometries.

All experiments were conducted under strictly controlled conditions, and the selection of material systems was guided exclusively by their electrical, thermal, and corrosion performance metrics, in full alignment with the objectives set forth in Subtask 3.1.

3.2.2 Fabrication of RFID Sensors Directly onto Planar Substrates.

The sensors were fabricated using dense alumina (Al_2O_3) substrates (96% purity, MTI Corporation, Richmond, CA, USA) and Ag-based inks and a purity level of 96%, sourced from MTI Corporation in Richmond, CA, USA, in conjunction with Platinum (Pt) based inks. The Ag ink was synthesized by using two Ag powders purchased from Beantown Chemical (Hudson, NH 03051, USA). The fine Ag particle size was 0.7–1.3 μm (99.9% purity, Lot#D06W05), and the coarse Ag particle size was 3–7 μm (99.9% purity, Lot#N01D020); both powders were used as received from the manufacturer. The Ag ink was formulated with fine and coarse Ag powders with a 1:4 ratio, respectively. The Ag powder and Pt powder mix was then dispersed into a Johnson Matthey ethyl cellulose and terpineol organic vehicle (Johnson Matthey, Smithfield, PA, USA), and two drops of fish oil (Tape Casting Warehouse, Morrisville, PA, USA) were added to aid in dispersion. The total mixture was then sonicated for 2 min. The LC sensors were then fabricated via a screen-printing process. A 230-mesh screen with our LC design was purchased from UTZ Technologies (Little Falls, NJ, USA). The fully printed sensor was then sintered in a box furnace (Sentry Xpress 4.0, Paragon Industries L.P., Mesquite, TX, USA) in ambient air.

3.2.3 Development of Inexpensive Transfer Process and Baseline Testing.

The sensor transfer process was carried out using a custom-developed ceramic decal transfer method. Initially, a conductive silver (Ag) ink was deposited onto the glossy side of a ceramic transfer paper via screen printing. The printed decal was then dried on a hot plate at a low temperature of 90 °C for 5 minutes to ensure solvent evaporation and adequate film formation. Following the drying process, an acrylic protective coating (Model #: K01303007, Krylon, Cleveland, OH, USA) was applied uniformly over the printed pattern to prevent deformation during the transfer. The acrylic spray was applied for 15–20 seconds, with careful attention to overlapping each pass. The coating procedure was repeated twice, allowing sufficient drying time between applications to ensure film integrity and adhesion. After preparation, the decal paper was immersed in deionized water to activate the release layer, allowing for the transfer of the printed pattern onto a planar Al_2O_3 ceramic substrate. The transferred sensor was aligned manually to maintain design fidelity. To improve adhesion and eliminate voids or air gaps, a vacuum-assisted technique was employed following transfer. Alternatively, a controlled sintering process was applied to achieve stable bonding and organic removal, using a heating schedule of 2 °C/min up to 750 °C with a 2-hour dwell, followed by cooling at the same rate. This method demonstrated successful pattern transfer onto a planar ceramic surface and will serve as a baseline for comparison with sensors fabricated directly via screen printing. In subsequent experiments, the applicability of this method to curved surfaces will also be explored.

3.2.4: Direct Transfer of Sensor to Metal Tubing and Thermal Processing Development.

The transfer process utilized in this task follows the same methodology previously developed and implemented in Subtask 3.2.3. Specifically, a ceramic decal transfer technique was employed to pattern conductive silver (Ag) ink onto a ceramic substrate. Initially, Ag ink was screen-printed onto the glossy side of a ceramic decal paper, followed by drying on a hot plate at 90 °C for 5 minutes to ensure proper solvent removal and film stabilization. A protective acrylic overlay (Krylon, Model #: K01303007, Cleveland, OH, USA) was then applied over the printed pattern to maintain design integrity during transfer. The coating was applied in two successive passes, each lasting 15–20 seconds, with appropriate drying intervals. The decal paper was subsequently soaked in deionized water to release the printed layer, which was then carefully transferred onto the ceramic substrate. Unlike the previous implementation on flat Al_2O_3 surfaces in Subtask 3.2.3, this procedure was adapted for application onto a curved Al_2O_3 surface. To facilitate conformal contact with the curvature, manual alignment was performed, followed by vacuum assistance to improve adhesion. Post-transfer, a controlled sintering cycle was applied (2 °C/min ramp to 750 °C, 2-hour dwell, and symmetric cooling) to remove organic layers and ensure robust bonding of the conductive pattern to the curved ceramic surface. This experimental step aims to validate the feasibility of transferring complex sensor designs onto non-planar substrates, advancing the sensor integration process for real-world curved components in energy systems.

3.3 Results and Discussion:

3.3.1 Investigation of Various Material Systems for the Wireless Sensor Fabrication.

The oxidation experiments revealed a clear linear correlation between exposure time and oxide layer thickness for stainless steel at 600 °C. SEM images taken before and after corrosion exposure confirmed progressive material degradation and oxide scale formation. As demonstrated in the quantitative analysis, an average of 30 μm of steel loss per day was recorded for the 1 mm samples. The improved accuracy resulting from enhanced image processing and reduced sample dimensions allowed for the elimination of the inconsistencies observed in earlier measurements.

Figure 3.1 demonstrates the measured steel thickness loss over a 5-day exposure period at 600 °C. The data exhibit a linear trend, indicating a consistent oxidation rate of approximately 30 μm per 24 hours for the 1 mm samples.

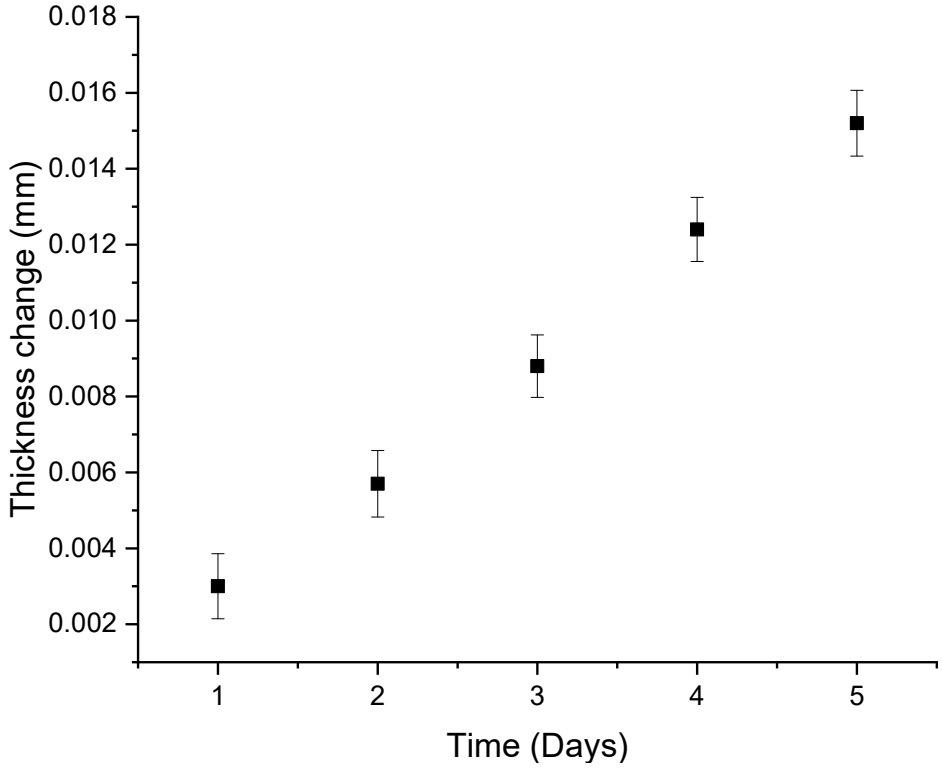

Figure 3.1: Thickness changes of stainless-steel samples after harsh environment exposure on a period of one to five days for one mm samples.

Figures 3.2 and 3.3 compare pre- and post-corrosion SEM images of the 1 mm stainless steel samples. In the post-corrosion image (Figure 3.1.4), the oxide growth region is distinctly highlighted in red, which facilitated quantitative analysis via ImageJ.

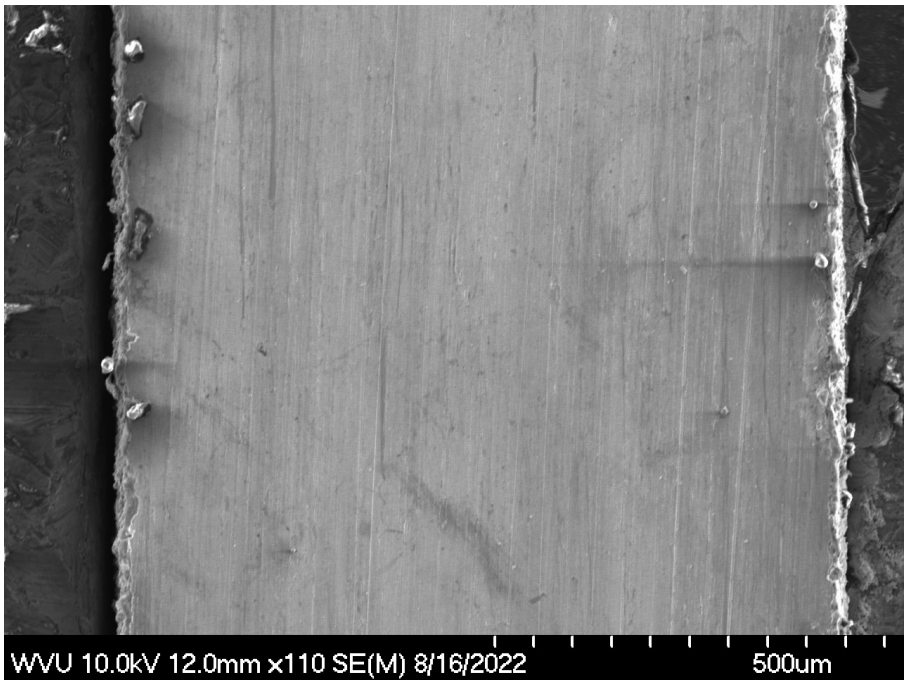

Figure 3.2: Pre corrosion SEM image of 1 mm thick stainless steel sample.

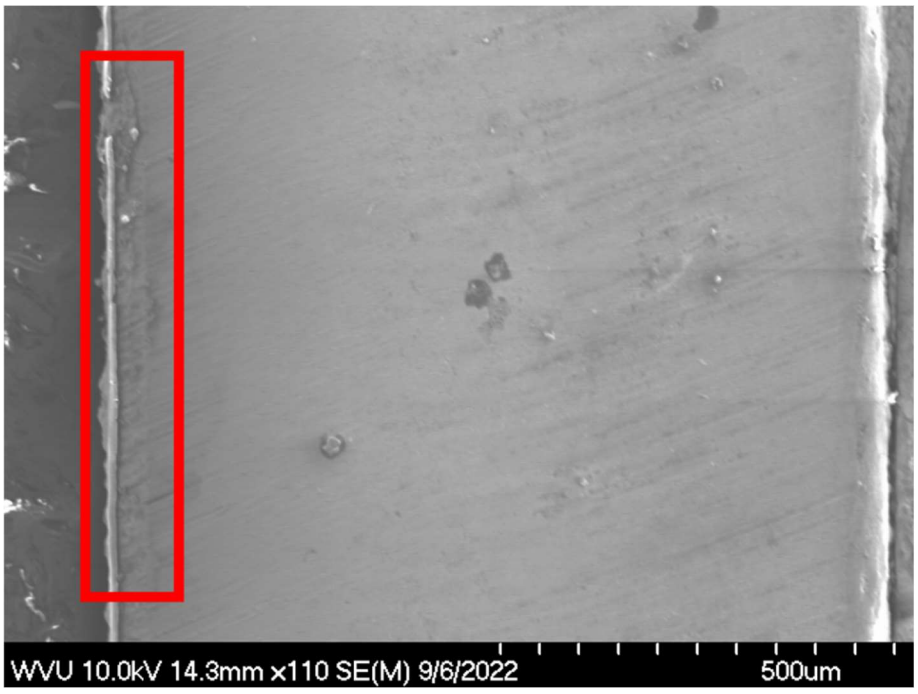

Figure 3.3: Post corrosion SEM image of 1 mm thick stainless steel sample with oxide growth identified in red.

Sensor miniaturization was concurrently investigated to enhance compatibility with in-situ pipe applications. Figures 3.4 and 3.5 illustrate the transition from large three-turn and five-turn inductors to smaller square and coiled designs. This downsizing led to a shift in resonant frequency from the low MHz range (40–200 MHz) to the low GHz range (1.4–3.4 GHz), directly attributed to the reduction in inductance and capacitance.

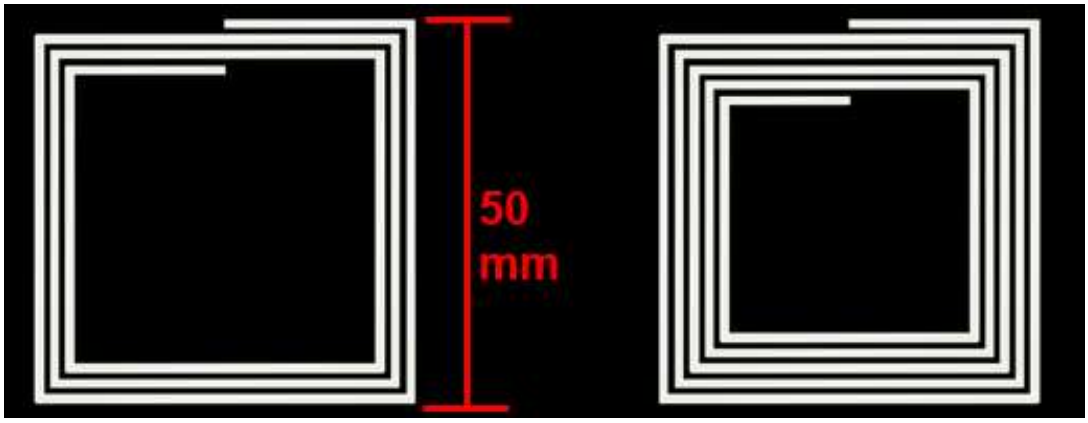

Figure 3.4: Geometry of large three turn and five turn inductors respectively.

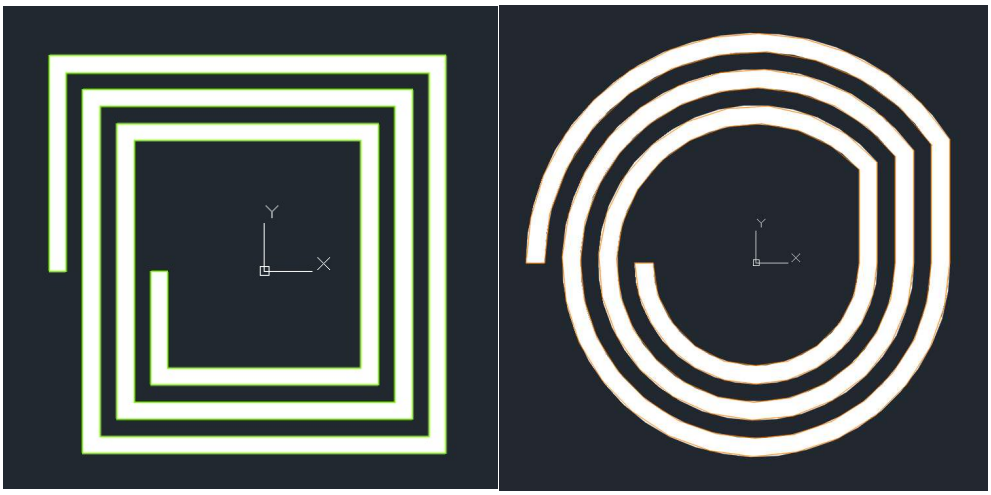

Figure 3.5: Geometry of small square inductor and small coiled inductor respectively.

Silver-based inkjet inks used in the fabrication exhibited good printability and electrical performance. However, certain challenges arose in achieving uniform thickness over larger areas, particularly with complex inductor geometries. These limitations were mitigated through the use of thin-film deposition techniques in conjunction with smaller sensor layouts. These findings validate both the oxidation kinetics model and the material performance criteria established under Subtask 3.1. The experimental observations provide essential inputs for sensor design refinement and material system selection in the subsequent fabrication phase outlined in Subtask 3.2.

3.3.2 Fabrication of RFID and Patch Antenna Sensors Directly onto Planar Metal/Ceramic Substrates.

Figure 3.6 shows the optical images of the 5-turn glass-ceramic sensor. The findings indicate that the sensor, when interrogated both wirelessly and via wired connections up to 600 °C, did not register any detectable resonant frequency. This lack of response suggests potential limitations in the sensor's operational capability within this temperature range. Furthermore, an investigation into the Curie temperature was conducted above 900 °C, raising concerns about the influence of magnetism at elevated temperatures. The emergence of magnetism could negatively affect the sensor's performance, potentially obstructing accurate measurements or altering the underlying mechanisms of detection. These observations underscore the necessity for further research to explore the compatibility of the sensor materials and designs with high-temperature applications, as well as to assess the effects of magnetic properties on sensor functionality in relevant environments.

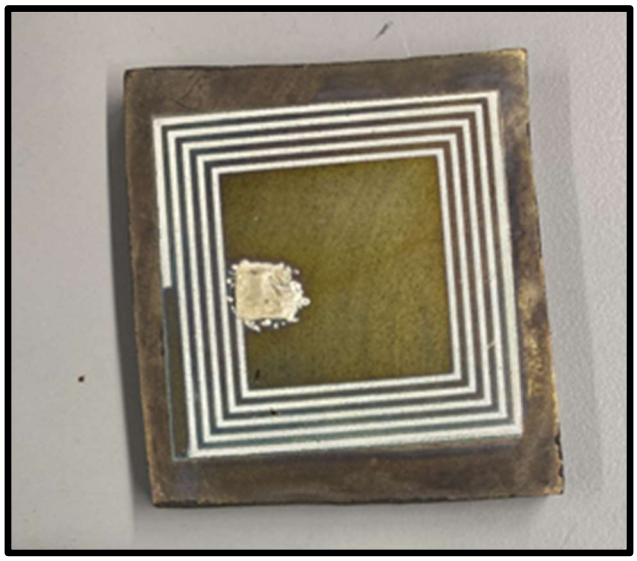

Figure 3.6: Optical images of 5 turn glass ceramic sensor

The following designs implement five-turn square inductors, with S11 responses of pproximately 95 MHz and 139 MHz, respectively. The square inductor is created with a 0.2 mm thick trace of silver printed on top of a 51x51x0.3 mm alumina substrate. Below the alumina is a 51x51x0.5 mm layer of silver acting as a ground plane.

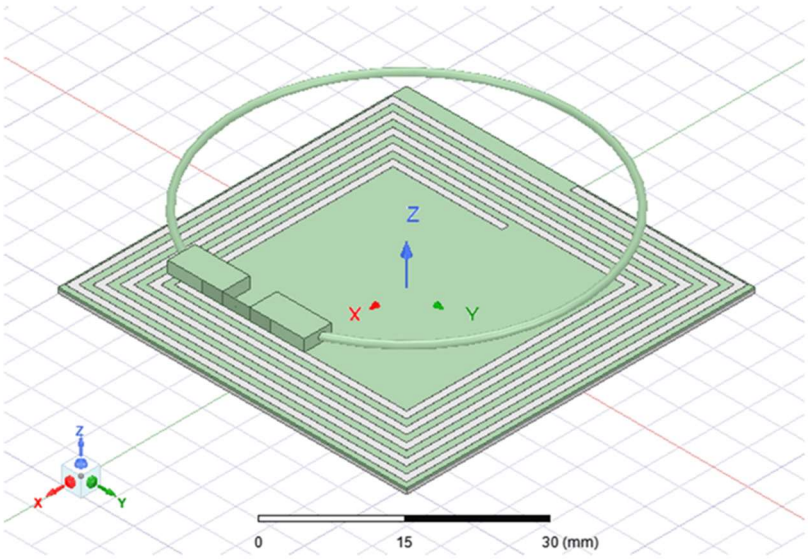

Figure 3.7: Schematic picture of the boundary conditions for the various EM inputs for the ANSYS simulation model of 5-turn silver inductor printed on alumina with a silver ground plane.

Three layers of Ag ink were printed in total with a 3 min time interval between layers to dry the previous layer. The fully printed sensor was then sintered in a box furnace (Sentry Xpress 4.0, Paragon Industries L.P., Mesquite, TX, USA) in ambient air. The sintering protocol was as follows: fired to 825 °C for 4 h with 2 °C/min for both the heating rate and the cooling rate. The final sintered Ag sensor can be seen in Figure 3.8.

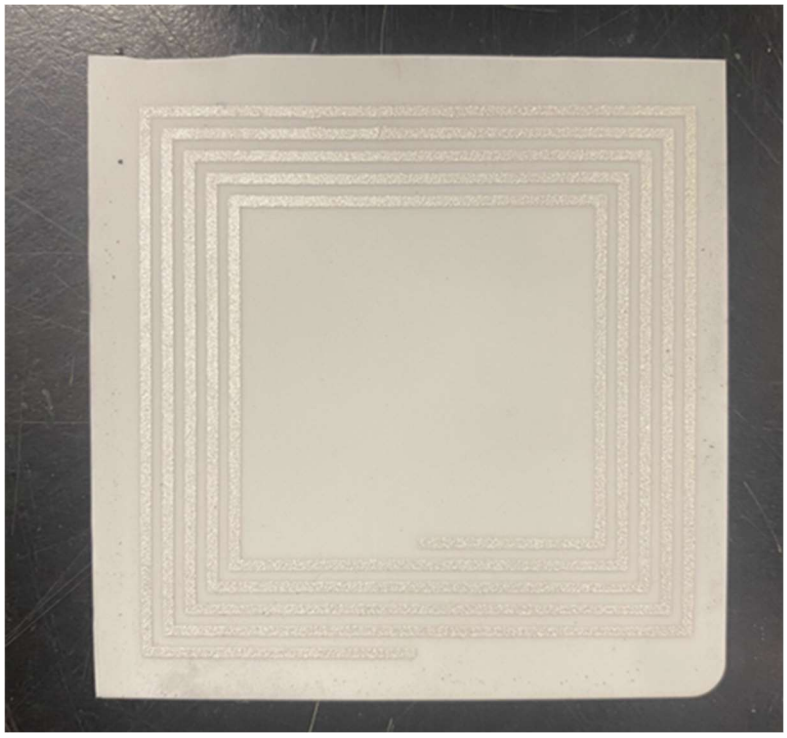

Figure 3.8: Optical image of 5-turn sensor after bonding the Ag inductor pattern onto the Al_2O_3 substrate.

The layers of Pt ink were printed with the same procedure as Ag. The sintering protocol was as follows: fired to 1400 °C for 2 h with 2 °C/min for both the heating rate and the cooling rate. The final sintered Pt sensor can be seen in Figure 3.9.

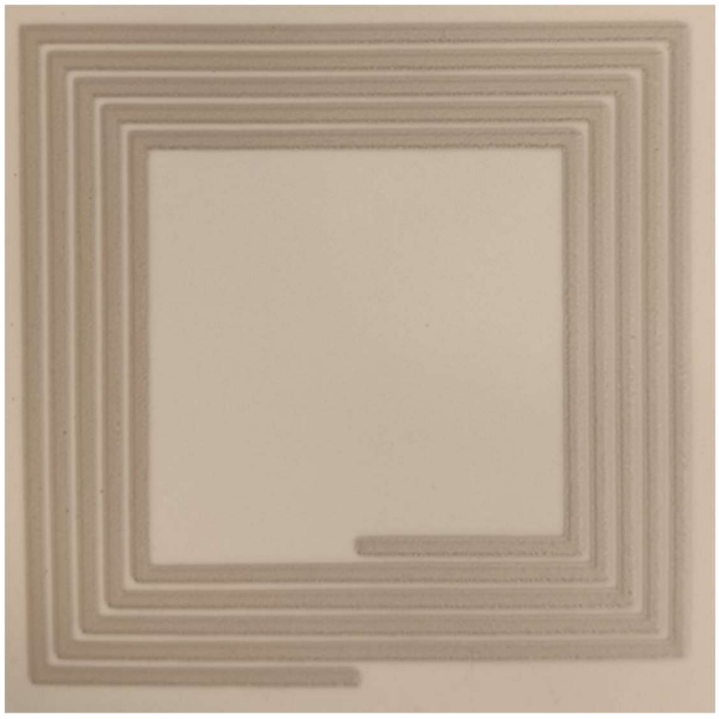

Figure 3.9: Optical image of 5-turn sensor after bonding the Pt inductor pattern onto the Al_2O_3 substrate.

3.3.3 Development of Inexpensive Transfer Process and Baseline Testing.

The process utilized a specially developed ceramic transfer paper and method. Initially, conductive ink (Ag ink) was applied to the glossy side of the decal paper via screen printing and then subjected to thermal treatment on a hot plate at a low temperature of 90 °C for 5 minutes to ensure adequate drying. Following this, an acrylic spray (Model #: K01303007, Krylon, Cleveland, OH, USA) was applied as a protective layer over the Ag ink to prevent any distortions during the transfer process. The application of the acrylic spray lasted for 15-20 seconds, with an emphasis on overlapping each pass adequately. This acrylic coating was applied twice, allowing for sufficient drying time between applications. Figure 3.10 (a) illustrates this procedure. Next, the decal paper was immersed in water to activate the release agent, facilitating its careful placement onto the Al_2O_3 substrate while maintaining the design integrity. To achieve the best results, a vacuum was utilized after application to ensure the sensor adhered flatly, or alternatively, a gradual sintering process (750 °C for 2 hours, with a heating and cooling rate of 2 °C/min) was employed to reduce acrylic burn-off. Figure 3.10 (b) depicts the sintering process of the Ag ink printed on the Al_2O_3 layer. This work shows that the same pattern shown for the previous work can be transferred to a planar substrate. Same procedure was applied to the Al_2O_3 curvature surface as illustrated in Figure 3.14.

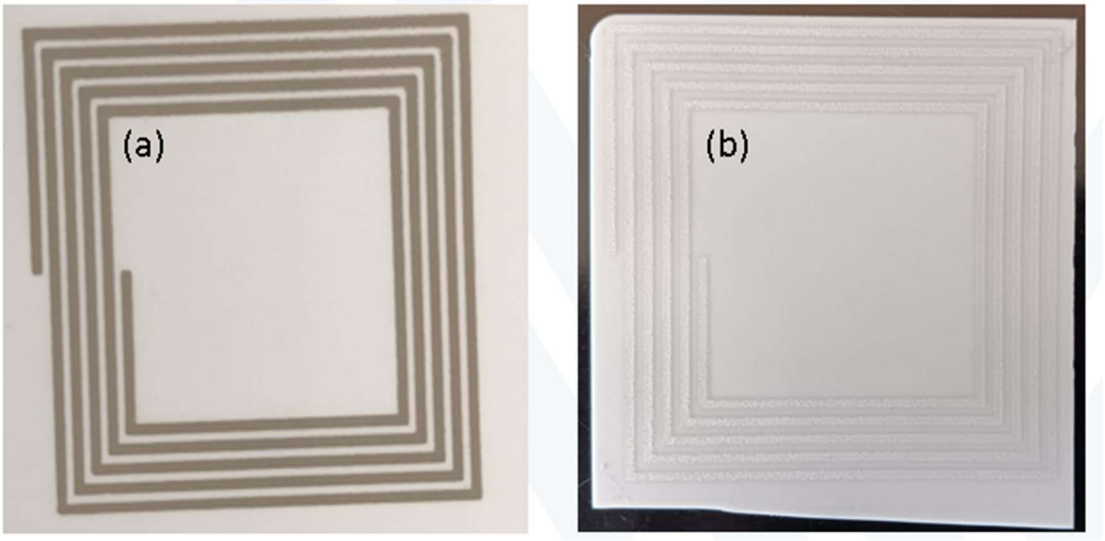

Figure 3.10: Peel and stick process (a) Ag screen printing and acrylic spray coating, (b) Sintered Ag on flat Al_2O_3 substrate.

3.3.4 **Direct Transfer of Sensor to Metal Tubing and Thermal Processing Development.**

Figure 3.11 presents the result after sintering, demonstrating successful transfer and uniform adhesion of the pattern onto the curved surface.

Figure 3.11: Peel and stick process sintered Ag on curvature Al_2O_3 substrate.

The sensor transfer procedure, employing a specially formulated ceramic decal method, was successfully extended to curved Al_2O_3 substrates, while maintaining consistency with the process previously applied to planar surfaces in earlier subtasks. Conductive silver (Ag) ink was screen-printed onto the glossy side of the decal paper and dried at 90 °C for 5 minutes to ensure proper solvent evaporation and ink stabilization. A protective acrylic overlay (Krylon, Model #: K01303007, Cleveland, OH, USA) was then applied in two successive passes, each lasting 15–20 seconds, with sufficient drying intervals between coatings to ensure layer integrity and protect the printed features during transfer.

The decal paper was immersed in deionized water to activate the release agent, enabling careful positioning of the sensor pattern onto the curved Al_2O_3 surface. Due to the surface geometry, vacuum assistance was employed to ensure complete adhesion and eliminate air gaps. A slow sintering process (2 °C/min up to 750 °C with a 2-hour hold, followed by controlled cooling) was carried out to remove the organic acrylic overlay and promote robust bonding between the Ag ink and the ceramic substrate.

Despite the challenges introduced by the curvature—such as uneven contact or distortion risk—the process yielded conformal, continuous, and defect-free sensor traces. This confirms that the same fabrication approach can be effectively adapted to non-planar geometries. The outcome

highlights the flexibility and reliability of the transfer method for integrating sensor patterns onto components with complex shapes.

Figure 3.12 shows the passive wireless sensor heating, cooling, and maximum temperature holding results for the ground plane without additional surface defects, tested with the peel-and-stick method. During the heating stage in Figure 3.15 (a), the sensor's peak decreased in magnitude by approximately 0.8 dB and shifted in frequency from 103.48 MHz to 103.32 MHz. This was the expected result because as the sensor was heated, the dielectric constant of the alumina increased, causing a corresponding downward frequency shift and magnitude decrease. During the max temperature hold stage in Figure 3.12 (b), the sensor's peak did not change in magnitude and shifted downward in frequency from 103.295 MHz to 103.290 MHz. The cooling stage of the ground plane with no defects is shown in Figure 3.12 (c), which displays the inverse of the heating stage. It increased in magnitude by approximately 0.7 dB and had an upward frequency shift from 130.33 MHz to 103.37 MHz. This is also the expected result, as the alumina's dielectric constant increases during heating and decreases during cooling.

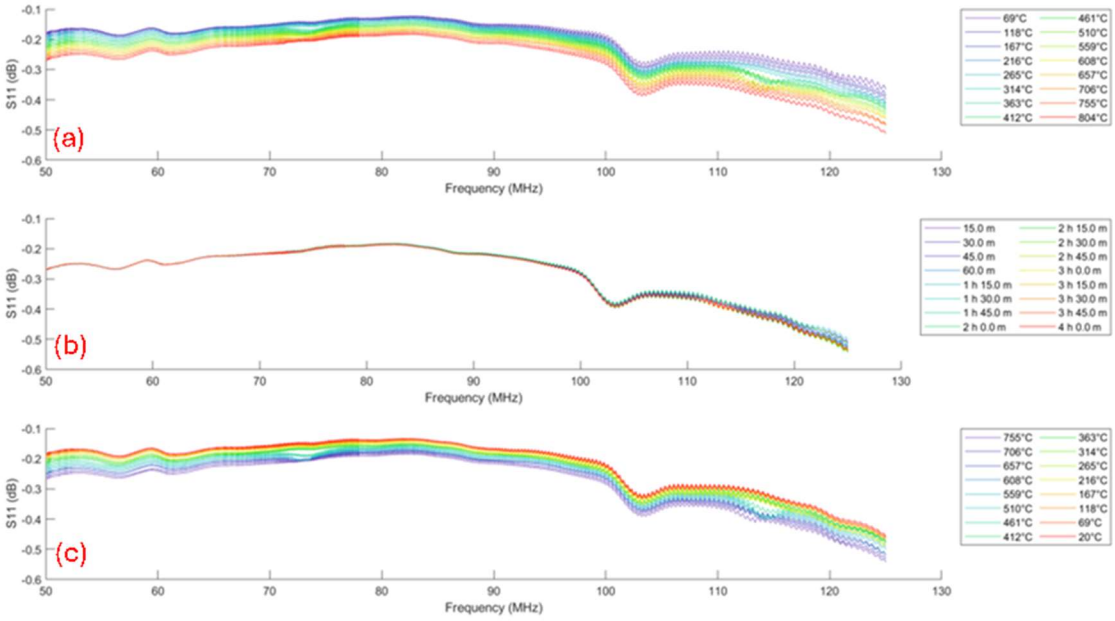

Figure 3.12: Passive wireless sensor heating and cooling furnace results on the Coppers ground plane (Peel and Stick method). (a) The sensor heating stage from room temperature to 800 °C at a rate of 120 °C/h. (b) The sensor maximum temperature hold at 800 °C for 4h. (c) The sensor cooling stage from 800 °C to room temperature at a rate of-120 °C/h

3.4 Conclusions:

This study presents a comprehensive investigation into high-temperature oxidation behavior, sensor miniaturization, and fabrication techniques relevant to wireless passive sensing systems. Stainless steel samples exposed to 600 °C exhibited a consistent and linear oxidation rate of approximately 30 μm/day, as confirmed through SEM analysis and quantitative image processing. The resulting oxide layer thickness provided critical insights into the time-dependent progression of corrosion. Simultaneously, efforts to reduce sensor size led to the development of smaller inductor geometries, which shifted resonant frequencies from the MHz to the GHz range, enabling improved integration within confined environments such as pipe interiors.

Fabrication trials on both planar and curved alumina surfaces using a peel-and-stick ceramic decal method demonstrated effective pattern transfer and adhesion. Successful sintering of Ag and Pt-based inductors at 825 °C and 1400 °C, respectively, validated the thermal robustness of the design. However, the five-turn glass-ceramic sensor did not yield detectable signals up to 600 °C, suggesting limitations in electromagnetic response at such temperatures. Additionally, baseline wireless measurements on curved substrates confirmed predictable shifts in magnitude and frequency with temperature variation, attributed to dielectric changes in the alumina. Overall, the results highlight the viability of the transfer process, the importance of miniaturized sensor design, and the need for continued refinement of sensor materials to enhance functionality under extreme conditions.

Task 4: Cyclic Passive Wireless Sensor Testing

4.1 Introduction:

This study focuses on the evaluation of singular passive wireless sensors applied to flat sheets of metal grades. Sensor designs developed in Task 2 will be tested using conductive materials identified in Task 3. Isothermal and cyclic crack tests will be conducted between 500 and 1300 °C, under varying humidity levels, to assess temperature fluctuations and the rate of cracking and decomposition. A standard sample will also be included to establish a baseline for comparing the corrosion rates of the sensor-equipped specimens. Microstructural analysis using Scanning Electron Microscopy (SEM) and Energy Dispersive Spectroscopy (EDS) will be employed to measure crack and corrosion lengths, thereby providing insights into oxidation kinetics. The data obtained will be correlated with the sensor outputs to identify health and temperature-related trends.

Subtask 4.1: Temperature and Corrosion Induced Crack Testing of Singular Passive Wireless Sensors

Singular passive wireless sensors will be deposited onto flat sheets of high-temperature metal (such as SS340H). Different designs from Task 2 will be evaluated initially using conductive materials identified in Task 3. Isothermal and cyclic crack tests will be completed at temperatures of 500-1300°C with various humidity levels. Both the temperature variation and the cracking/decomposition rate will be evaluated. A standard sample will be characterized for their corrosion kinetics to compare against that measured with the sensor during the corrosion test. Microstructural and compositional analysis (SEM, EDS, XPS, Raman etc.) will be used to measure cracking and corrosion, and this information will be used to define oxidation (failure) kinetics. This information will be related back to the sensor output in order to define health and temperature related trends. Advanced signal processing methods defined in Task 2 will be used to deconvolute the sensor data and relate the key sensor parameters to the selectivity and sensitivity of the sensor, and this will assist in defining the sensor arrays in the following subtasks.

Subtask 4.2: Performance Evaluation of Wireless Sensor Arrays at Low Temperature.

The sensor arrays (two or more sensors) will be initially tested up to 500ºC to identify the issues with high-temperature experiment. Representative sample arrays (with RFID sensors) will be inserted at various distances and orientations to replicate an initial evaluation completed in Task 2. The interrogator antenna design and placement (as function of distance from the RFID sensors) will be the key aspect of this work. Temperature, corrosion, and corrosion-induced crack effects will be characterized. Key sensor parameters will be identified to carry into high-temperature testing evaluations in Subtask 4.3.

Subtask 4.3: ***Performance Evaluation of Wireless Sensor Arrays at High Temperature*****.**

The high-temperature test stand will be used for testing the passive wireless sensor arrays to 500-1300°C. Sensor designs and configurations (i.e. placement distances and orientations) will be

investigated and related to modelling in Task 2 and Subtask 4.2. Isothermal and cyclic crack propagation tests will be completed (depending upon temperature), and microstructures from each sensor location will be evaluated using SEM, diffraction (XRD) and spectroscopic (XPS, Raman, etc.) techniques (and related to signal data obtained). The optimized sensors, and data processing and passive wireless circuits from Task 4 will be carried into further sensor wireless sensor testing in Task 5 and the final demonstrations in Task 6.

4.2 Experimental Methods:

4.2.1. Temperature and Corrosion-Induced Crack Testing of Singular Passive Wireless Sensors

To investigate the influence of high-temperature oxidation and corrosion-induced crack formation on passive LC wireless sensors, a series of single-sensor experiments were conducted using Cu110 and SS304H metallic substrates. These trials aimed to characterize the sensitivity and reliability of the sensors under thermally aggressive and mechanically degrading environments, simulating long-term service conditions.

The sensors used in these experiments consisted of five-turn silver planar inductors screen-printed onto high-density alumina substrates (96% dense, 99% purity; MTI Corp., Richmond, USA). The silver paste formulation was bimodal in particle distribution with a fine-to-coarse ratio of 1:4. It was deposited through a 230-mesh screen and sintered in ambient air at 825 °C for 4 hours, following a heating ramp rate of 2 °C/min, to ensure optimal conductivity and mechanical integrity. All sensors used across different test scenarios were fabricated identically to maintain experimental consistency.

Metallic ground planes were machined from Cu110 (99.5% Cu, McMaster-Carr) and SS304H stainless steel into square coupons of 76.2 mm × 76.2 mm × 6.35 mm. All sample surfaces were prepared using sequential polishing with SiC abrasive papers of grit sizes 400, 600, 800, 1200, and 1500, producing uniform, reflective surfaces. For the Cu110 experiments, three different surface integrity levels were prepared to examine the impact of substrate degradation on sensor response. These included: (i) pristine surfaces, (ii) minimally damaged surfaces with two perpendicular cuts (0.5 mm wide × 0.5 mm deep) forming four quadrants, and (iii) severely damaged surfaces with four cuts forming nine equal segments. A 2D diagram illustrating the cuts made on the copper ground planes can be found in Figure 4.1.

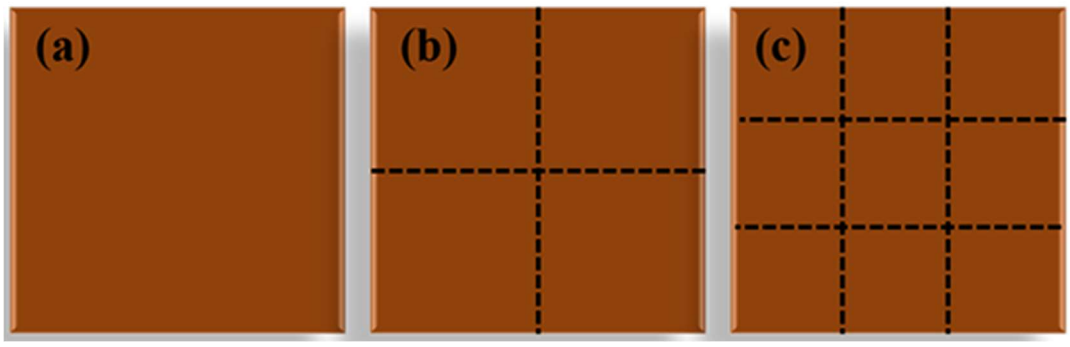

Figure 4.1: 2D illustration of the cuts made on the copper ground planes to evaluate the effects of structural integrity on the ground plane.

These predefined surface features were intended to simulate different extents of crack propagation and oxide spallation. Each sensor was positioned centrally on the polished metal substrate. A single-loop interrogator antenna, made from a 0.2 mm diameter platinum wire, was aligned 1.2 mm above the sensor. To ensure mechanical stability during thermal expansion and avoid antenna deformation, the setup incorporated two square alumina plates (0.5 mm thick, 26 cm^2 area), placed below and above the loop antenna. No mechanical fasteners or adhesives were used; all components were self-aligned through gravity-based stacking to preserve dielectric continuity and eliminate unwanted thermal stress.

Thermal testing was performed inside a high-temperature box furnace and consisted of three stages: (1) heating at a rate of 120 °C/h, (2) isothermal holding, and (3) cooling at −120 °C/h. For the Cu110 experiments, an isothermal hold of 800 °C for 4 hours was implemented. In contrast, SS304H substrates were subjected to an extended oxidation regime at 1000 °C for 120 hours in static air, simulating prolonged high-temperature exposure.

Throughout the entire heating cycle, the sensors were interrogated using a Keysight FieldFox N9918A vector network analyzer (26.5 GHz), interfaced with a custom MATLAB script. Reflection coefficients (S_{11}) were measured over the 50–125 MHz range. Data acquisition was conducted every 30 minutes during heating and cooling, and every 20 minutes (Cu110) or 6 hours (SS304H) during isothermal stages. Each measurement point was averaged over 100 sweeps to minimize noise and improve signal reliability.

Following the thermal tests, post-characterization of the oxidized surfaces was performed. Cu110 substrates exhibited oxide growth following parabolic kinetics, with an estimated oxide thickness of ~189 μm after 4 hours at 800 °C, as confirmed by thermogravimetric analysis (TGA) and cross-sectional SEM imaging. Cracks initiated along predefined surface notches were visible, correlating with signal magnitude losses and frequency shifts from ~81.3 MHz to ~77.7 MHz. These changes signified the onset of oxide layer delamination and structural discontinuity, directly captured by the sensor response.

SS304H samples, after 120 hours at 1000 °C, developed complex multi-layer oxide scales consisting of Fe_2O_3 as verified by SEM-EDS. Evidence of localized cracking and oxide spallation was observed, especially near grain boundaries. These physical changes corresponded with gradual reductions in signal amplitude and alterations in resonance frequency, demonstrating the sensor's capability to detect not only oxidation but also underlying crack development over prolonged thermal cycling.

Overall, this unified experiment demonstrated that a singular passive LC wireless sensor, when deployed on Cu110 and SS304H substrates, is capable of detecting both temperature variation and corrosion-induced mechanical degradation with high fidelity, making it a promising tool for real-time structural health monitoring in harsh environments.

4.2.2: Performance Evaluation of Wireless Sensor Arrays at Low Temperature

The final series of room-temperature experiments involved multi-sensor evaluations designed to examine signal interference and individual sensor response. Two passive LC wireless sensors were used: a temperature-only sensor and a temperature-corrosion sensor, both fabricated by screen-printing a five-turn silver inductor onto high-purity (99%), dense alumina ceramic substrates. The sensors shared identical geometries but differed in placement. The temperature-only sensor was suspended above the metallic ground plane using an alumina spacer, eliminating electromagnetic coupling with the substrate and ensuring a response only to ambient temperature. The temperature-corrosion sensor was placed directly on a conductive ground plane (copper) to capture both thermal variations and potential interactions with the underlying metal surface. Measurements were carried out with a single-loop platinum antenna (0.2 mm diameter) placed centrally between the two sensors. The antenna was aligned at a fixed vertical distance of 1.2 mm and connected to a vector network analyzer scanning the 50–125 MHz range. Sensor alignment was incrementally shifted in 0.5 cm steps up to ±1.5 cm to evaluate signal dominance and readability. The experiment was repeated with and without ground planes to assess their influence on signal magnitude and resolution.

4.2.3 Performance Evaluation of Wireless Sensor Arrays at High Temperature

This section presents the experimental methodology used to evaluate the high-temperature performance of the passive wireless sensors. All experiments were conducted at elevated temperatures; no low-temperature tests were performed, and testing began directly from room temperature. The primary objective was to observe sensor behavior during controlled heating, isothermal hold, and cooling stages, using two different ground plane materials—copper (Cu110) and stainless steel (SS304H). The sensor design consisted of a 5-turn silver planar inductor printed on an alumina substrate (96% dense, 99% pure; MTI Corp., Richmond, USA), which served as the dielectric layer. The bottom conductive layer was either copper or stainless steel, functioning as the ground plane. The sensor array incorporated two types of configurations: one sensor was placed in direct contact with the ground plane to function as a temperature-and-corrosion sensor, while another was elevated above the metal surface using alumina spacers to act as a temperature-only sensor. This arrangement allowed simultaneous observation of corrosion-related effects and pure temperature response. The sensors were interrogated wirelessly using a single-loop platinum antenna (0.2 mm diameter), which was positioned 1.2 mm above the temperature-and-corrosion sensor. This antenna was supported by a 0.5 mm thick square alumina plate (26 cm^2 area), placed 0.7 mm above the sensor. Another alumina plate was placed above the antenna to ensure mechanical stability during furnace operation. The temperature-only sensor was situated 5.0 mm above the top plate. All components were aligned using ceramic support structures without the need for mechanical fasteners or adhesives. This configuration ensured stable alignment and minimized thermal distortion throughout the experiment. A schematic diagram of the setup is provided in Figure 4.2, illustrating the vertical stacking arrangement of the sensor, antenna, and alumina plates. For the copper test, the Cu110 ground plane was polished using SiC abrasive papers ranging from 400 to 1500 grit to ensure uniform surface conditions and controlled oxidation

behavior. The sensor array was placed at the center of the furnace and subjected to a three-stage thermal cycle: heating from room temperature to 800 °C at a rate of 120 °C/hour with data recorded every 30 minutes; an isothermal hold at 800 °C for 4 hours with measurements every 20 minutes; and cooling back to room temperature at a rate of -120 °C/hour, again recording at 30-minute intervals. For the stainless steel test, a single sensor was placed directly onto the SS304H ground plane. The experimental procedure followed the same heating and cooling rates, but the isothermal hold was extended to 120 hours at 1000 °C to account for the slower oxidation kinetics of stainless steel. In this case, only one sensor–antenna pair was used, and no additional elevated sensor was included. This extended exposure was necessary to observe measurable corrosion effects under realistic high-temperature service conditions. Throughout all tests, wireless interrogation was performed using a spectrum analyzer and signal generator connected to the antenna, enabling real-time monitoring of the resonant frequency and magnitude shifts associated with temperature variation and corrosion layer growth. These experiments provided critical insight into the performance of passive wireless sensors under thermal stress and oxidative environments, supporting the analysis discussed in the subsequent result sections.

4.3 Results and Discussion:

4.3.1 Temperature and Corrosion Induced Crack Testing of Singular Passive Wireless Sensors.

4.3.1.1 Corrosion Kinetics of Cu 110 Grade

Earlier studies on the oxidation of copper have indicated that the oxidation rate adheres to a parabolic time law. However, slight variations in this relationship have been observed within the temperature range of 350-1050 °C [5, 10-13]. These variations led to the classification of three distinct regions: high temperature (900-1050 °C), intermediate temperature (600-900 °C), and low temperature (350-600 °C). One objective of the current study is to establish a direct connection between oxidation kinetics and sensor signals, a relationship not previously addressed in existing literature. Table 4.1 presents the oxidation kinetic constant, commonly referred to as k" (expressed in $g^2\ cm^{-4}\ s^{-1}$), which was measured for Cu 110 through isothermal TGA analyses at temperatures of 600, 700, and 800 °C. The k" values obtained at these temperatures were 2×10^{-8}, 5×10^{-8}, and $1 \times 10^{-7}\ g^2\ cm^{-4}\ s^{-1}$, respectively. The activation energy, derived from the slope of the corresponding graph (Figure 4.2), was determined to be 76.6 kJ/mol, yielding an R^2 fit parameter of 0.9947. Previous studies found the activation energy of copper in an air atmosphere between 600 and 800 °C to range from 27 to 123 kJ/mol [11, 13-17]. The activation energy reported in this study (76 kJ/mol) falls within this established range.

Table 4.1: Calculated oxidation parabolic constants (k") for Cu samples in $g^2\ cm^{-4}\ s^{-1}$.

Temperature	k" ($g^2\ cm^{-4}\ s^{-1}$)

600 °C	2×10^{-8}
700 °C	5×10^{-8}
800 °C	1×10^{-7}

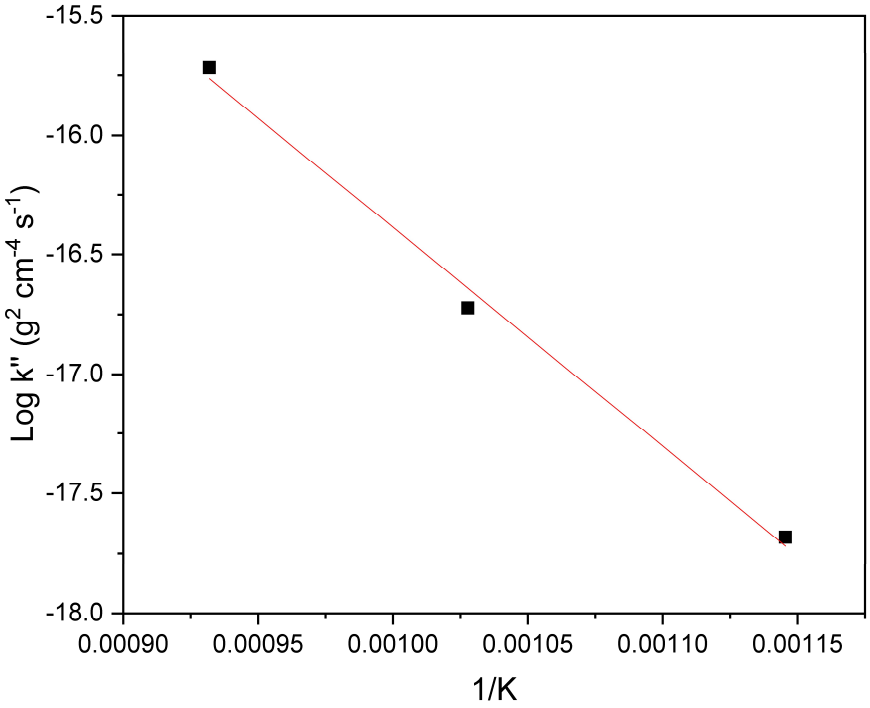

Figure 4.2: Arrhenius plot for the oxidation of copper in different temperatures

Figure 4.3 illustrates the estimated thickness of the oxide layer calculated from the TGA weight kinetics data, utilizing the sample surface dimensions. This information will later be compared with the sensor signals recorded during oxidation. Figure 4.3(a) shows the estimated oxide thickness growth upon heating to 800 °C, while Figure 4.3 (b) depicts the growth observed during the isothermal hold at that temperature.

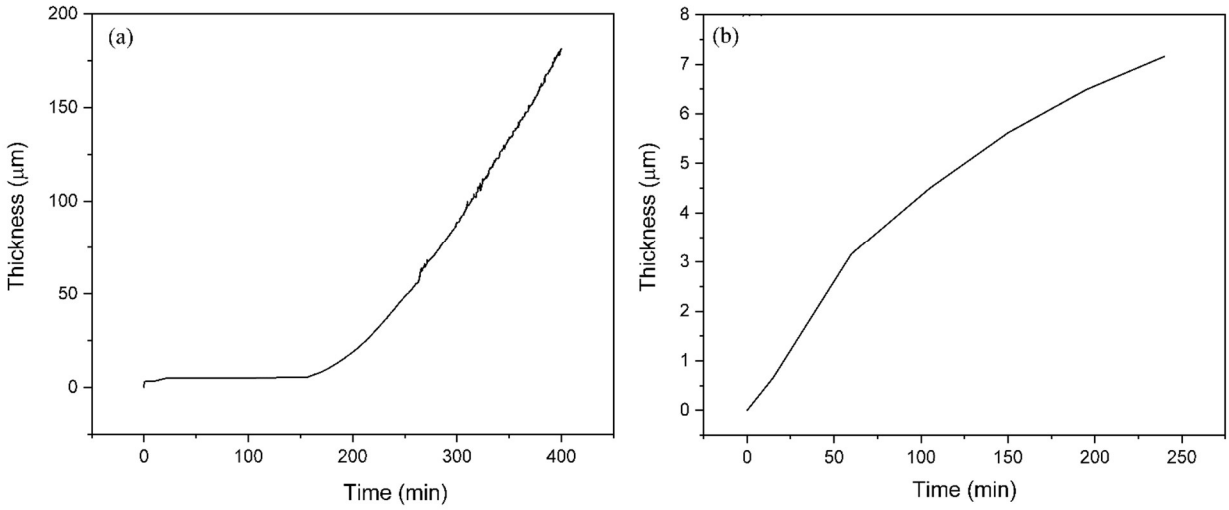

Figure 4.3: Copper oxide thickness growth obtained in TGA curves during (a) the heating stage from room temperature to 800 °C, and (b) the temperature isothermal hold at 800 °C for 4 h.

To validate the kinetic trends derived from the TGA data, pieces of Cu 110 were also oxidized in an air furnace under the same heating and isothermal conditions. Small sections of Cu 110, measuring (1 × 25.4 × 6.35 mm), were polished according to the previously described protocol to prepare them for SEM analysis. The samples were subsequently heated to 800 °C for four hours, employing a heating and cooling rate of 2 °C/min. Figure 4.4 displays the SEM image of the cross-section of one sample that was maintained at 800 °C for four hours. The SEM micrograph reveals that the oxide-copper interface remained intact and matched the roughness of the copper surface. Additionally, the micrograph exhibited a line of porosity along this interface. The oxide thickness was measured to be approximately 189 µm from the micrograph. The overall thickness change observed during heating and the isothermal hold (the total of Figures 4.3 (a) and (b)) was found to correlate well with the previously estimated oxide thickness kinetics. Thus, the oxidation kinetics determined for Cu 110 can be directly linked to the frequency signal shift recorded by the wireless sensor, which will be further elaborated upon in a subsequent section.

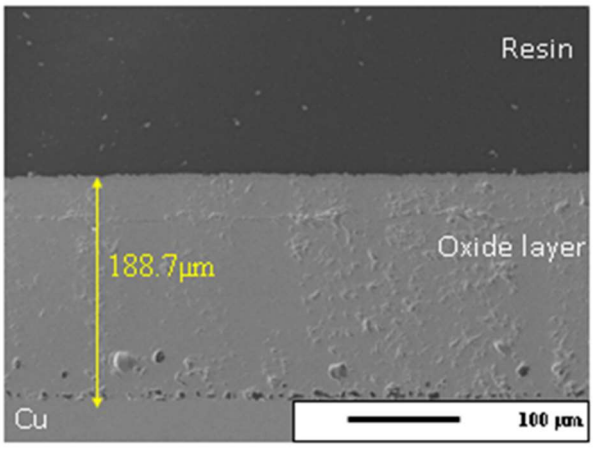

Figure 4.4: SEM cross-sectional image of oxide layers on copper oxidized under air atmosphere for 4 h at 800 °C.

3.3.1.2 Corrosion Kinetics of SS304H

In reality, oxidation is the process by which the oxide scale forms. If the generated oxide scale is thin, slowly developing, and sticky, the substrate is shielded from additional oxidation. The material eventually fails if the scale spalls often because the metal is constantly being devoured [18]. The literature contains several models for the oxide development on stainless steels [Thermodynamic and Kinetics Aspects of High Temperature Oxidation on a 304L Stainless Steel 19-23]. They can be summarized by considering how a chromium (Cr_2O_3) layer forms at low temperatures, serving as a barrier to prevent further oxidation. At higher temperatures, the chromium layer changes into the spinel-type oxide M_3O_4 (M = [Cr, Fe]). As it grows, its iron content increases steadily until it transforms into hematite (Fe_2O_3). The Wagner model can be used to explain how the oxide layer grows [24]. It describes the weight growth as a function of time by considering a parabolic law. Before starting the sensor testing on the SS304H ground planes in the current work, the oxidation kinetics for the SS304H employed in these studies were defined based on this and the minor differences observed in each investigation over the previous decades. This study aims to establish a direct link between sensor signal and oxidation kinetics, as we did in our previous [25] publication. The oxidation kinetic constant, commonly referred to as k" (in $g^2\ cm^{-4}\ s^{-1}$), was determined for the SS304H by isothermal TGA measurements at 900, 950, 1000 and 1050 °C and is displayed in Table 4.2. The k" values for 900, 950, 1000 and 1050 °C were measured as 7 x 10^{-10}, 5 x 10^{-10}, 2 x 10^{-10} and 1 x 10^{-10} $g^2\ cm^{-4}\ s^{-1}$, respectively. Based on the graph's slope (Figure 4.5)., the activation energy was calculated to be 173.3 kJ/mol, with an R^2 fit parameter of 0.96 . The literature shows that different steels have different activation energies at different temperatures and atmospheres. Between 850 and 950 °C, the activation energy of AISI304 steel was 158 kJ/mol, and that of AISI439 steel was 231 kJ/mol [26]. Lussana et al. [27]. reported that 304L Stainless Steel steel between 850 °C and 1200 °C had activation energies of 138 ± 12 kJ/mol The activation energy value (173.3 kJ/mol) in this investigation falls within the previously discovered range.

Table 4.2: Calculated oxidation parabolic constants (k") for SS304H samples in $g^2\ cm^{-4}\ s^{-1}$.

Temperature	k" ($g^2\ cm^{-4}\ s^{-1}$)
900 °C	7×10^{-10}
950 °C	5×10^{-10}
1000 °C	2×10^{-10}
1050 °C	1×10^{-10}

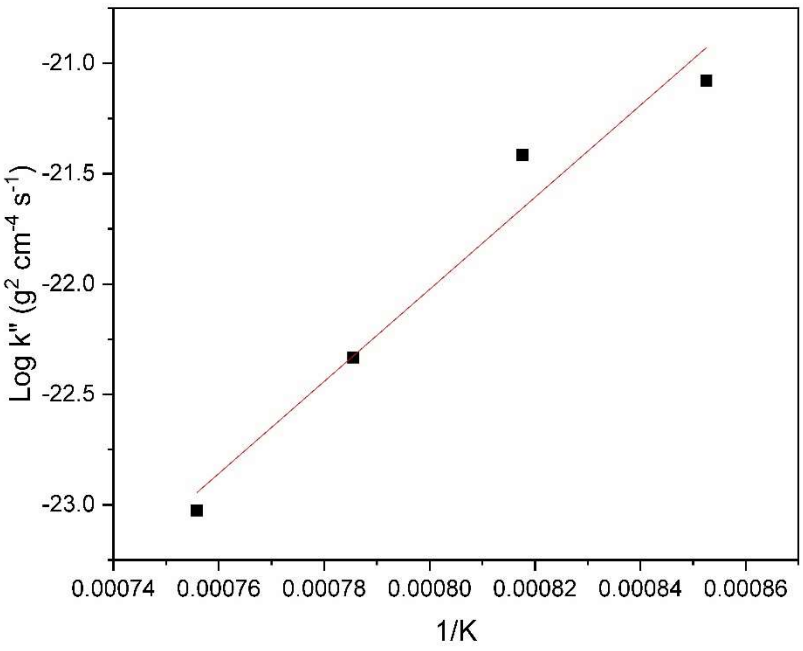

Figure 4.5: Arrhenius plot for the oxidation of SS304H in different temperatures

Figure 4.6 displays the SEM image of the cross-section of three samples held at 950°C, 1000°C and 1050°C for 4 h. From the SEM micrograph, it can be seen that the oxide-304H stainless steel interface was shown to be uncracked and conformed to the roughness of the steel surface. The SEM micrograph also showed a line of porosity following this interface. The oxide thickness increased with increasing temperature from 950°C (~ 13.5 µm) to 1050°C (~ 168 µm). In other words, when the temperature rises, the rate of oxidation increases.

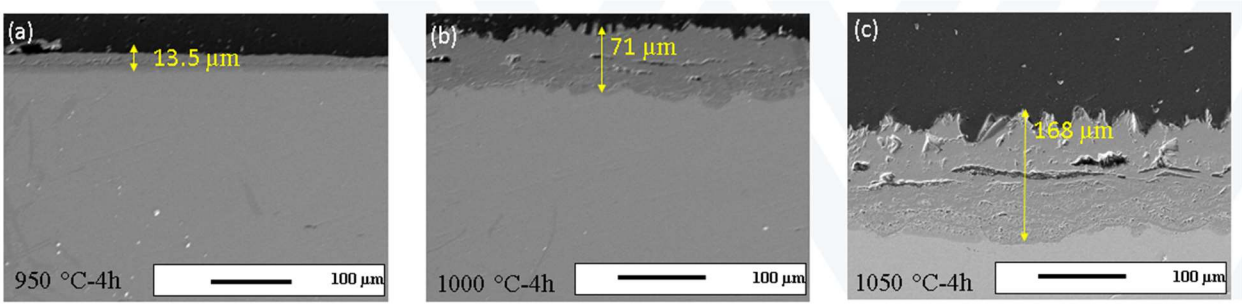

Figure 4.6: SEM cross-sectional image of oxide layers on SS304H oxidized under air atmosphere for 4 h between 950-1050 °C.

According to the information obtained from the literature, first, the oxidation rate of SS304H increases significantly when the temperature is raised from 950°C to 1050°C, which accelerates

diffusion processes. At 950°C, the oxidation rate is slower, and the oxide layer grows more steadily. However, at 1050°C, the diffusion of oxygen to the surface and alloying elements within the material becomes faster, leading to a thicker oxide layer and a higher growth rate. Second, at 950°C, SS304H typically forms a protective layer of Cr_2O_3 (chromium oxide) on its surface, which slows down oxidation and protects the metal. When the temperature is raised to 1050°C, the stability of the Cr_2O_3 layer decreases: At 1050°C, chromium oxide may start to evaporate or degrade, reducing the thickness and effectiveness of the protective layer and allowing oxidation to progress more rapidly. The third one is that the oxide layer can develop into multiple layers at both temperatures, but at 1050°C, the layer becomes thicker and more porous. At 950°C, a thinner and more homogeneous chromium oxide layer typically covers the surface [28].

Figure 4.7 shows the SEM image of the cross-section of three samples held at 1000°C for 4 h, 24 h, 48 h, and 72h. The SEM micrograph reveals that the oxide-304H stainless steel interface was uncracked and adapted to the steel's surface roughness. A line of porosity that followed this interface was also visible in the SEM image. The oxide thickness increased with increasing holding time from ~ 71 µm to ~ 297 µm.

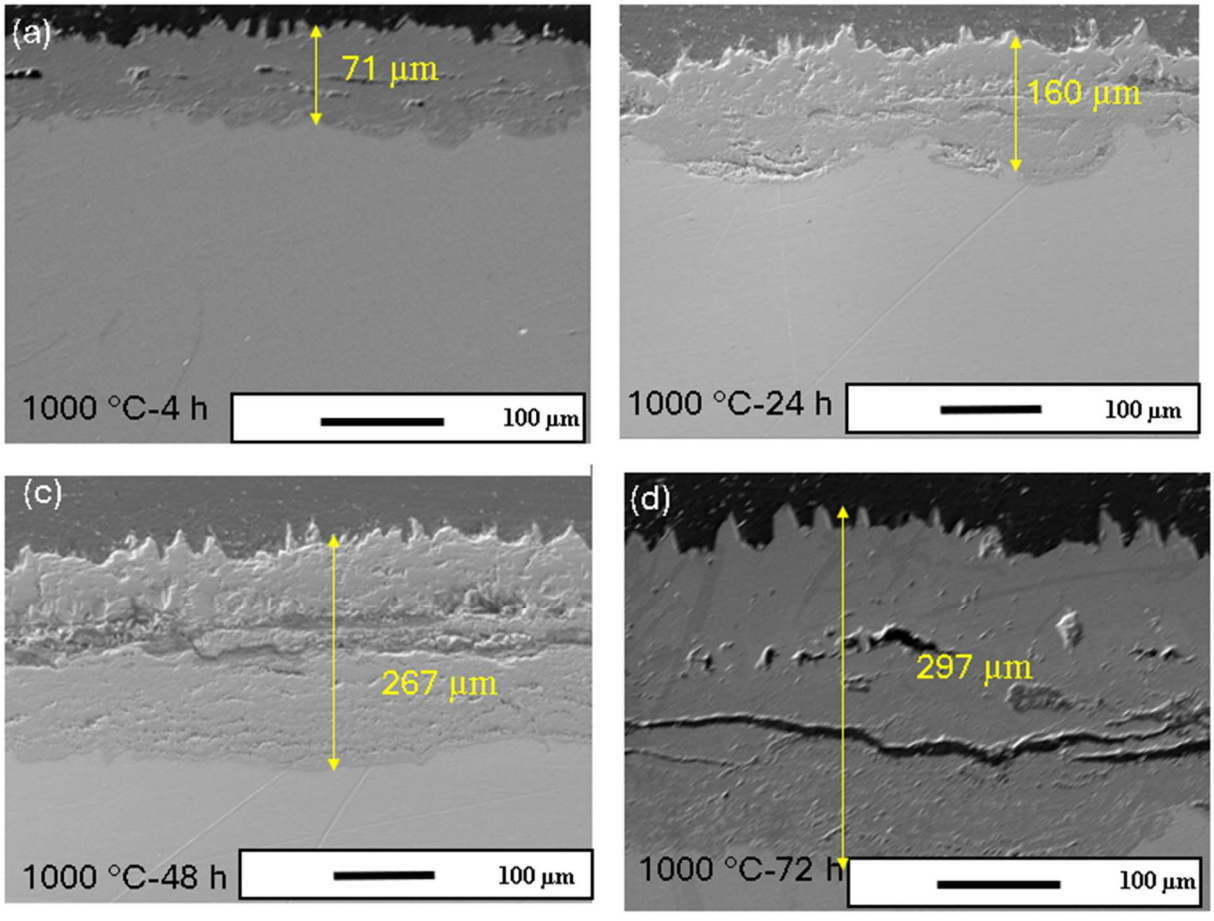

Figure 4.7: SEM cross-sectional image of oxide layers on SS304H oxidized under air atmosphere different coating times 4h, 24h, 48h, and 72h at 1000 °C.

It has been shown in the literature that at 1000 °C, the oxide layer on SS304H thickens over time. In the initial stage, a thin Cr_2O_3 (chromium oxide) layer forms rapidly, slowing oxidation. Over

time, the oxide layer thickens further, and Fe_3O_4 and Fe_2O_3 (iron oxides) accumulate on the surface, creating a multilayer structure. The thickness of the oxide layer continues to increase, though the growth rate slows down following a parabolic trend. During prolonged oxidation, the oxide layer becomes thicker and more porous, allowing oxygen to penetrate deeper into the steel [28].

Figure 4.8 (a) represent Pt structure, where a small porosity of Pt can be seen showing nonuniform coverage of Pt on the alumina substrate. The calculated average grain size of Pt structure were found to be 30.77 µm. Figure 3.8 (b) represents the cross-sectional boundary layer of Pt on the alumina substrate. The deposited layer can be shown to be uniform across the alumina substrate with a calculated thickness of 32.45 µm .

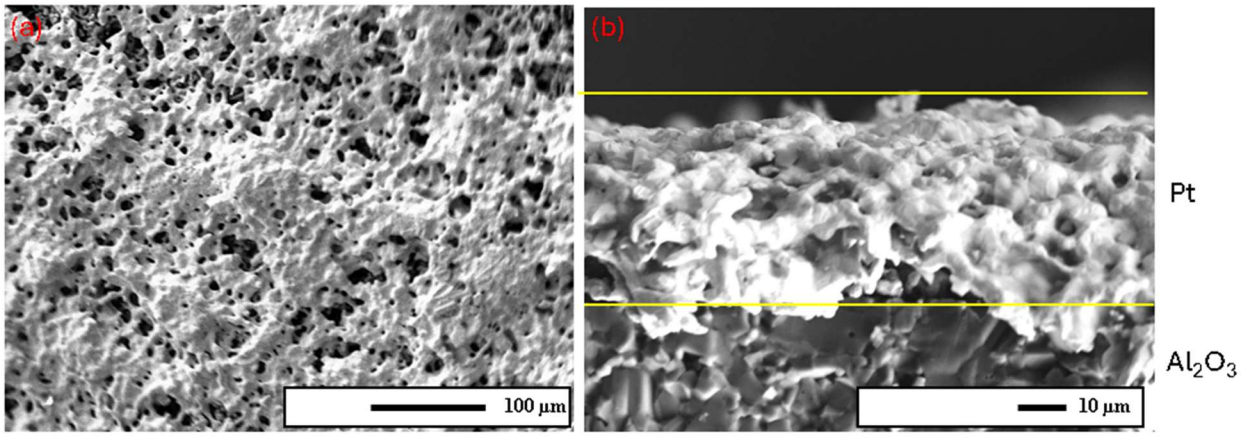

Figure 4.8: (a) SEM topographic image of Pt inductor, (b) Cross-sectional SEM image of Pt inductor bonded to alumina substrate.

Figure 4.9 illustrates the sensor response of a passive wireless system integrated onto a ground plane with no intentional surface defects, evaluated during heating, maximum temperature hold, and subsequent cooling phases. As shown in Figure 4.9 (a), during the heating phase, the sensor experienced a reduction in peak magnitude by approximately 0.5 dB and a downward frequency shift from 93 MHz to 82 MHz. This behavior is consistent with the simulation results in Figure 2.7 (a), as the increase in the dielectric constant of alumina with temperature leads to a corresponding frequency decrease and magnitude attenuation. Additionally, rising temperature reduces the conductivity of metallic conductors, further contributing to signal attenuation. In the maximum temperature hold phase (Figure 4.9 (b)), the sensor peak increased in magnitude by approximately 0.12 dB and continued to shift downward in frequency, from 82 MHz to 76 MHz This trend aligns with the simulation results in Figure 5b, where the progressive growth of oxide on the ground plane was shown to increase the signal magnitude while decreasing the resonant frequency in a generally linear manner. The cooling stage, shown in Figure 4.9 (c), revealed a reverse trend compared to heating. As the sensor cooled, its signal magnitude increased by around 0.5 dB, while the resonant frequency shifted upward from 76 MHz to 89 MHz This reversal is expected due to the reduction in the dielectric constant of alumina during cooling. Overall, the sensor's magnitude and frequency responses during both heating and cooling phases exhibited consistent and predictable trends, with minimal deviations or anomalies. The offset between the initial and final frequency values during thermal cycling serves as a clear indicator of oxidation,

allowing for straightforward tracking of corrosion-related changes. This frequency and magnitude shift can be quantitatively correlated with oxide thickness on the ground plane by comparing sensor behavior with corrosion kinetics obtained from previous thermogravimetric analysis (TGA) data. The simulation results provide a valuable modeling basis for interpreting the sensor response under high-temperature oxidation environments, specifically linking frequency shifts to oxide growth behavior on the Cu ground plane.

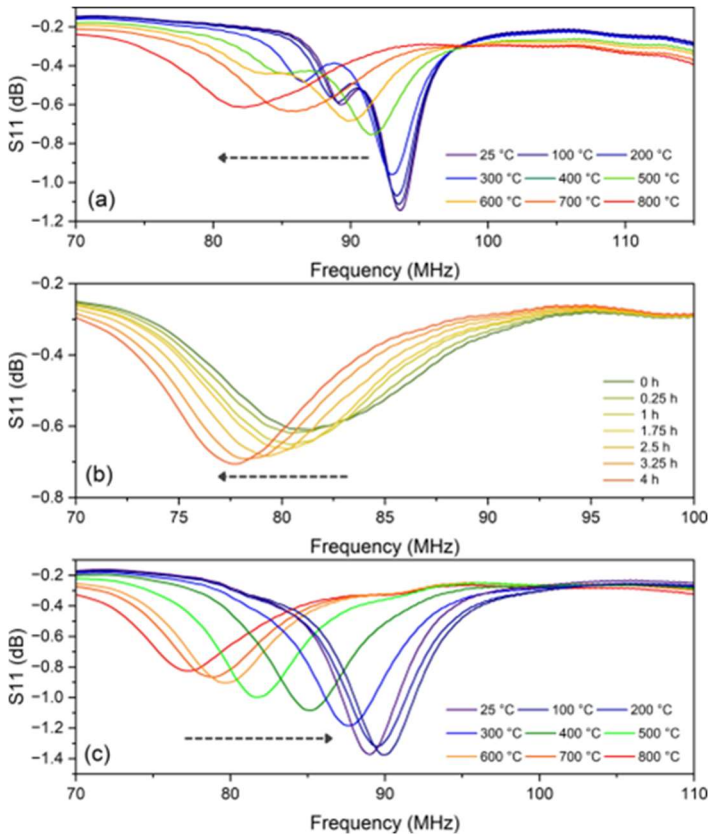

Figure 4.9: Passive wireless sensor heating and cooling results of the copper ground plane with no surface defects. (a) Sensor data for the heating stage from room temperature to 800 °C at a rate of 120 °C/h. (b) Sensor data at 800 °C isothermal hold for 4 h. (c) Sensor data for the cooling stage from 800 °C to room temperature at a rate of −120 °C/h

One significant finding from conducting multiple trials at 800 °C was the occurrence of substantial jumps in signal amplitude during the cooling phase, which deviated from the established trend lines. Upon removing the ground plane from the furnace, it was noted that the oxide layer had undergone considerable spallation and cracking. Based on these observations, it was hypothesized that the development of cracks or delamination within the oxide layer would lead to a shift in signal frequency and a reduction in amplitude.

To test this hypothesis, additional ground planes with enhanced surface defects were utilized to increase the likelihood of spallation and cracking. Figure 4.10 illustrates the maximum temperature

holding segments for each ground plane with varying defect quantities. Figure 4.10 (b) presents the sensor response during the isothermal hold for the ground plane exhibiting minimal surface defects (characterized by two initial saw cuts). This response mirrors the downward frequency shift seen in the defect-free sensor, but it results in a decrease in magnitude rather than an increase. This outcome contradicts the simulation results depicted in Figure 2.7 (b), as this sensor experienced a spallation event, indicating catastrophic failure of the oxide layer.

Figure 4.10 (c) illustrates the maximum temperature hold for the ground plane with maximum surface defects (marked by four initial saw cuts). The sensor response again shows the downward frequency shift observed in the other ground planes, but with minimal change in S11 magnitude. The behavior observed for each ground plane varied significantly depending on the extent of crack formation and propagation.

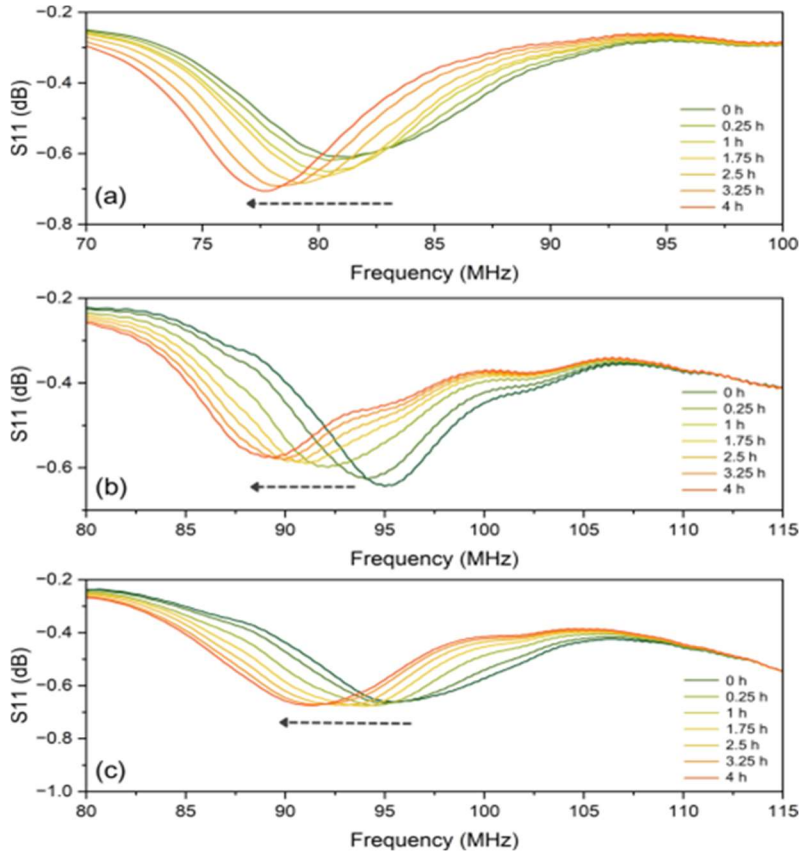

Figure 4.10: Passive wireless sensor responses for copper oxidation during the isothermal holding period at 800 °C for ground planes with varying levels of pre-existing surface defects. (a) Ground plane without defects, (b) ground plane with minimal defects, and (c) ground plane with maximum defects.

Figure 4.11 illustrates the key sensor frequency as a function of temperature during the heating and cooling phases for ground planes with various levels of pre-existing defects. In Figure 4.11 (a), the hysteresis of the defect-free ground plane is shown, indicating a consistent magnitude of frequency shifts during both heating and cooling. A frequency shift is observed during the maximum temperature hold at 800 °C, resulting in a gap between the heating and cooling curves.

This gap serves as an indicator of spallation, as the other two ground planes depicted in Figures 4.11 (b) and 4.11 (c) exhibit a greater frequency change during their cooling rates. In both of these plots, the cooling line intersects the heating line, which does not occur for the initially "defect-free" ground plane. This distinction is attributed to spallation events affecting the two ground planes with defects.

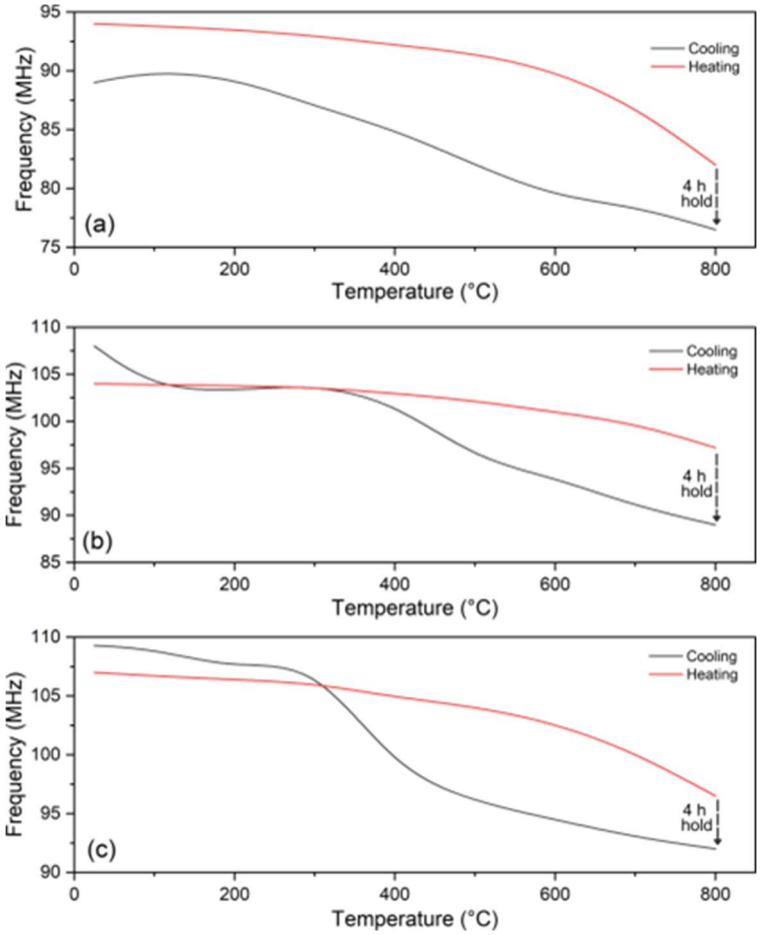

Figure 4.11: Passive wireless sensor frequency plotted against temperature during the heating and cooling stages of the experiment for ground planes with varying levels of pre-existing surface defects. (a) Ground plane without defects. (b) Ground plane with minimal defects. (c) Ground plane with maximum defects.

Low Frequency (50-70 MHz) Response of Triple-layer Sensors (for SS304H)

Figures 4.12 and 4.13 show the wireless response of triple-layer Pt inductor sensors at 1000 °C and 1050 °C, respectively. At 1000 °C, the resonance frequency shifted from ~59.55 MHz to ~59.30 MHz, accompanied by a signal magnitude change of ~0.14 dB. This response indicates improved spectral clarity and signal-to-noise ratio compared to thinner configurations, enabled by the increased conductance (~33 µm total thickness) of the Pt lines, which mitigates ohmic losses and enhances the resonator's quality factor.

Quantitative analysis during heating yielded frequency shifts of approximately 1.25–1.5 kHz/°C, while cooling resulted in slightly smaller shifts (~1.1–1.3 kHz/°C), suggesting mild hysteresis. The isothermal hold at 1000 °C produced a further frequency drop (~0.15 MHz) and magnitude

increase (~0.06 dB), consistent with oxide scale thickening. At 1050 °C, however, the response became less linear, with intermittent slope reversals, likely due to oxide instability or spallation effects.

While the triple-layer configuration exhibits superior stability and signal clarity under these conditions, its absolute performance still falls short of sensors utilizing silver (Ag) inductors, as demonstrated in previous work [29]. This is attributable to Pt's inherently lower conductivity (~9.3×10^6 S/m at room temperature) versus Ag (~6.3×10^7 S/m), reinforcing the need for alternative conductors in future designs targeting high-temperature applications.

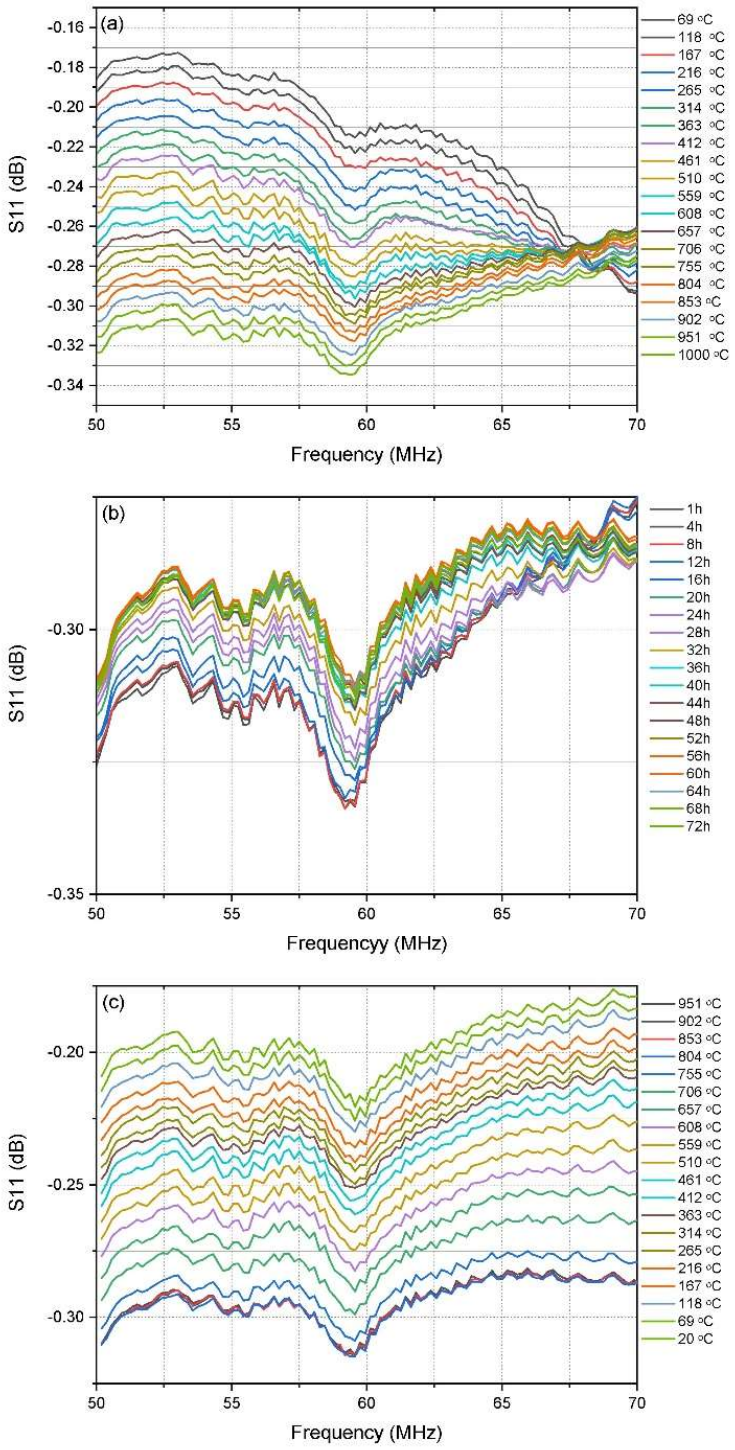

Figure 4.12: Passive wireless repeat sensor at low frequency (triple-layer platinum) heating, cooling, and maximum temperature hold furnace results. The top window (a) The multi-sensor response when heated from room temperature to 1000°C at a rate of 120°C/hour with data captured in 30-minute intervals. (b) The multi-sensor response when held at 1000°C for 72 hours with data

captured in 20-minute intervals. And (c) The multi-sensor response when cooled from 1000 °C to room temperature at a rate of -120 °C/hour with data captured in 30-minute intervals.

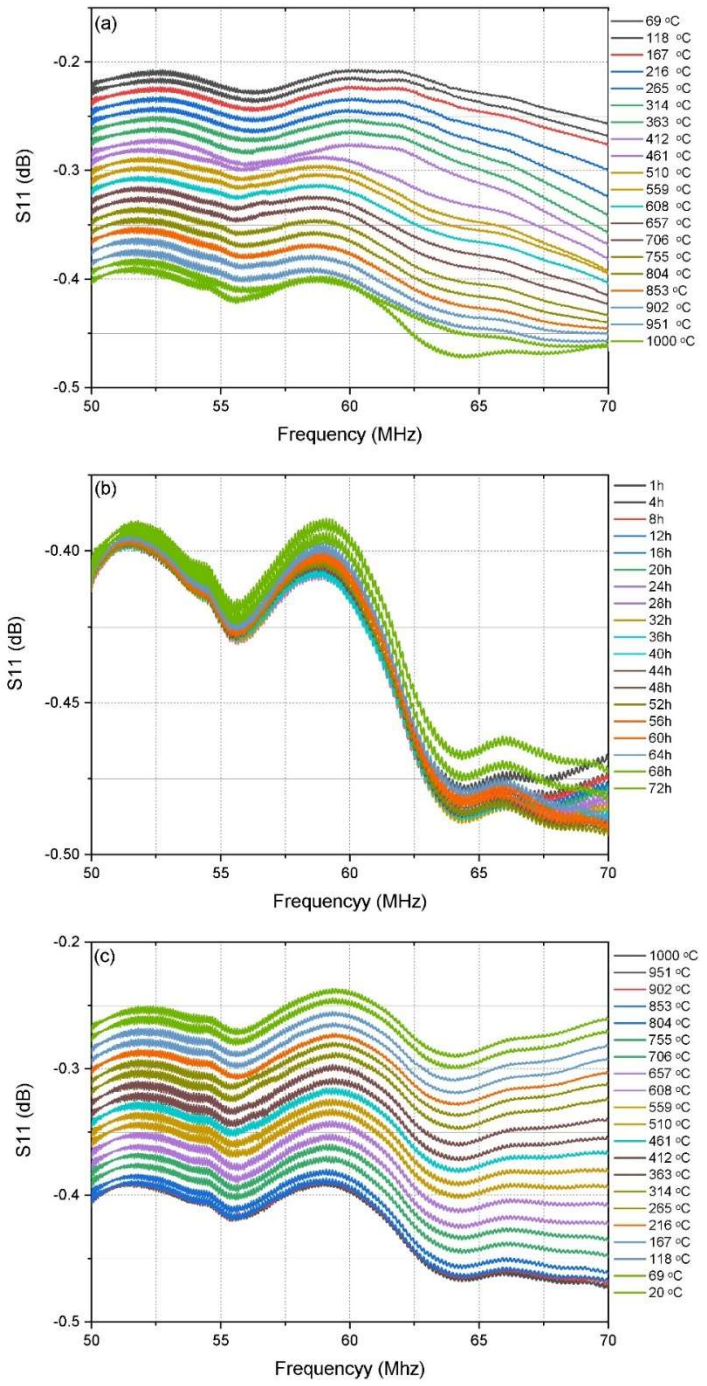

Figure 4.13: Passive wireless repeat sensor at low frequency (triple-layer platinum) heating, cooling, and maximum temperature hold furnace results. The top window (a) The multi-sensor response when heated from room temperature to 1050 °C at a rate of 120°C/hour with data captured in 30-minute intervals. (b) The multi-sensor response when held at 1000°C for 72 hours

with data captured in 20-minute intervals. And (c) The multi-sensor response when cooled from 1050 °C to room temperature at a rate of -120 °C/hour with data captured in 30-minute intervals.

Passive Wireless Temperature and Corrosion Sensing between 160-180 MHz (*for SS304H)*

Initial sensor measurements conducted at 50–70 MHz exhibited limitations in signal intensity and sensor sensitivity, particularly under high-temperature conditions. These issues were attributed to increased resistive losses in the platinum (Pt) inductor lines and suboptimal electromagnetic coupling, especially in single-layer Pt configurations. To overcome these limitations and enhance the fidelity of temperature-corrosion discrimination, attention was directed toward a higher frequency regime. Notably, a prominent resonance peak was experimentally observed within the 160–180 MHz range, which had not been predicted by the initial simulation models . The simulated models showed no discernible resonance in this harmonic range, likely due to the simplifications in modeling assumptions and exclusion of higher-order coupling effects. Hence, the resonance observed near 173 MHz is tentatively referred to as a "harmonic," acknowledging its empirical identification and unknown origin.

Among the various sensor configurations and operational parameters tested, the triple-layer Pt sensor operating in the 160–180 MHz range demonstrated superior signal clarity and frequency stability, particularly at elevated temperatures. This finding informed a targeted investigation in the 900–1050 °C range using isothermal and dynamic thermal profiles to determine optimal sensing conditions. The decision to focus on this window was guided by the objective of capturing a clear and repeatable frequency shift that correlates with oxidation behavior, without spallation disrupting sensor stability.

Figures 4.14 through 17 show the response of the triple-layer Pt sensor when subjected to heating (room temperature to target), isothermal holding (72 h), and cooling phases for maximum temperatures of 900 °C, 950 °C, 1000 °C, and 1050 °C. Each figure includes three subplots representing the respective thermal stages. During the heating phase at 900 °C (Figure 4.14), the sensor’s resonance frequency decreased from 171.75 MHz to 167.00 MHz, corresponding to a signal magnitude drop of approximately 0.5 dB. This was followed by a minor shift from 167.00 MHz to 166.50 MHz during the 72-hour isothermal hold, accompanied by a magnitude gain of about 0.2 dB. Upon cooling, the frequency increased to 169.50 MHz, and the signal magnitude rose by approximately 0.6 dB. At 950 °C (Figure 4.15), a frequency drop from 173.50 MHz to 169.50 MHz occurred during heating with a 0.7 dB magnitude loss, followed by a slight frequency reduction to 169.00 MHz and a 0.3 dB gain during the hold. The cooling phase restored the frequency to 172.00 MHz with a 0.4 dB signal gain. For the 1000 °C case (Figure 4.16), a clear frequency shift from 173.00 MHz to 169.50 MHz (corresponding to a 1.0 dB signal drop) was recorded during the heating stage, followed by a further shift to 168.25 MHz and a 0.5 dB magnitude increase during the hold. On cooling, the frequency recovered to 169.90 MHz, with a signal magnitude gain of approximately 1.0 dB. Lastly, at 1050 °C (Figure 4.17), the frequency declined from 174.00 MHz to 169.50 MHz during heating, with a 0.8 dB drop, then shifted slightly to 168.90 MHz during the hold, accompanied by a 0.5 dB gain. The cooling process resulted in a frequency increase to 168.90 MHz and a 1.5 dB signal gain. These detailed measurements illustrate the progressive impact of temperature on the sensor’s electromagnetic behavior, reflecting both thermal expansion and oxidation kinetics at the ground plane interface.

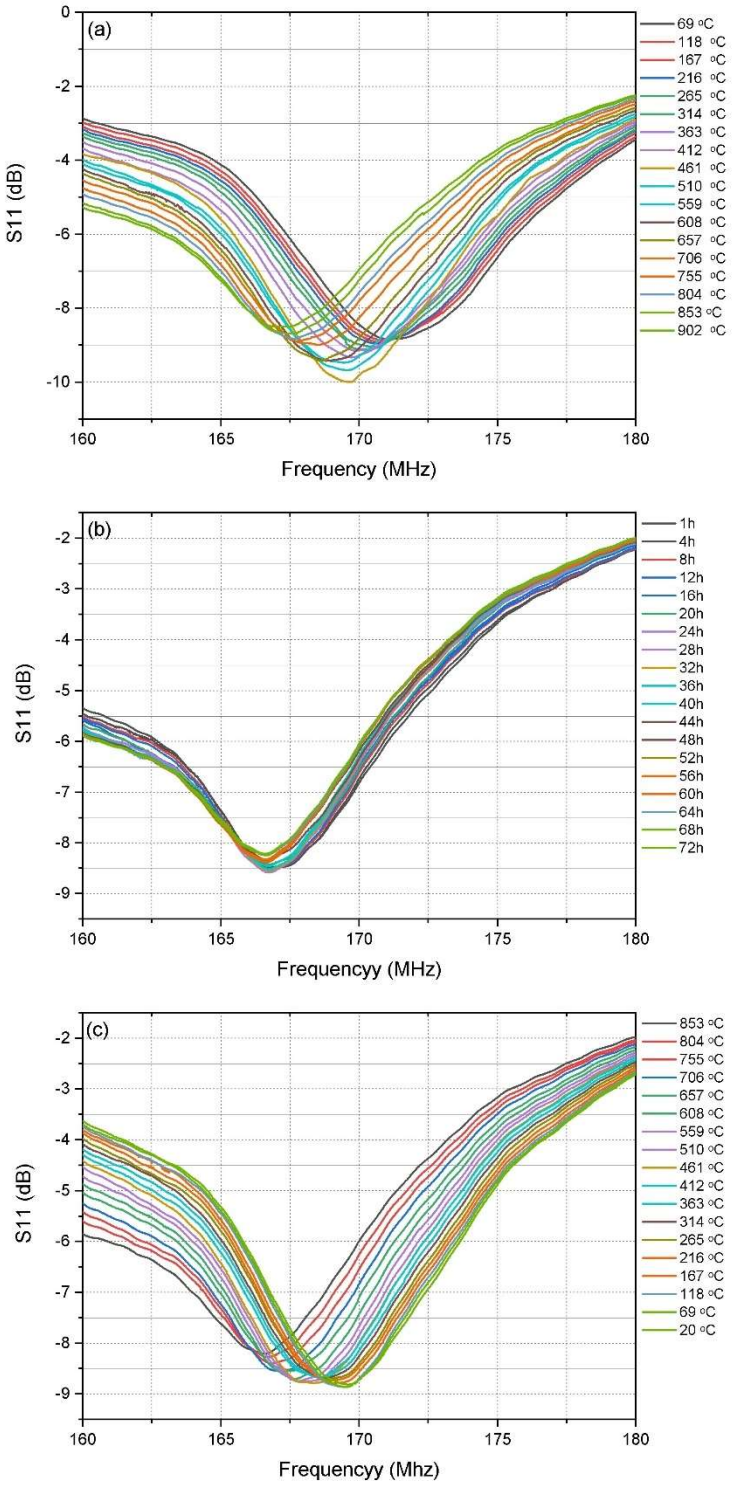

Figure 4.14: Passive wireless repeat sensor at high frequency (triple-layer platinum) heating, cooling, and maximum temperature hold furnace results. The top window (a) The multi-sensor response when heated from room temperature to 900°C at a rate of 120°C/hour with data captured in 30-minute intervals. (b) The multi-sensor response when held at 900°C for 72 hours with data

captured in 20-minute intervals. And (c) The multi-sensor response when cooled from 900 °C to room temperature at a rate of -120 °C/hour with data captured in 30-minute intervals.

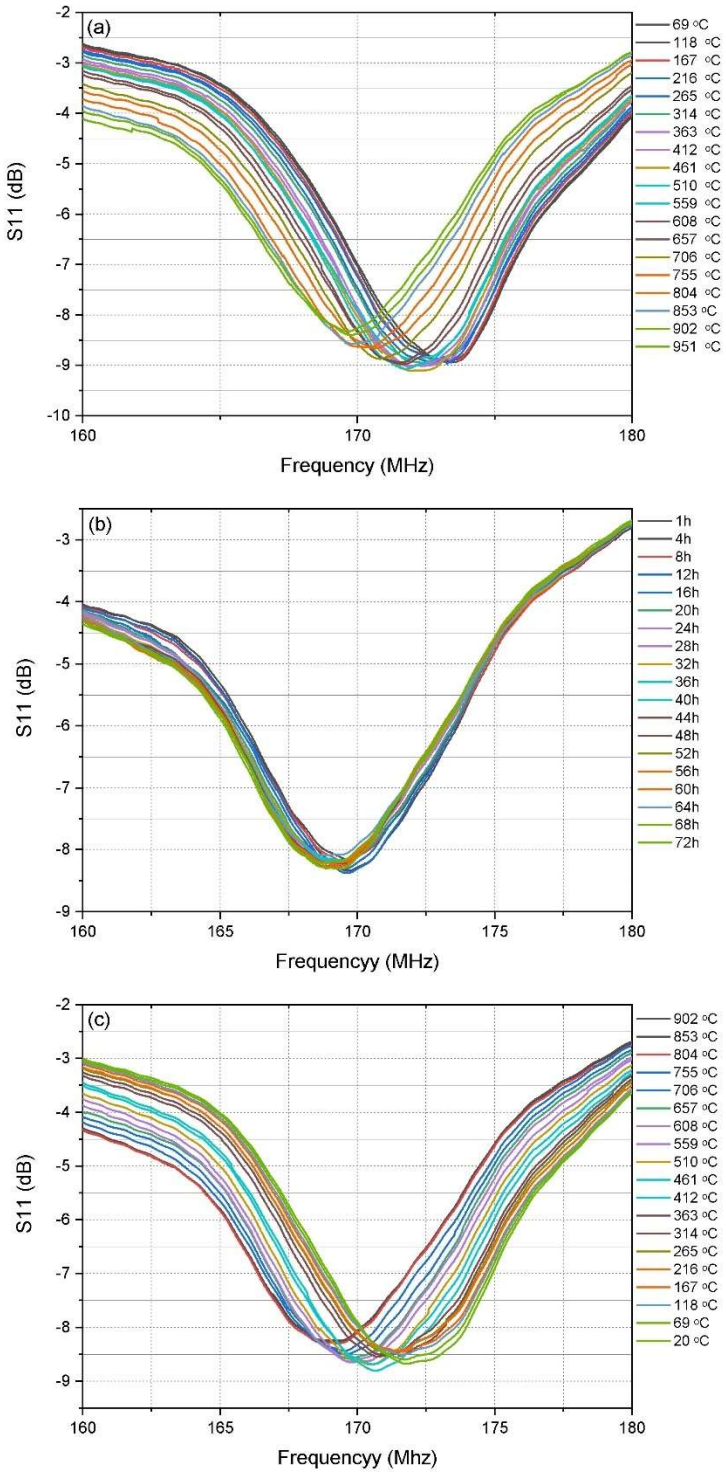

Figure 4.15: Passive wireless repeat sensor at high frequency (triple-layer platinum) heating, cooling, and maximum temperature hold furnace results. The top window (a) The multi-sensor response when heated from room temperature to 950°C at a rate of 120°C/hour with data captured in 30-minute intervals. (b) The multi-sensor response when held at 950°C for 72 hours with data captured in 20-minute intervals. And (c) The multi-sensor response when cooled from 950 °C to room temperature at a rate of -120 °C/hour with data captured in 30-minute intervals.

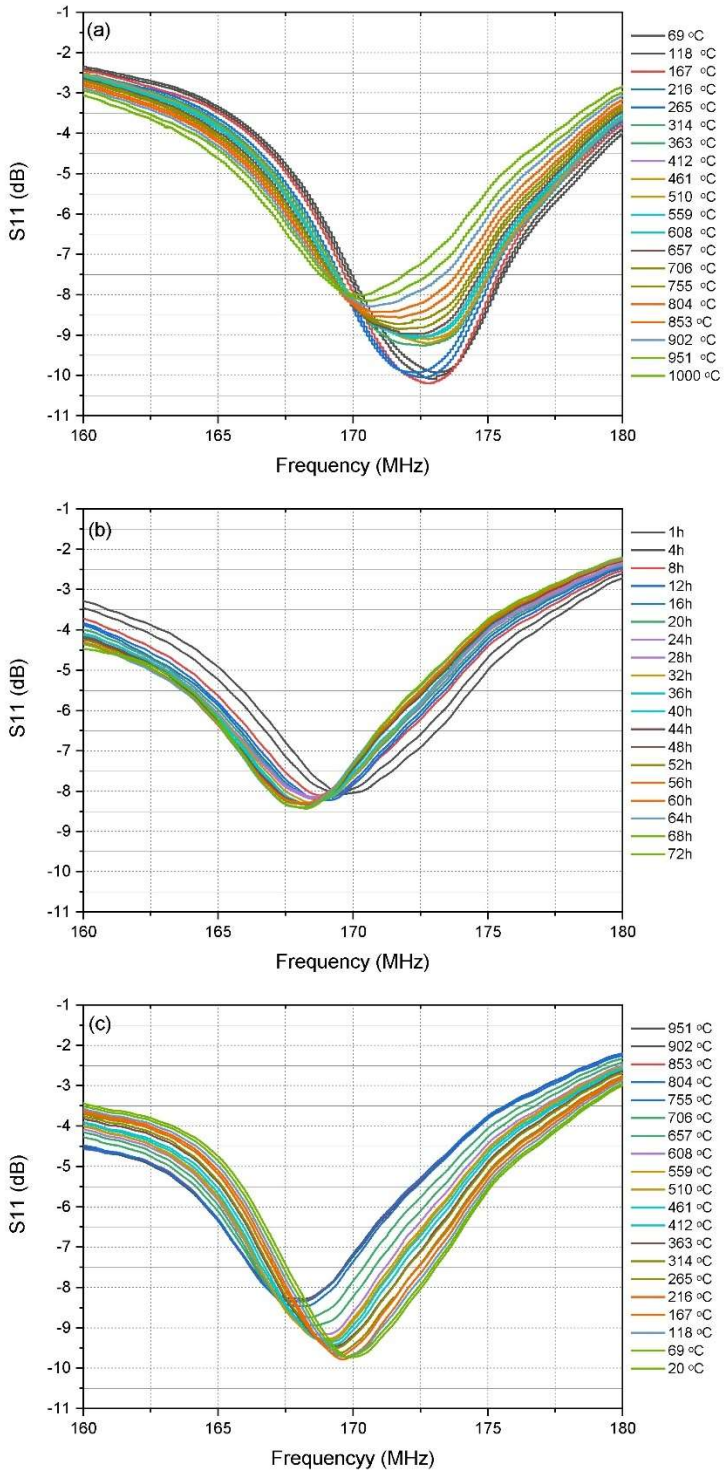

Figure 4.16: Passive wireless repeat sensor at high frequency (triple-layer platinum) heating, cooling, and maximum temperature hold furnace results. The top window (a) The multi-sensor response when heated from room temperature to 1000 °C at a rate of 120°C/hour with data captured in 30-minute intervals. (b) The multi-sensor response when held at 1000 °C for 72 hours

with data captured in 20-minute intervals. And (c) The multi-sensor response when cooled from 1000 °C to room temperature at a rate of -120 °C/hour with data captured in 30-minute intervals.

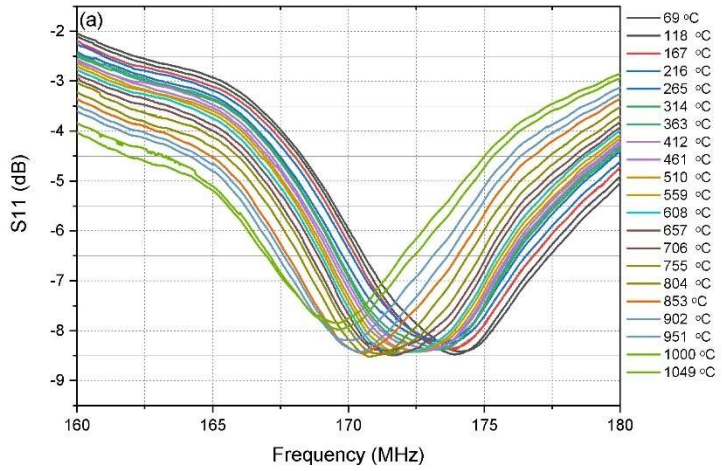

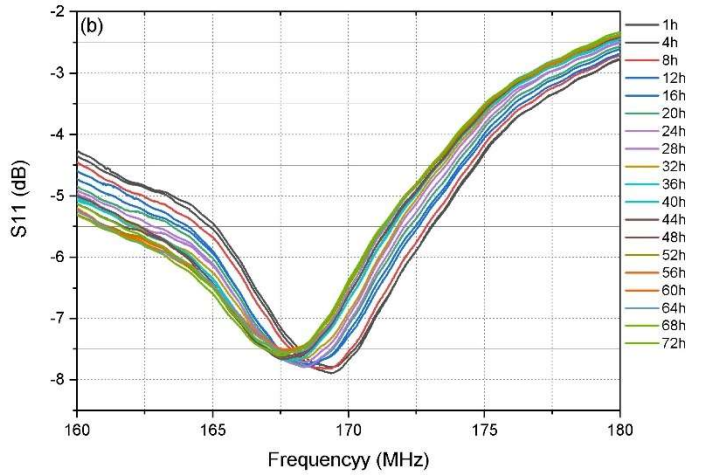

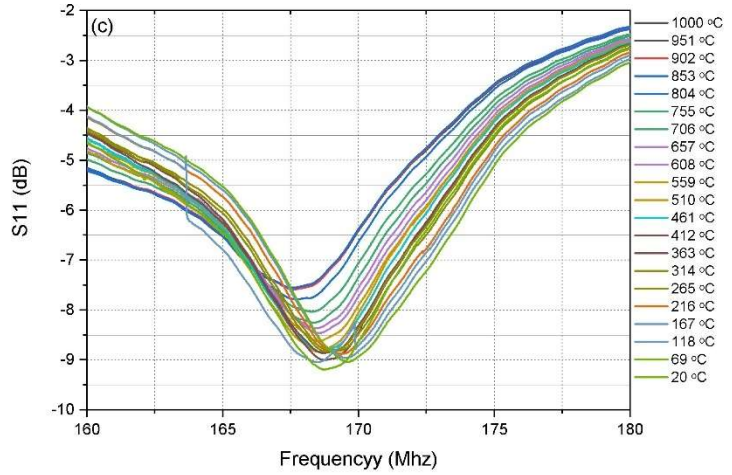

Figure 4.17: Passive wireless repeat sensor at high frequency (triple-layer platinum) heating, cooling, and maximum temperature hold furnace results. The top window (a) The multi-sensor response when heated from room temperature to 1050°C at a rate of 120°C/hour with data captured in 30-minute intervals. (b) The multi-sensor response when held at 1050°C for 72 hours with data captured in 20-minute intervals. And (c) The multi-sensor response when cooled from 1050 °C to room temperature at a rate of -120 °C/hour with data captured in 30-minute intervals.

Among the four evaluated temperatures, the 1000 °C condition exhibited the most balanced and reliable performance in terms of frequency shift, signal magnitude, and oxide growth without structural degradation. Compared to the lower temperatures of 900 °C and 950 °C, which showed limited oxide layer development and relatively modest signal changes, the 1000 °C setting offered apparent, measurable shifts in both frequency and magnitude, with a frequency change of 3.5 MHz and signal shift of around 1.5 dB across the whole cycle. In contrast, the 1050 °C condition, while showing the most significant shifts in some aspects, was compromised by spallation and delamination effects that interrupted signal integrity. SEM analysis at 1000 °C confirmed steady oxide formation reaching ~297 μm over 72 h, and no physical degradation of the sensing surface was observed. Therefore, 1000 °C was selected as the optimal operational point for calibration and further correlation.

To distinguish the sensor's inherent response from external influences such as the reader antenna and the substrate, a control experiment was conducted using only the antenna and substrate, without the sensor. By subtracting this baseline response from the full system measurements, a corrected signal was obtained, representing solely the effect of the sensing material. Figure 4.18 displays the deconvoluted signal peaks during the heating, isothermal hold, and cooling phases, along with the corresponding frequency shifts.

During the heating stage (Figures 4.18a and 4.18b), the corrected sensor response exhibited a frequency decrease from 173.25 MHz to 169.5 MHz, corresponding to a 3.75 MHz shift, along with a 1.8 dB reduction in signal magnitude. In the isothermal holding phase (Figures 14c and 14d), a 1.44 MHz frequency shift and a 0.48 dB decrease in magnitude were observed. In the cooling phase (Figures 14e and 14f), the sensor demonstrated a frequency recovery of 2.32 MHz and an increase in signal magnitude by 1.3 dB.

These results clearly demonstrate that the sensor itself—particularly the triple-layer platinum (Pt) structure—plays a dominant role in shaping the overall system response. The sharper frequency shifts and stronger signal variations observed in the corrected data confirm the sensor's effectiveness for high-precision corrosion monitoring applications.

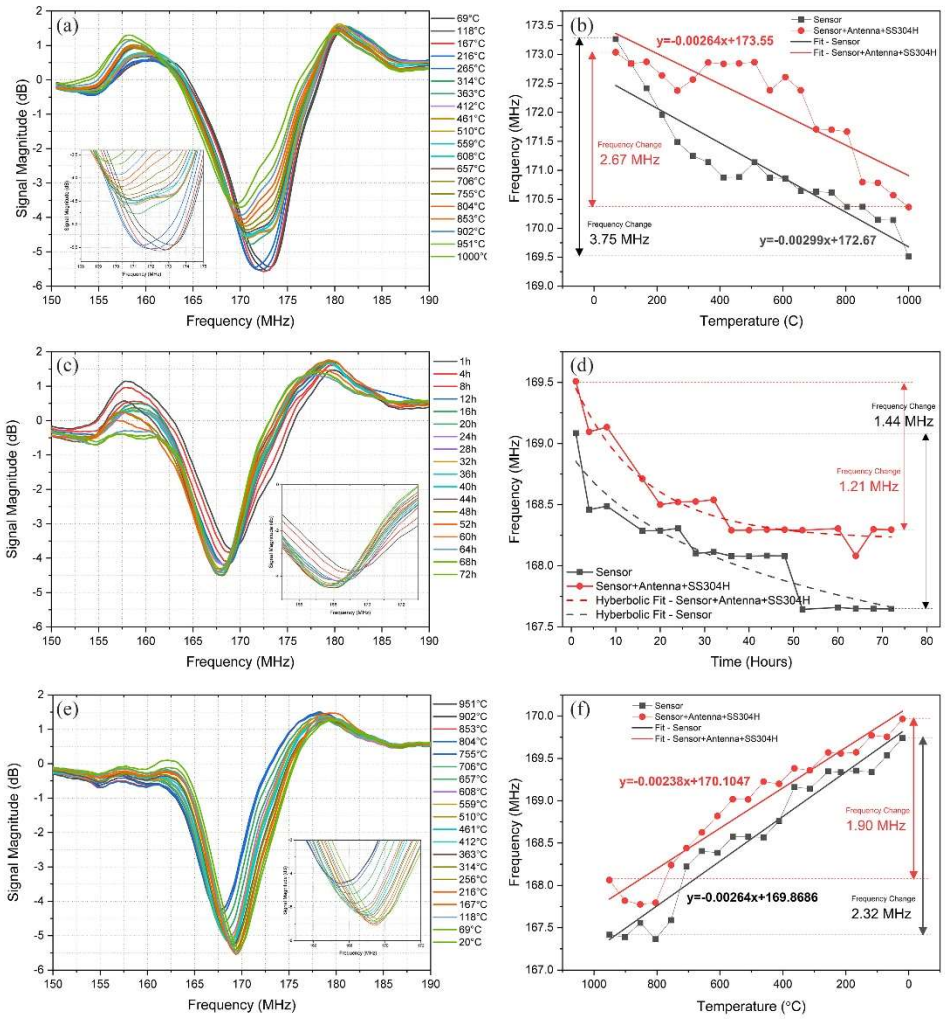

Figure 4.18: (a)–(c): Frequency response of the corrected sensor-only signal during the heating (ramp-up), isothermal hold, and cooling (ramp-down) phases at 1000 °C, (d)–(f): Comparison of the corrected sensor data and sensor + antenna + SS304H response as a function of temperature and time during the respective thermal cycles.

4.3.2. Performance Evaluation of Wireless Sensor Arrays at Low Temperature.

The layout presented in Figure 4.5 corresponds to real experimental data. In this setup, the sensor response was measured with the sensor positioned directly beneath the interrogator antenna at a fixed vertical distance. This distance was then systematically increased in 0.5 cm increments, up to a maximum offset of 3.0 cm from the center. The same experiment was repeated after rotating the sensor by 90 degrees. The results obtained from these real experimental measurements are shown in Figure 4.19.

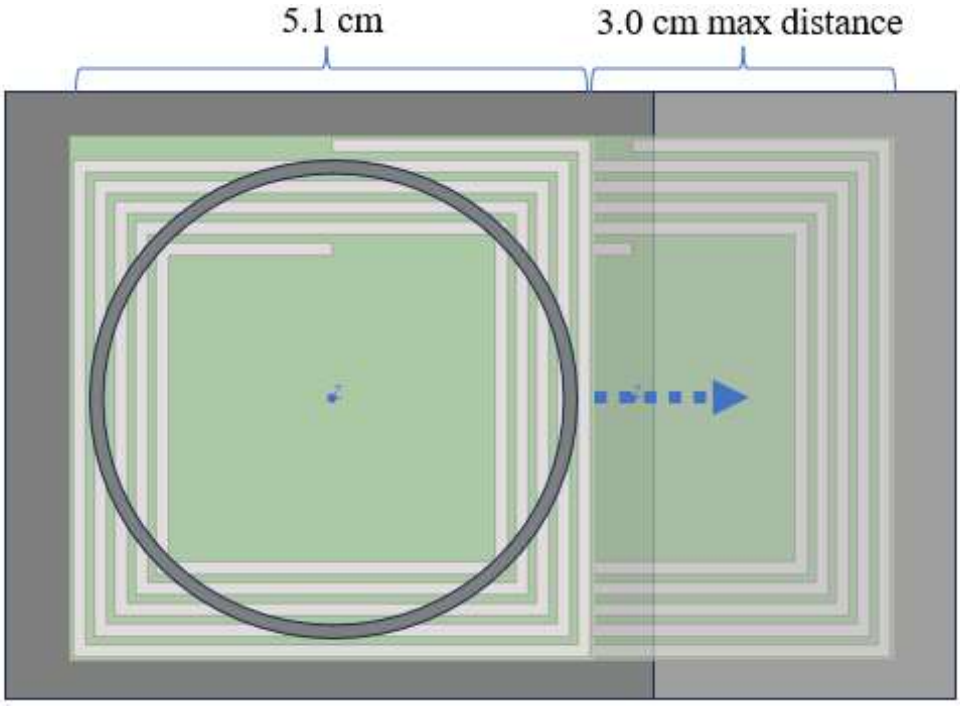

Figure 4.19: Physical layout of the horizontal distance vs. power room temperature experiment

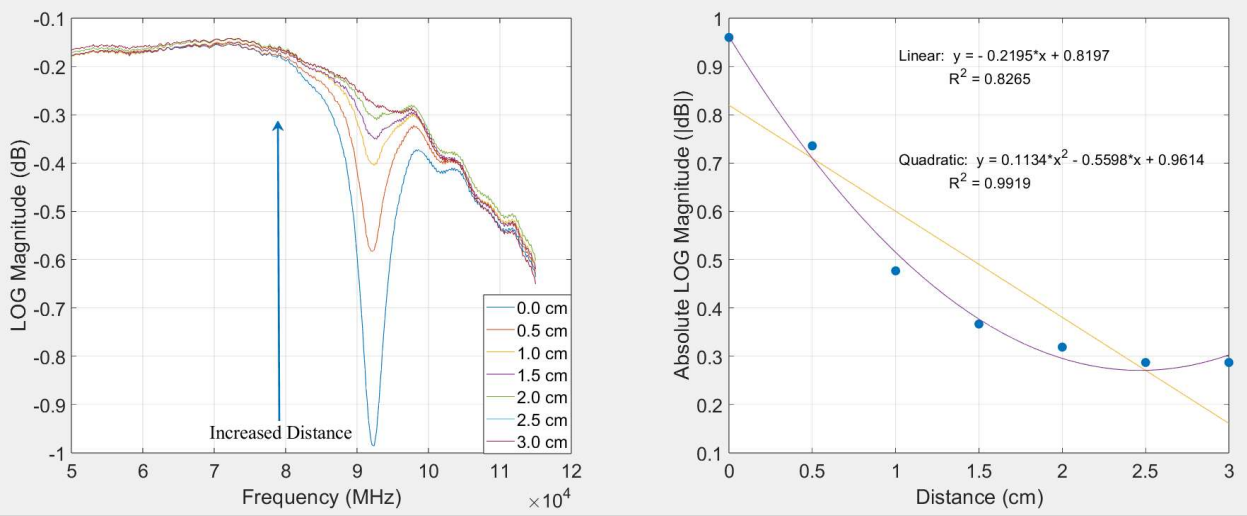

Figure 4.20: Results of the horizontal distance vs. power room temperature experiment. The figure 4.20 on the left shows the frequency response of the experiment, and the figure on the right shows the signal magnitude vs. distance from the sensor**.**

Like the vertical distance experiment, the horizontal distance experiment shows that as the sensor is offset from the center of the antenna, the signal magnitude decreases. Once again, this decrease in magnitude vs. distance can be fitted with great accuracy to a quadratic function with an error value of 0.9919, which indicates an excellent fit.

After the distance vs. power experiments, the last room-temperature experiments conducted were multi-sensor experiments. These experiments simply measured the response of two sensors side-by-side with and without ground planes. They would be measured with the interrogator antenna directly between them and with an added offset to both sides. Figures 4.21 and 4.22 display the physical layout of the multi-sensor experiments.

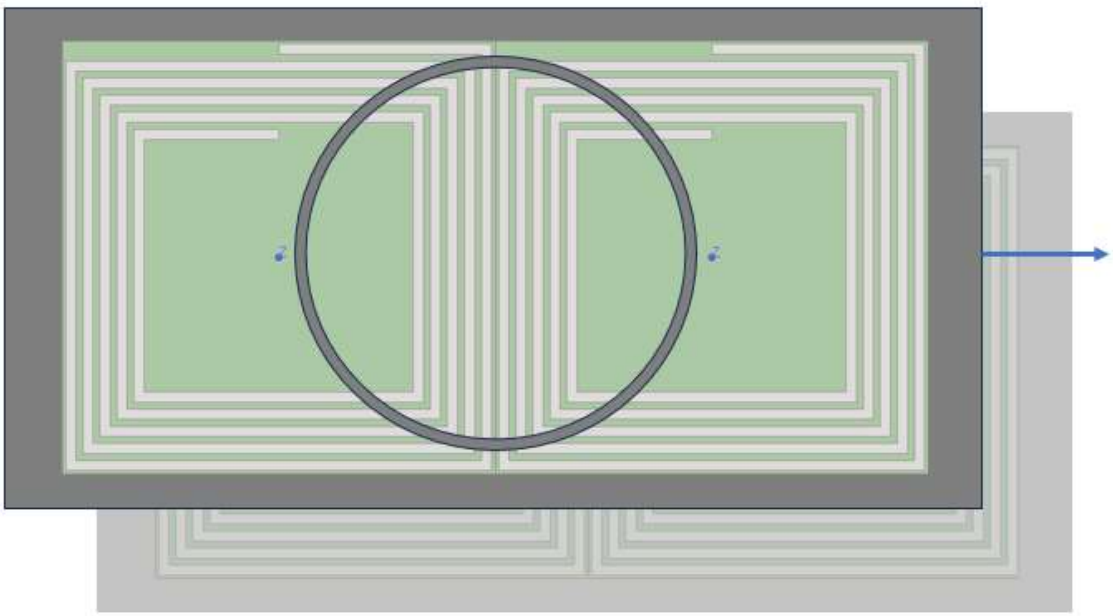

Figure 4.21: Physical layout of the multi-sensor experiments with ground planes.

As the diagram in Figure 4.21 indicates, the starting position of the sensors is balanced under the interrogator antenna. The position is the offset more to one of the sensors than the other in 0.5 cm increments to a max of 1.5 cm offset in either direction. The results of this experiment can be observed in Figure 4.22.

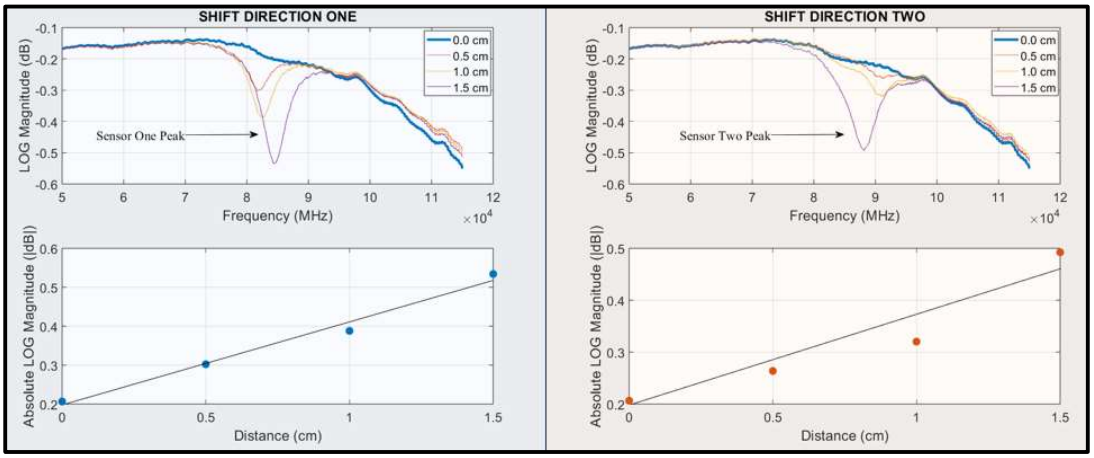

Figure 4.22: Results of the multi-sensor experiment with ground planes. The blue segment on the left represents shifting the sensor 0-1.5 cm in one direction, and the red segment on the right represents shifting the sensor 0-1.5 cm in the other direction.

As observed in Figure 4.23, when the sensors are centered (0.0 cm offset in either direction) there is no visible frequency peak. But as the sensors are shifted in either direction, we see the peak form corresponding to the sensor that is becoming more centered under the interrogator antenna. These results indicate that the sensor magnitudes are slightly too weak to be observed simultaneously when using a ground plane.

Though the sensor cannot be read simultaneously while using a ground plane, the next experiment repeats the process from the previous multi-sensor experiment except with no ground plane. This greatly increases the sensor signal magnitude. The layout of this experiment and the results can be observed in Figure 4.24.

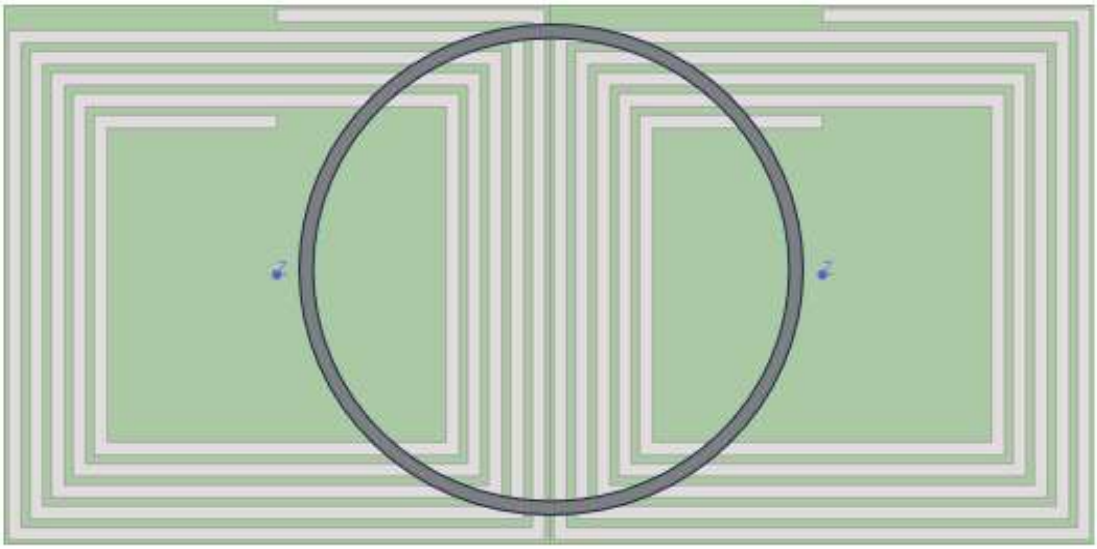

Figure 4.23: Physical layout of the multi-sensor experiments with NO ground planes.

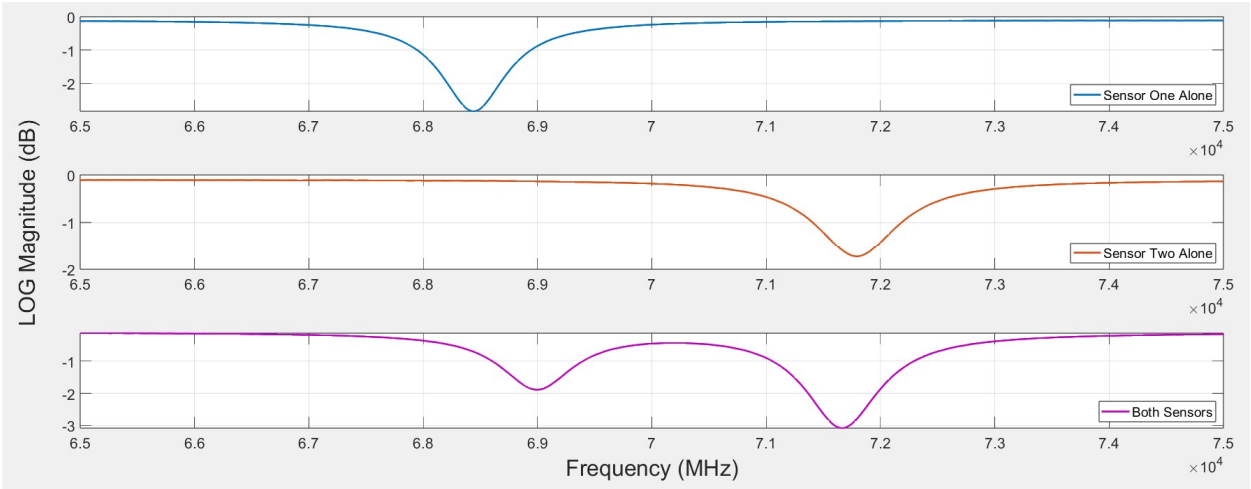

Figure 4.24: Results of the multi-sensor experiment with NO ground planes. The top figure represents the sensor reading with one sensor removed at the offset displayed in Figure 4.9, the middle figure represents the same process with the other sensor, and the bottom figure displays the reading of both the sensors simultaneously.

The results displayed in Figure 4.10 indicate that both sensors can be simultaneously read when no ground plane is used. This provides enough room temperature evidence to begin testing two sensors simultaneously at higher temperatures for dual-sensor temperature sensing.

4.3.3. Performance Evaluation of Wireless Sensor Arrays at High Temperature.

Figure 4.25 presents the results of the passive wireless sensor during the heating, cooling, and maximum temperature hold phases for the copper ground plane with two sensors. In the heating stage illustrated in Figure 4.25(a), both sensors exhibited a decrease in peak magnitude and a downward shift in frequency. The corrosion and temperature sensor experienced a larger magnitude reduction and frequency shift compared to the temperature-only sensor. This outcome was anticipated, as the dielectric constant of the alumina increases with heating, leading to a corresponding downward frequency shift and decrease in magnitude. These findings align with the simulation results shown in Figure 2.7 (a).

During the maximum temperature hold stage depicted in Figure 4.25(b), the corrosion and temperature sensor displayed an increase in magnitude along with a decrease in frequency. In contrast, the temperature-only sensor showed a minimal increase in magnitude without any change in frequency. This trend corresponds to the simulation results in Figure 2.7 (b), which indicated that an increase in oxide thickness on the ground plane results in a rise in magnitude and a decline in frequency of the sensor response, primarily in a linear manner. The temperature-only sensor did not exhibit this behavior, as it was not in contact with the copper and therefore did not undergo frequency shifting due to corrosion effects.

Finally, the cooling stage depicted in Figure 4.25 (c) shows a reversal of the heating stage response, with an increase in magnitude and an upward frequency shift. This behavior was expected because the dielectric constant of the alumina rises during heating and decreases during cooling, with minimal hysteresis error.

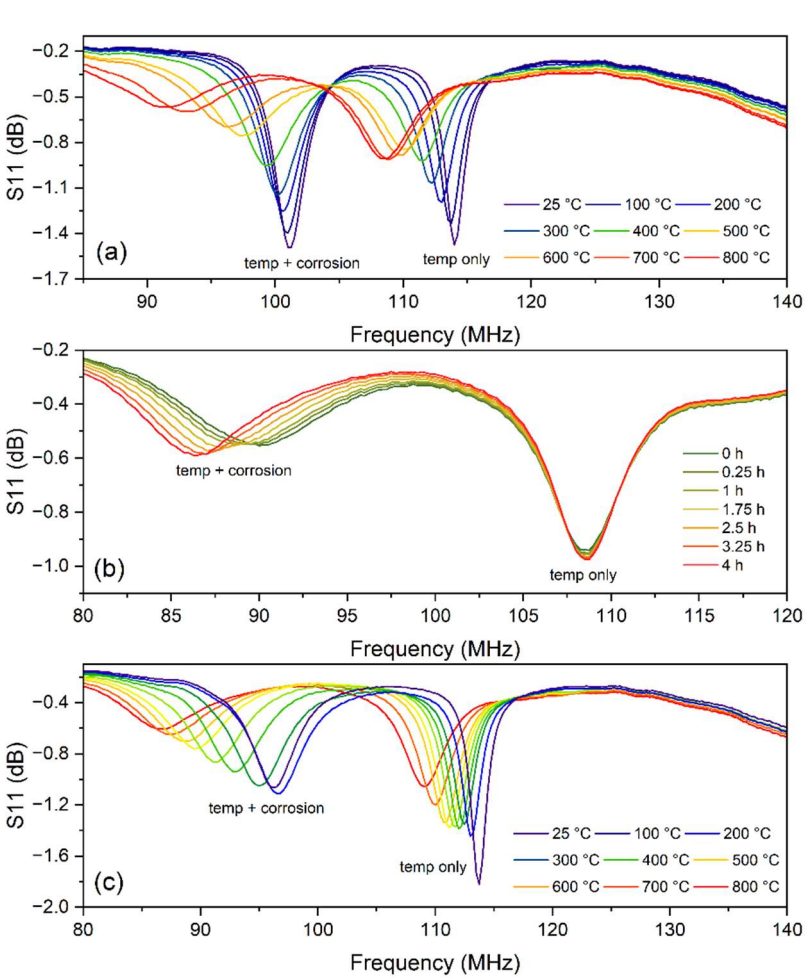

Figure 4.25: Passive wireless multi-sensor heating, cooling, and maximum temperature hold furnace results. The top window **(a)** The multi-sensor response when heated from room temperature to 800°C at a rate of 120°C/hour with data captured in 30-minute intervals. **(b)** The multi-sensor response when held at 800°C for 4 hours with data captured in 20-minute intervals. And **(c)** The multi-sensor response when cooled from 800°C to room temperature at a rate of -120°C/hour with data captured in 30-minute intervals.

Figure 4.26 illustrates the results of passive wireless sensor heating, cooling, and maximum temperature hold for a stainless steel ground plane. In the heating phase depicted in Figure 4.26(a), the sensor's peak experienced a reduction in magnitude of about 0.19 dB and shifted in frequency from 83 MHz to 78 MHz. This outcome was anticipated as the sensor heated, leading to an increase in the dielectric constant of the alumina, resulting in the observed downward shift in frequency and decrease in magnitude. These findings aligned with the simulations shown in Figure 2.7(a).

During the maximum temperature hold stage in Figure 4.26(b), the sensor's peak magnitude rose by 0.05 dB, with no significant frequency shift noted. These outcomes correspond with the general trend observed in the simulation results in Figure 2.7(b), indicating that a greater oxide thickness on the sensor's ground plane leads to an increase in magnitude. However, this does not correlate with a frequency shift. This lack of frequency change may be attributed to the high level of signal peak attenuation, making it harder to distinguish from background noise.

In the cooling phase shown in Figure 4.26(c), where no defects were present, the behavior mirrored that of the heating phase: the magnitude increased by about 0.2 dB, and there was an upward frequency shift from 78 MHz to 88 MHz. This result aligns with expectations, as the dielectric constant of the alumina decreases during cooling after being heightened during heating.

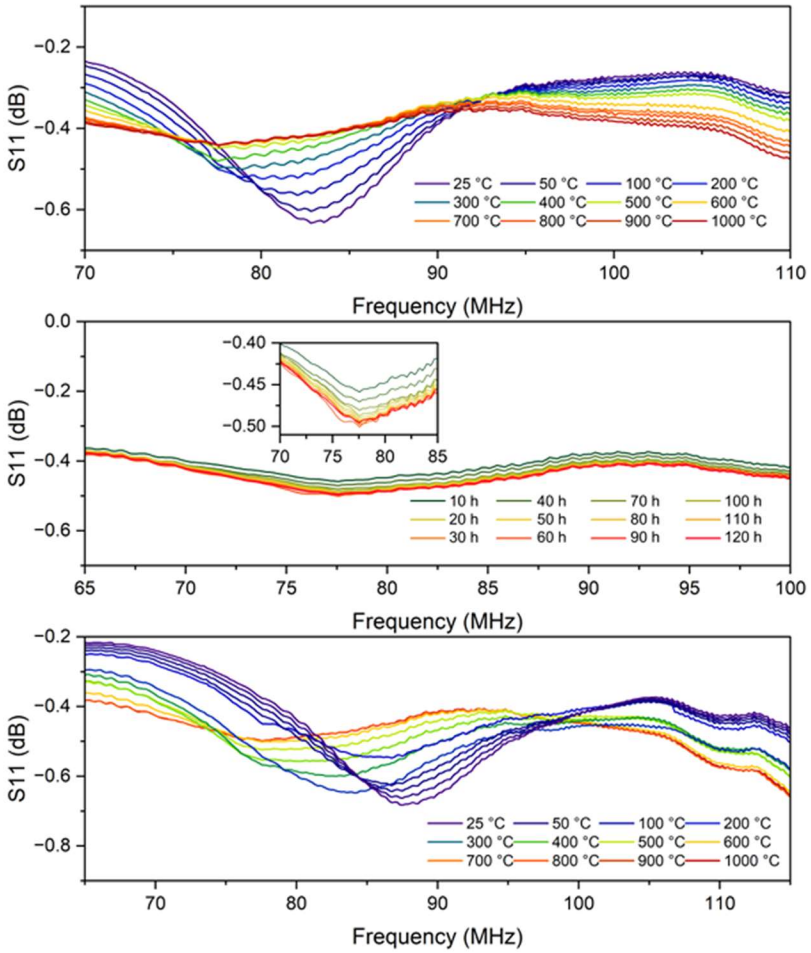

Figure 4.26: Passive wireless sensor heating and cooling furnace results on the stain less steel ground plane. (a) The sensor heating stage from room temperature to 1000 °C at a rate of 120 °C/h. (b) The sensor maximum temperature hold at 1000 °C for 120 h. (c) The sensor cooling stage from 1000 °C to room temperature at a rate of-120 °C/h

Conclusion

This study comprehensively evaluated the performance of singular and array-based passive wireless LC sensors for high-temperature corrosion and structural health monitoring applications. Through a combination of experimental validation and modeling support, the results demonstrated the sensors' capability to track temperature-induced and corrosion-driven changes in real time, with distinct frequency and magnitude signatures.

Singular sensor tests conducted on Cu110 and SS304H substrates revealed clear correlations between oxide growth and sensor responses. For Cu110, the frequency shift during isothermal oxidation at 800 °C aligned closely with the TGA-derived oxide thickness (~189 μm), confirming that the passive sensor can serve as a proxy for oxidation kinetics. The results also confirmed the parabolic growth law, with the measured activation energy (76.6 kJ/mol) falling within the expected range reported in the literature. Similarly, SS304H exhibited progressive oxide layer growth at elevated temperatures, especially at 1000 °C and 1050 °C, where the activation energy (173.3 kJ/mol) was consistent with reported values. The sensors successfully captured the evolution of multi-layer oxide scales and mechanical degradation, evidenced by frequency reductions and amplitude losses that correlated with crack initiation and spallation.

The study further explored the effects of pre-existing surface defects on sensor performance. Experiments revealed that increasing defect severity led to distinct signal anomalies, particularly during the isothermal hold and cooling phases, indicating degradation of the signal due to spallation. These findings reinforce the sensor's sensitivity not only to temperature and oxidation but also to mechanical failure modes at the metal-oxide interface.

The performance of wireless sensor arrays was also systematically assessed. At low temperatures, dual-sensor configurations revealed that antenna alignment and horizontal offset had a significant influence on signal strength, with interference minimized when no ground plane was used. These findings provided critical insight for high-temperature multi-sensor tests. Under high-temperature conditions, the corrosion-temperature sensor showed more pronounced frequency and magnitude shifts compared to the temperature-only sensor, enabling effective differentiation between thermal and oxidative effects. Particularly at 800°C, the temperature-corrosion sensor displayed expected trends in signal behavior, aligning with simulation data, while the temperature-only sensor remained largely unaffected.

Furthermore, the study investigated sensor response in the higher frequency range (160–180 MHz), where triple-layer Pt inductors offered improved spectral clarity. Among all temperature conditions tested (900–1050 °C), 1000 °C emerged as the optimal calibration point, exhibiting strong linearity between oxide thickness and frequency shift (~3.5 MHz shift, ~1.5 dB signal change), without experiencing the spallation observed at 1050 °C. These findings validate the potential of the high-frequency triple-layer Pt sensor design for long-term stability in harsh environments.

In summary, the results demonstrate that the developed passive wireless sensors provide a robust, non-contact method for monitoring both temperature and corrosion-induced damage. The strong correlation between oxide thickness and sensor signal enables quantifiable tracking of material degradation. These findings lay the groundwork for further development of passive sensor arrays and advanced signal processing algorithms for deployment in industrial high-temperature environments such as power plants, gas turbines, and boilers.

Task 5: Through-Wall Signal Transmission for RFID Wireless Sensor Testing

5.1 Introduction:

This study involves a detailed analysis of the passive wireless sensors designed in Task 2 and inserted into metal tubes that are various thicknesses (1-5 mm). The interrogator antenna will be placed outside the closed tube, and the relative signal transfer efficiency will be measured for each sensor design. The optimal sensor and antenna designs demonstrating the best performance will be transferred to Subtask 5.2. The sensor/antenna pairs that perform the best for specific tube thicknesses and compositions will be evaluated in a high-temperature test stand up to 1300 °C. Additionally, similar isothermal and cyclic steam exposure tests, as used in Subtasks 4.1 and 4.3, will be conducted for sensors directly deposited onto the metal tubes, along with a kinetic study to relate sensor signals to through-wall data compared to previous parallel transmission data.

Subtask 5.1 Through-Wall Performance Evaluation Sensors at Low Temperature

The passive wireless sensor designed in Task 2 will be used int his task. The singular sensors will be fixed parallel to the metal tube wall (but not deposited to the wall). Metal tubes with various thicknesses (1-5 mm) and compositions will be utilized. Various metals (with different magnetic properties, such as low-chromium ferritic steel (SA213 T22) and high-chromium austenitic steel (SA213 TP304H) tubes, will be tested. The interrogator antenna will be placed outside the closed tube, and the relative signal transfer efficiency will be measured for each sensor design. The optimal sensor type and antenna design will be transferred to Subtask 5.2.

Subtask 5.2 Through-Wall Performance Evaluation of Sensors at High Temperature.

The sensor/antenna pairs that show the best performance in Subtask 5.1 for a specific tube thickness and composition will be tested in the high-temperature (up to 1300^{o}C) test stand. Similar isothermal and cyclic exposure used in Subtask 4.1 and 4.3 will be completed for the sensors directly deposited onto the metal tube. A similar kinetic study will be completed in order to relate the sensor signal to the through-wall data compared to the previous parallel transmitted sensor data.

5.2 Experimental Methods:

5.2.1 Through-Wall Performance Evaluation Sensors at Low Temperature.

To evaluate the electromagnetic transmission characteristics of passive wireless LC sensors in metallic environments, a fixed-distance measurement setup was employed. The sensor used in this study was a chipless LC-type resonator operating around 150 MHz and designed for near-

field inductive and capacitive coupling. The sensor was screen-printed using silver-based conductive ink onto a non-conductive ceramic substrate. The interrogator antenna was positioned at a constant distance of approximately 1 cm from the sensor. The sensor was tested in four different configurations: in open air, and enclosed behind stainless steel (3.50 mm), galvanized steel (3.35 mm), and aluminum (0.70 mm) shields. A vector network analyzer (VNA) was used to record the S11 reflection parameter in each configuration. Background measurements without the sensor were also collected as a baseline.

5.2.2 Through-Wall Performance Evaluation of Sensors at High Temperature

The experimental campaign for Task 5.2 was designed to evaluate the through-wall sensing capability of the most effective sensor/antenna pairs identified in Subtask 5.1 under high-temperature conditions. Initially, multiple sensor and antenna configurations were screened using benchtop through-wall signal transmission tests at temperatures up to 500 °C. Metal tubes with varying thicknesses (1–5 mm) and compositions, including SA213 T22 and SA213 TP304H, were employed to determine the optimal sensor/antenna design capable of maintaining wireless communication in obstructed environments. Signal quality was assessed by placing metallic barriers between the sensor and the interrogator antenna and quantifying the resonance magnitude and frequency shift. Following performance ranking from these low-temperature tests, the best-performing sensor/antenna pairs were selected for high-temperature evaluation in a controlled furnace environment capable of reaching 1300 °C. In this phase, sensors were directly deposited onto the exterior surface of metal tubes using screen-printing or tape-casting methods. The interrogator antenna was placed outside the furnace, allowing signal interrogation through the tube wall, simulating real-world deployment conditions where direct visual access is not feasible. The thermal exposure protocol followed similar isothermal and cyclic conditions as described in Subtasks 4.1 and 4.3. Each test involved ramping the furnace temperature at a rate of 2 °C/min to the target hold temperature (ranging from 600 °C to 800 °C) and maintaining the setpoint for up to 120 hours. During this period, sensor response data were continuously captured using a Vector Network Analyzer (VNA), and MATLAB scripts were employed to automate the acquisition process with signal averaging techniques to reduce noise. Frequency and magnitude shifts in the S11 parameter were analyzed as indicators of oxide growth and crack formation on the metal surface beneath the sensor. Complementary thermogravimetric analysis (TGA) and scanning electron microscopy (SEM) were performed to characterize the oxidation kinetics and correlate physical degradation with sensor signal changes. In particular, oxide layer thickness and morphology were evaluated to determine the extent of corrosion and establish a relationship between the observed resonant frequency shifts and the corresponding through-wall degradation behavior. The outcomes of this experimental protocol are intended to validate the feasibility of through-wall corrosion monitoring at elevated temperatures and provide a framework for deploying passive wireless sensors in harsh industrial environments such as coal-fired boilers.

5.3 Results and Discussion:

5.3.1 Through-Wall Performance Evaluation of Sensors at High Temperature.

The through-wall performance of passive wireless LC sensors was investigated by evaluating the sensor's ability to communicate through various metallic materials. As shown in **Figure 5.1**, the background signal from the interrogator antenna with no sensor present exhibited no resonance at the expected frequency. When the LC sensor was placed in air at a distance of 1 cm from the antenna, a clear resonant peak was observed at approximately -4.0 dB (**Figure 5.2**), confirming strong near-field signal transmission.

Figure 5.1: Background measurement of interrogator antenna with no sensor present.

Figure 5.2: Measured S11 response of LC sensor through air.

However, when metallic shields were introduced between the sensor and the antenna—specifically, 3.50 mm stainless steel (**Figure 5.3**), 3.35 mm galvanized steel (**Figure 5.4**), and 0.70 mm aluminum (**Figure 5.5**)—the resonant signal was entirely suppressed, with the S11 response indistinguishable from the background. These results confirm the well-known shielding effect of metals, which significantly attenuate electromagnetic waves, particularly in the low-frequency range used by LC sensors.

Figure 5.3: Measured S11 response of LC sensor through stainless steel.

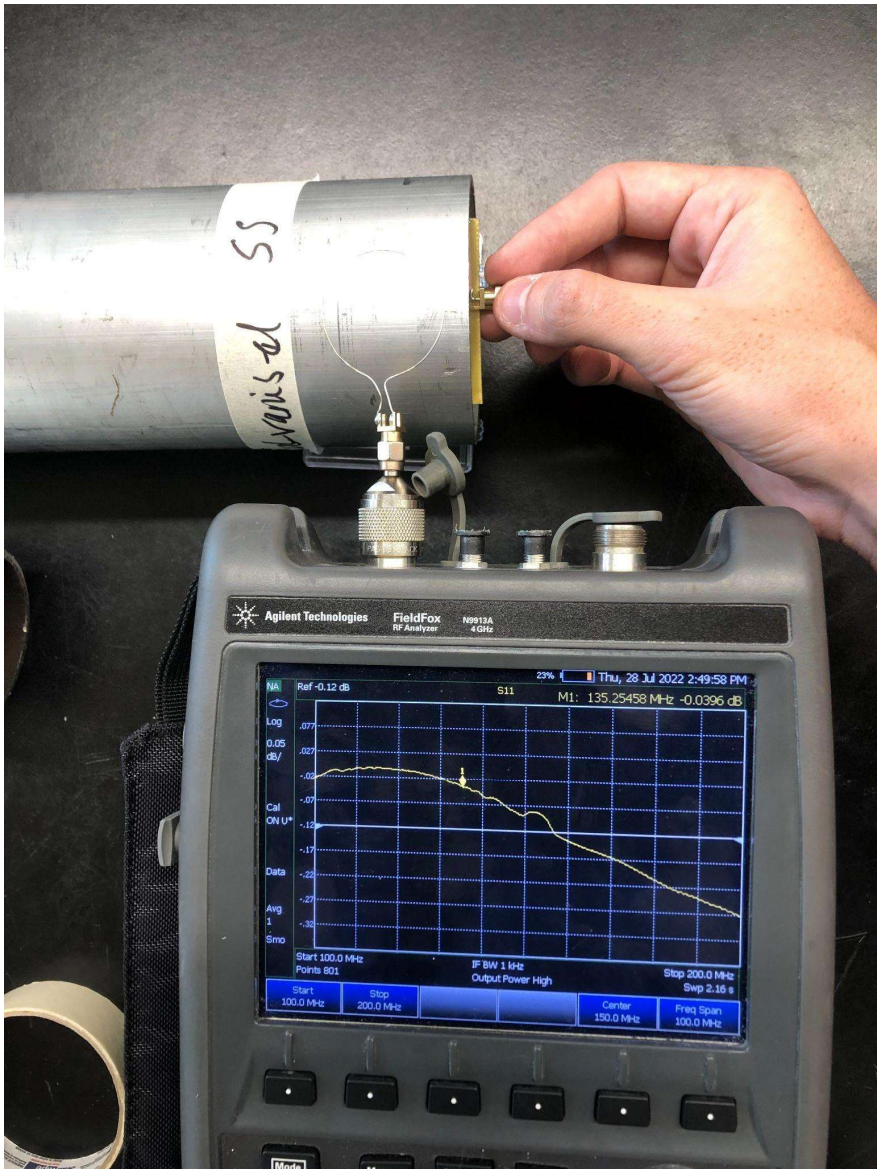

Figure 5.4 : Measured S11 response of LC sensor through galvanized steel.

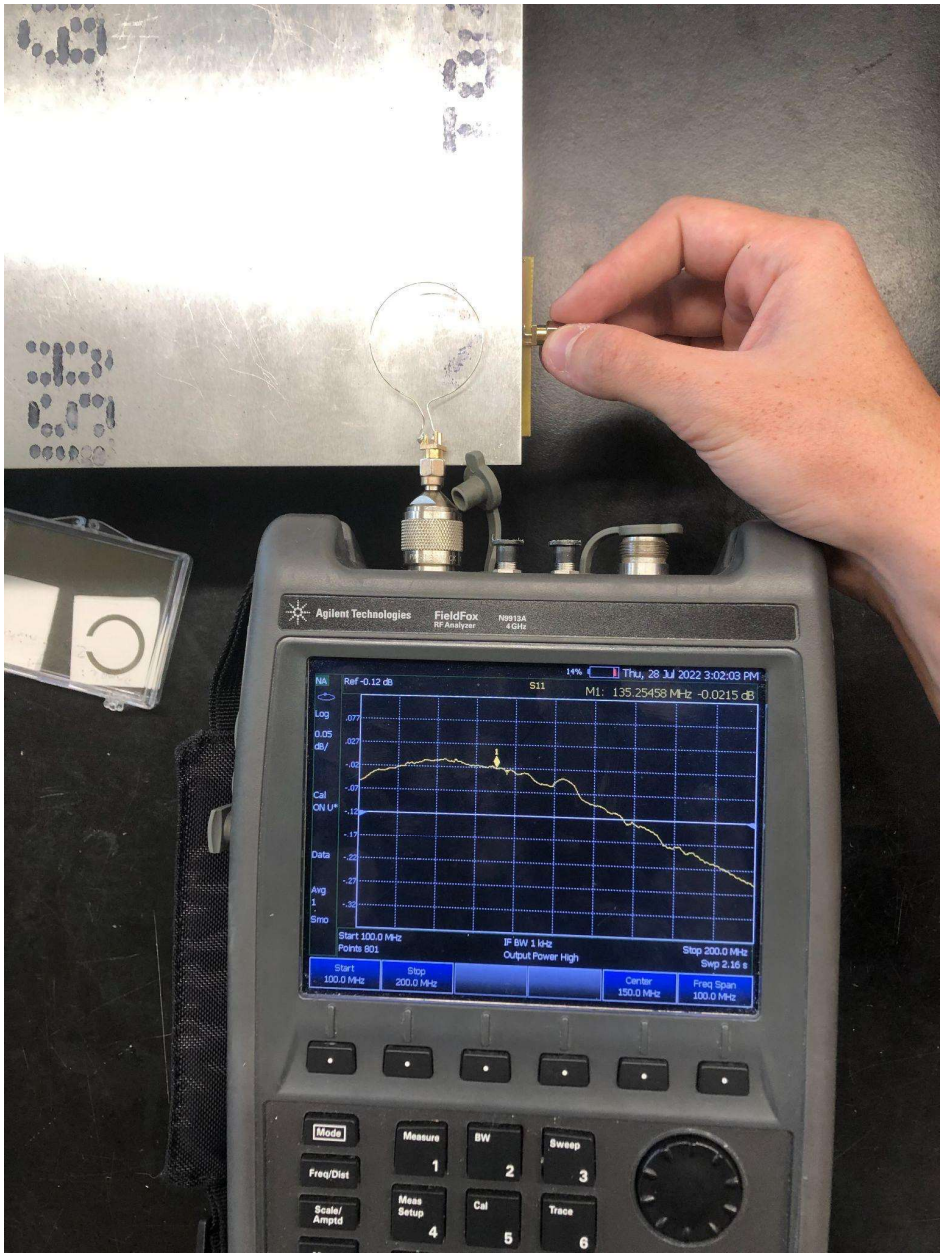

Figure 5.5: Measured S11 response of LC sensor through aluminum.

There was no readable sensor response through any tested metallic materials. Metal materials are generally used as shielding because EM waves cannot penetrate them easily. That is clearly what is being demonstrated here as well. It is highly unlikely the sensor will be able to read through metal shields, especially being a low-power passive device.

A method for reading a sensor through a stainless-steel wall was determined through simulation, but there was no method of testing this experimentally determined. A method was determined using alumina as a substitute for the oxidation layer so this phenomenon could be tested at room

temperature. The previous method involved simulating the sensor when there was oxidation growth ONLY on the bottom of the sensor. This represents the sensor being on the outside of the high temperature component, not the inside. So, to replicate this experimentally, the sensor was read at room temperature with nothing on its ground plane, then layers of alumina were then added to simulate the effect of a corrosion layer. This was also replicated in ANSYS as well so the simulation and experiment could be compared. The results of this can be observed in Figure 5.6 .

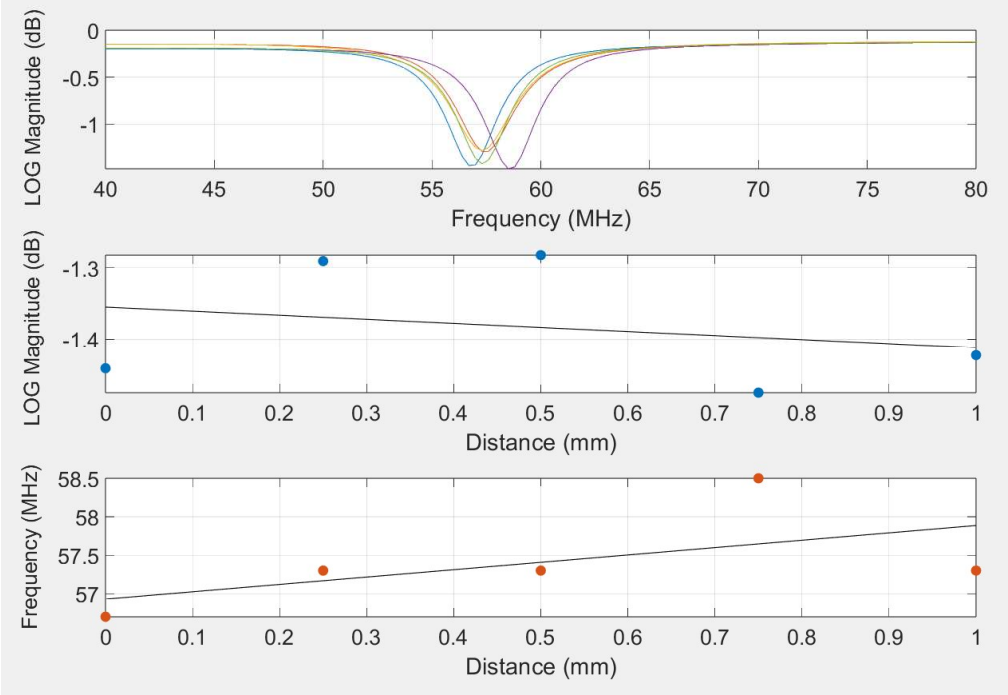

Figure 5.6: ANSYS simulation results of measuring the sensor response with increased thicknesses of alumina being added to the bottom of the ground plane. The top figure is the frequency response, the middle figure is the magnitude vs. thickness of alumina, and the bottom layer is the frequency vs. thickness of alumina.

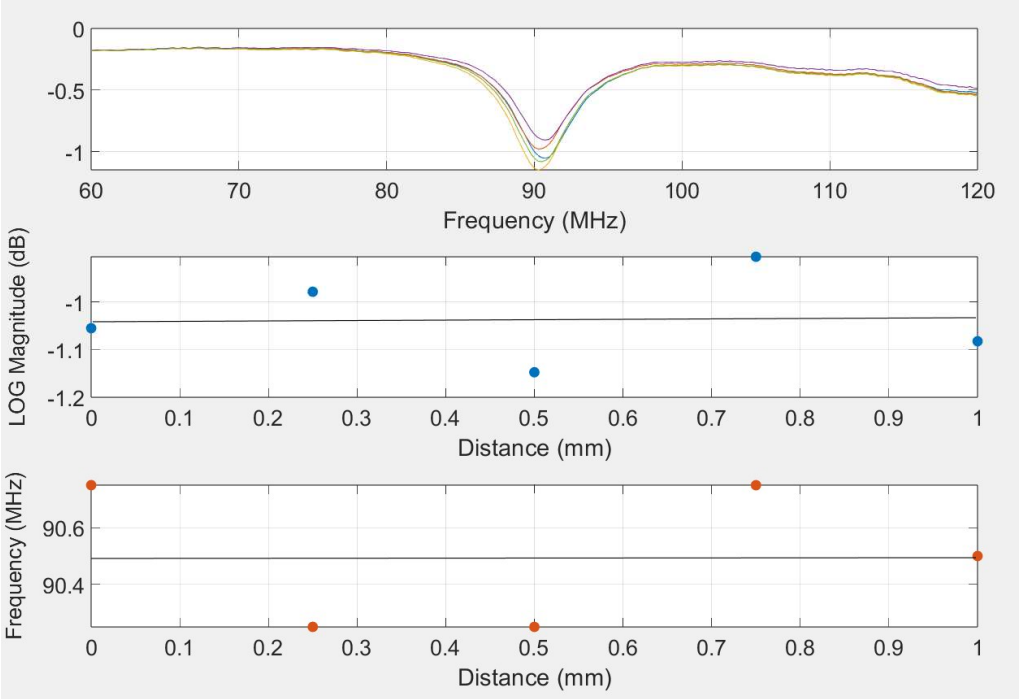

Figure 5.7: Experimental results of measuring the sensor response with increased thickness of alumina being added to the bottom of the ground plane. The top figure is the frequency response, the middle figure is the magnitude vs. thickness of alumina, and the bottom layer is the frequency vs. thickness of alumina.

It can be observed that through simulation and experimentation in Figures 5.6-5.7, using alumina as an oxidation substitute there is no strong observable trend as the alumina layers are increased. At this point it is not completely clear whether this phenomenon will work with oxidation as there is no method yet determined to experimentally replicate the initial ANSYS simulations.

Based on the lack of detectable signal transmission through any tested metallic material, this experimental path was terminated. Subsequently, the focus shifted to sensor configurations where the interrogator antenna passes directly over the dielectric surface, enabling reliable near-field signal acquisition. These findings clearly define the limitations of passive LC sensors in through-wall applications and underscore the need for alternative antenna and sensor designs—such as far-field multi-resonance patches—for embedded environments involving metal enclosures.

5.3.2 Through-Wall Performance Evaluation of Sensors at High Temperature.

The through-wall sensing performance of the optimized sensor/antenna configurations was evaluated at high temperatures to assess their viability in real-world applications such as coal-fired boiler environments. This evaluation builds upon the findings of Subtask 5.1, where multiple metallic barriers (galvanized steel, stainless steel, and aluminum) of varying thicknesses were tested to identify the most effective sensor/antenna pairings under obstructed conditions.

Figure 5.8 illustrates the signal degradation observed when various metallic barriers were placed between the sensor and interrogator antenna. As shown, the presence of a metallic shield significantly attenuates the S11 signal, confirming the critical challenge of through-wall interrogation in metallic enclosures.

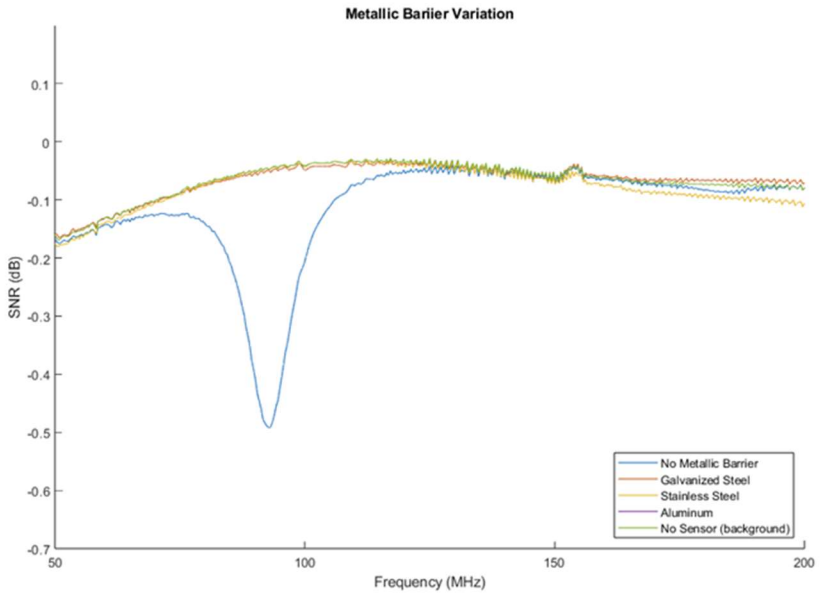

Figure 5.8: Experimental results of testing different metallic barriers obstructing the view of the sensor and the interrogator antenna. The chosen materials were 3.5 mm galvanized steel, 3.35 mm stainless steel, and 0.7 mm aluminum.

To overcome this, an alternative configuration was explored—placing the sensor on the opposite side of the metal wall while still utilizing the metal as the ground plane. ANSYS simulations (Figures 5.9, 5.10 , and 5.11) predicted that measurable and consistent shifts in resonant frequency would occur in response to oxide growth localized on the inner wall of the metallic tube, even when the interrogator antenna remained outside the furnace.

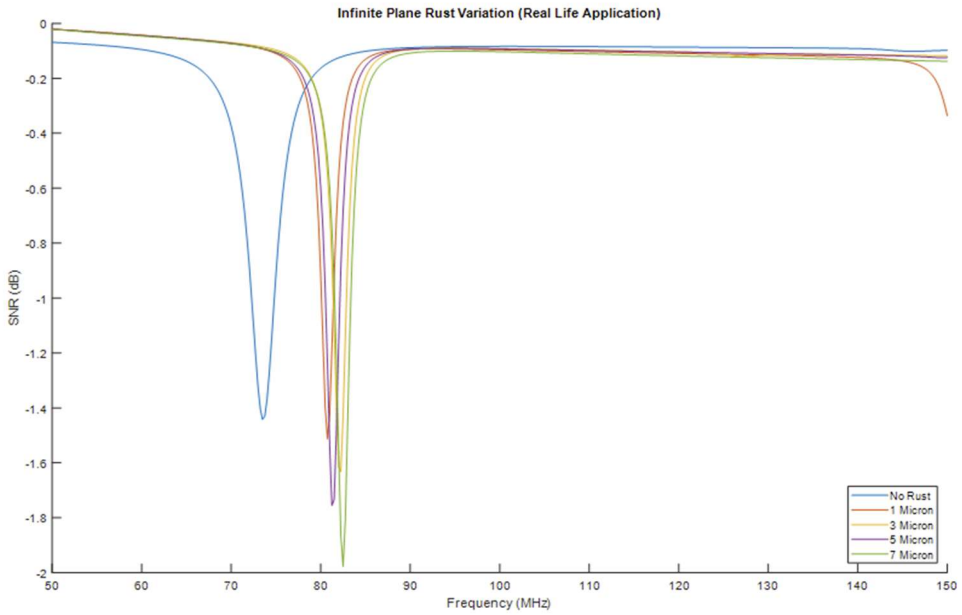

Figure 5.9. ANSYS simulation results of the category 1 thin oxide growth on the **through-wall testing environment** ANSYS model (oxidation only on the bottom).

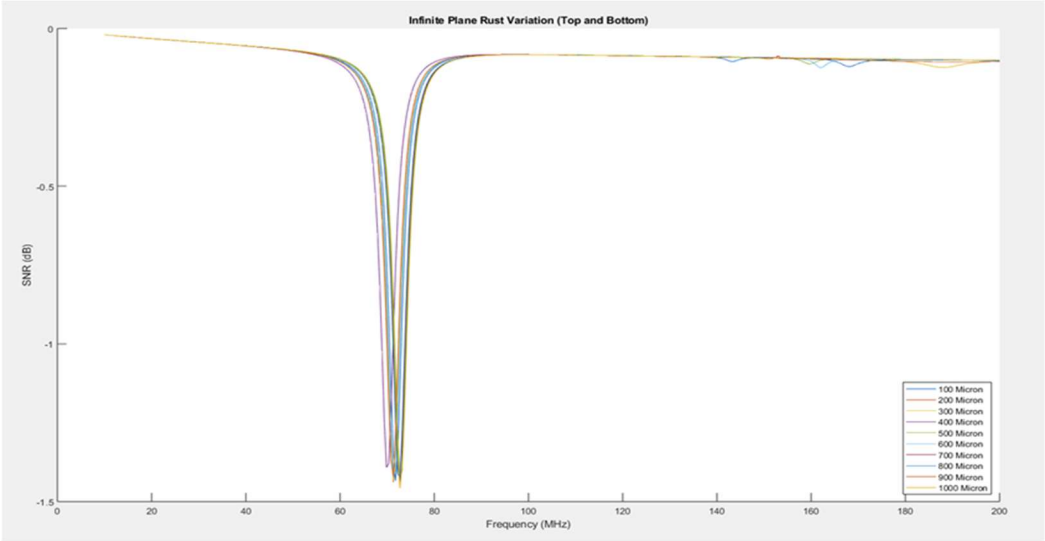

Figure 5.10. ANSYS simulation results of the category 2 thick oxide growth on the **through-wall testing environment** ANSYS model (oxidation only on the bottom).

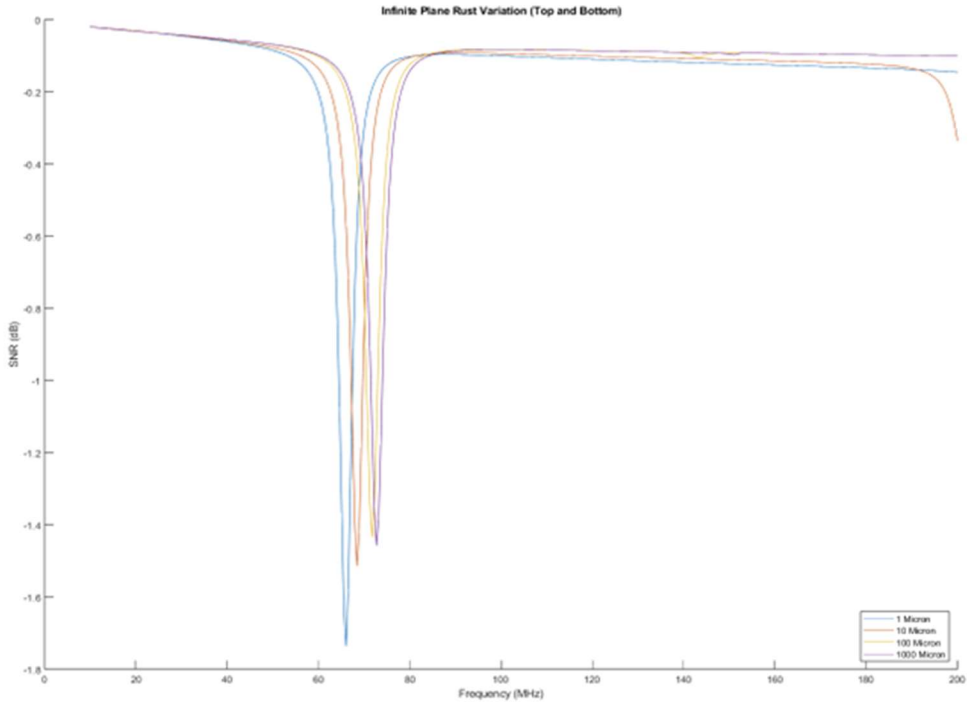

Figure 5.11. ANSYS simulation results of exponential (1 µm, 10 µm, 100 µm, and 1,000 µm) oxide growth using the **through-wall testing environment** ANSYS model (oxidation only on the bottom).

Experimental verification of this setup was initiated using stainless steel SS304H tubes, where sensors were pseudo-bonded to the tube surface. Isothermal holds at 600°C and 700°C were conducted for up to 120 hours. The sensor signal was captured in real-time using a Vector Network Analyzer, and post-processed using a MATLAB script that averaged each data point from 100 readings to suppress environmental noise.

In Figure 5.12, results from 600°C, 120h, 5-turn inductor, 3×3 inch ground plane show a detectable frequency shift trend during the steady-state temperature hold. A downward frequency shift was observed over time, which is consistent with the increase in effective permittivity due to oxide formation.

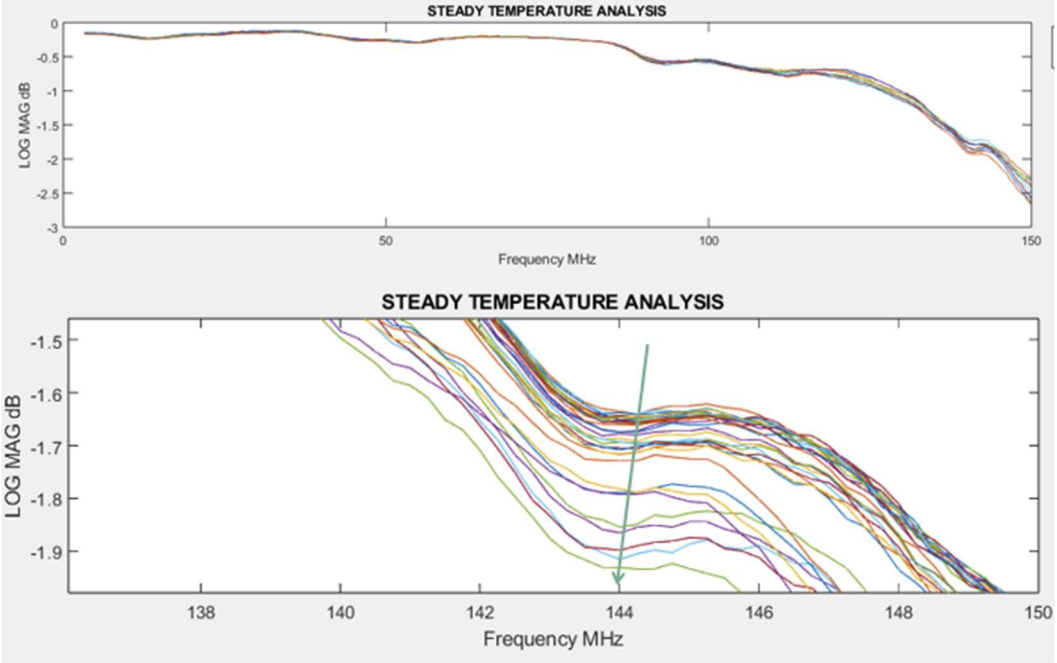

Figure 5.12. Experimental results of **Trial 3** steady temperature segment. The (top) figure displays the full spectrum, and the (bottom) figure displays a zoom on a small portion of the spectrum (136 MHz - 150 MHz) which was chosen because it contained the highest signal variation.

However, Figure 5.14, although averaging techniques were employed, the frequency response showed a more erratic pattern, suggesting possible external electromagnetic interference or variation in sensor contact. The inconsistencies in signal shape highlight the sensitivity of the system to small environmental or mechanical perturbations.

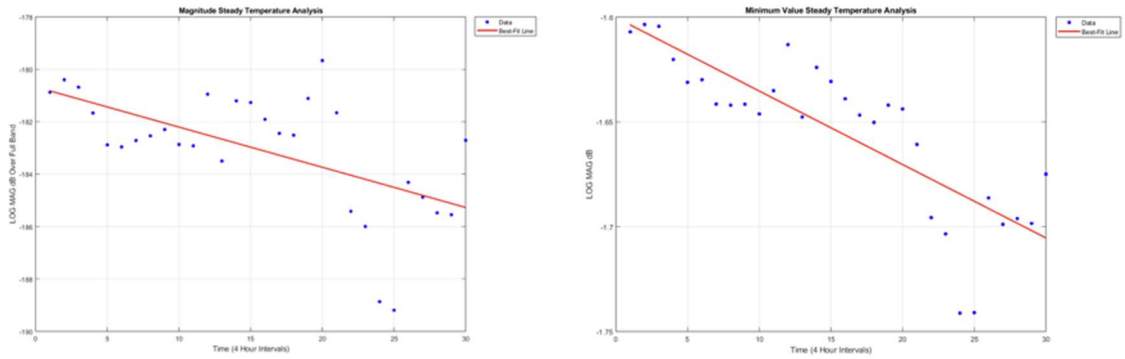

Figure 5.13. Experimental results of **Trial 5** steady temperature segment. The (left) figure displays the total magnitude over the wideband signal at every 4-hour time interval and its line of best fit, and the (right) figure displays the minimum over the wideband signal at every 4 hour time interval and its line of best fit.

Moving to 700°C in Trial 8, a more pronounced shift was recorded, as seen in Figures 5.13 and 5.14. In the first 40 hours, the resonant frequency shifted nearly twice as much as it did during the 600°C run, confirming that oxidation proceeds more aggressively at higher temperatures. Notably, after 40 hours and again after 80 hours, sudden jumps in the frequency curve suggest potential microstructural changes such as crack formation or sensor detachment due to thermal expansion mismatches.

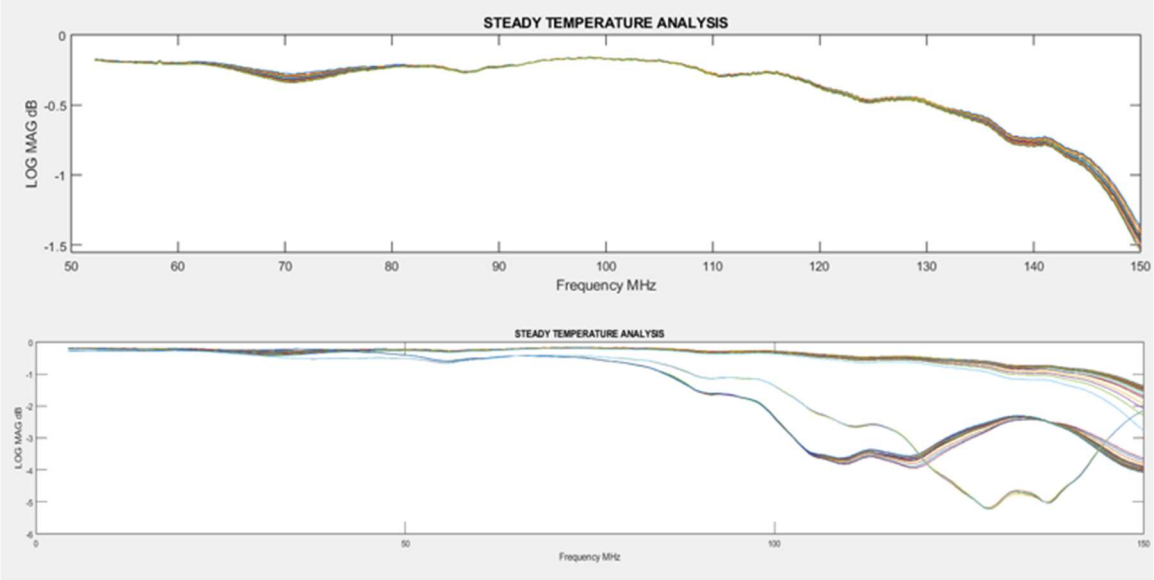

Figure 5.14. Experimental results of **Trial 8** steady temperature segment. The (top) figure displays the first 12 hours of the full spectrum, and the (bottom) figure the remaining 108 hours of captures for the full spectrum.

To better understand the relationship between the signal response and oxide growth, SEM imaging was conducted on the SS304H ground planes used in Trial 6. Figures 5.15 to 5.17 present SEM images at various magnifications. No distinct oxide layer was visible at the micron scale, supporting the conclusion that oxide growth remained in the nanometer range at 600°C. This limited visibility reinforces the importance of pushing testing to higher temperatures (800–1000°C) to ensure detectable oxide development for reliable sensor calibration.

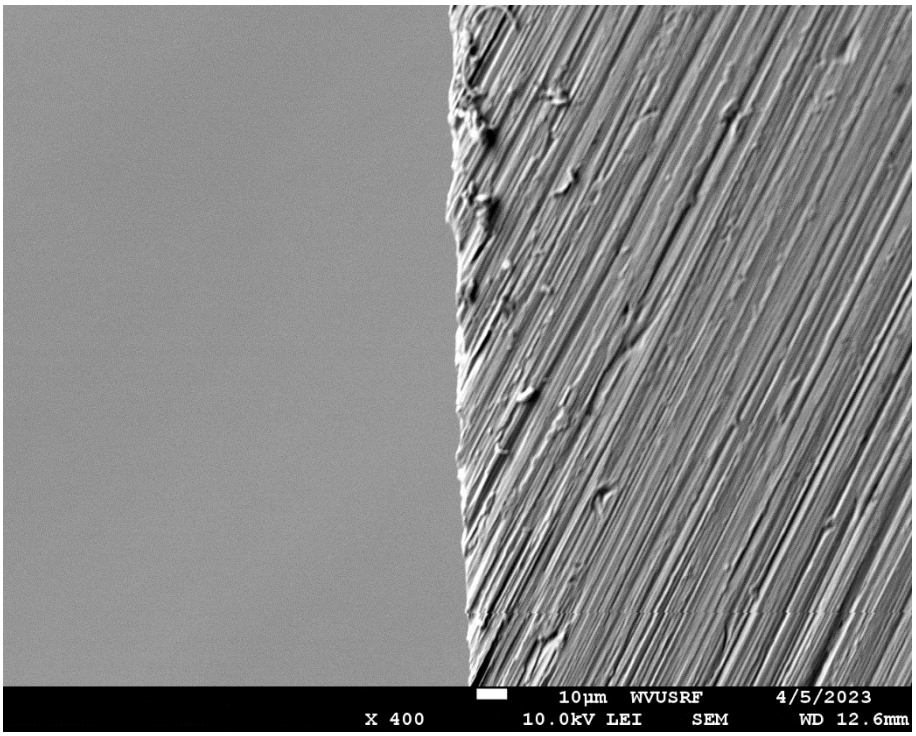

Figure 5.15: X400 magnification SEM image of corroded SS 304 H.

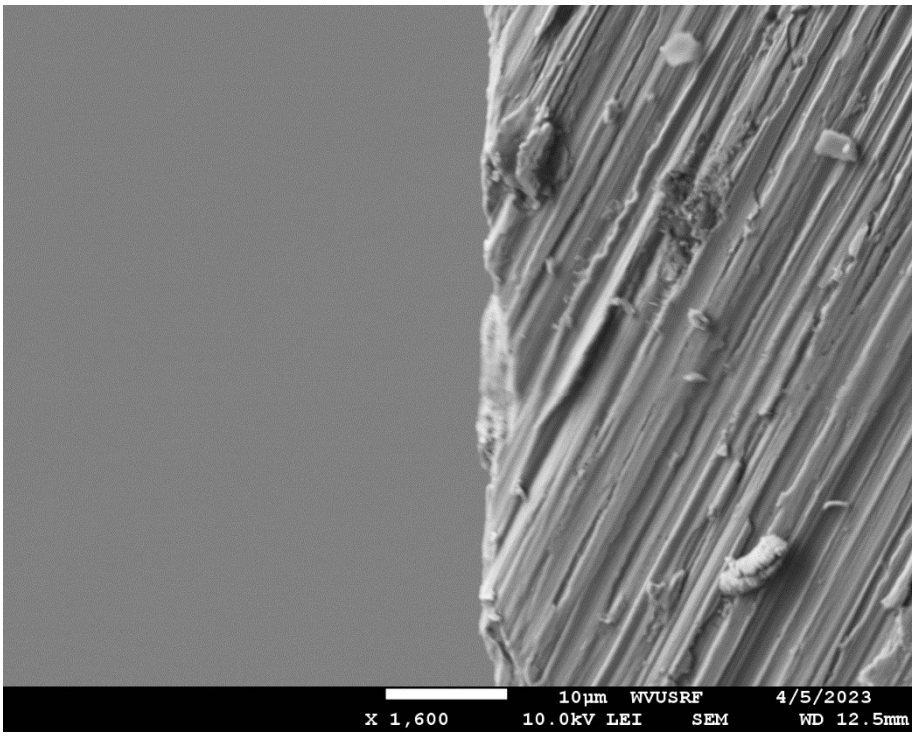

Figure 5.16. X1600 magnification SEM image of corroded SS 304 H.

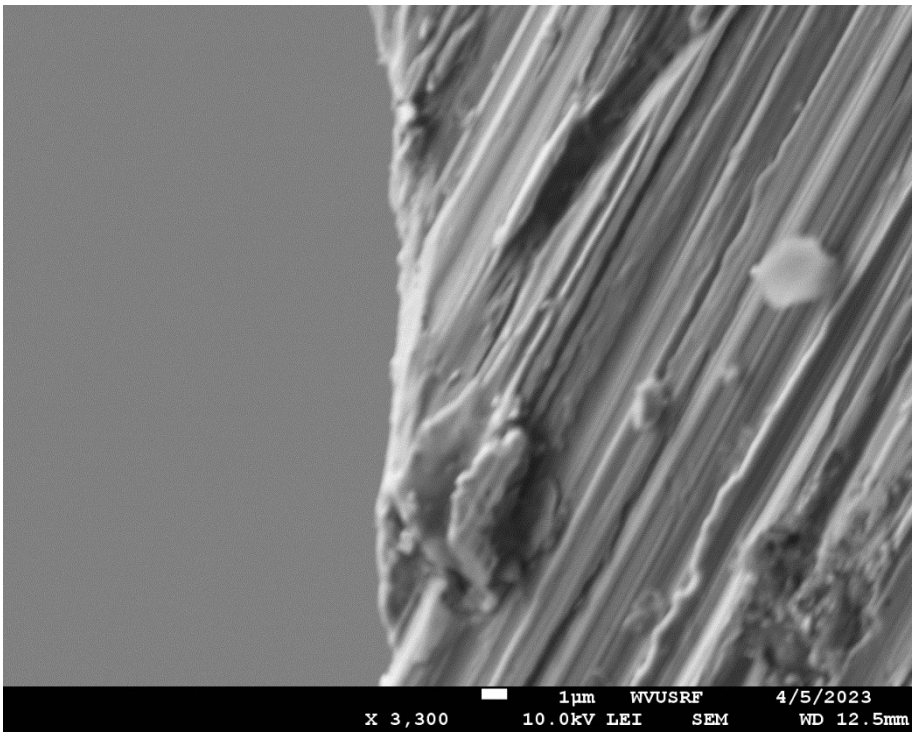

Figure 5.17: X3300 magnification SEM image of corroded SS 304 H.

5.4 Conclusions:

The combined results from Task 5.1 and Task 5.2 demonstrate significant progress in the development and validation of passive wireless LC sensors for through-wall temperature and corrosion monitoring in high-temperature environments. In Task 5.1, sensor/antenna configurations were systematically evaluated under low-temperature (≤500 °C) conditions using various metallic barriers, including galvanized steel, stainless steel, and aluminum. The observed severe signal attenuation across these barriers emphasized the challenges inherent in through-wall sensing applications and underscored the need for optimized sensor placement and design.

As a result, Task 5.2 focused on validating a novel sensing approach, in which the sensor is positioned on the opposite side of the metallic wall while still utilizing the metal as the ground plane. This approach avoids the need for direct through-metal interrogation, enabling real-time monitoring without exposing the antenna system to high temperatures. ANSYS simulations supported the feasibility of this configuration by predicting consistent resonant frequency shifts in response to oxide growth on the internal surface of the tube.

Experimental validation at elevated temperatures (600 °C and 700 °C) confirmed the trends anticipated by simulation. Trials using both 3-turn and 5-turn inductor designs exhibited frequency shifts over extended isothermal exposure periods, consistent with progressive oxide formation. In particular, Trial 6 demonstrated a smooth, quadratic trend in frequency response at 600 °C, while Trial 8 at 700 °C revealed accelerated signal shifts, confirming the sensitivity of the sensor to

temperature-induced oxidation. However, some trials also indicated signal instability and abrupt changes, which are likely attributed to antenna misalignment, sensor contact changes, or microstructural changes such as cracking or delamination at elevated temperatures.

Complementary SEM imaging of the SS304H ground planes verified that oxide layer growth at 600 °C remained within the nanometer scale, consistent with limited frequency shift magnitudes. These findings support the necessity of further testing at ≥800 °C to achieve oxide thicknesses sufficient for reliable, field-deployable sensor calibration.

Collectively, Tasks 5.1 and 5.2 validate a promising through-wall sensing strategy and provide foundational understanding of the sensor's electromagnetic behavior in obstructed, high-temperature environments. Future work will focus on extending tests to higher temperatures, refining sensor bonding methods, and further developing signal processing techniques to enhance accuracy, robustness, and field readiness of the system

Task 6: Project Implementation of Passive Wireless Sensor Arrays into Power Plant Demonstration

6.1 Introduction:

The goal of this task was to implement the technology into an actual application to monitor the high-temperature corrosion and cracking of the metal involved. The chipless RFID sensor was to be placed on the surface of the metal components provided by the plant collaborator, and most preferably, within a component of a coal power plant. The original proposal included had an interested coal plant to act as a partner in this project; the technology was going to be deployed within Longview Power Plant (just outside Morgantown, WV). Unfortunately, just after the submission of the project proposal, and during the start of the project (early 2020), Longview Power Plant declared bankruptcy due to economic pressures and the result COVID19. The contacts at the plant were removed, and approval for this demonstration of this technology within the plant was rescinded. Therefore, over the next years, a willing partner for the deployment of the technology was sought after. Through contacts on another DOE-NETL project, Calgon Carbon Corporation, with their materials processing plant in Neville Island, PA, agreed for us to install the passive wireless sensor within their plant. The plant has many high-temperature reactors and pipes that use similar stainless steels as coal power plants, and there would be various opportunities to install and monitor the metal components. The sensor system was then deployed into their plant onto a high-temperature cyclone separator along their regeneration production line for carbon black on May 7th, 2025. The system runs at temperatures in excess of >800 °C in air, and the system is exposed to the elements outside the building facilities. Follow-up reinstallations were completed after the project was completed (post-May 15th, 2025) due to various power and electronics issues; even though post-project, the results will be discussed in this report to show the team's dedication to the technology and given DOE project. More will be discussed and shown about the installation in the sections below.

6.2 Experimental Methods:

Previous testing of the sensors within WVU was completed using an g a Keysight Technologies N9918A 26.5 GHz FieldFox Microwave Analyzer (Santa Rosa, CA, USA) controlled with MATLAB R2023b (MathWorks, Natick, MA). For the demonstration within the industrial setting, and more compact and lower power (and cost) method of signal measurement was needed to deploy the technology. The engineering team replaced the control computer for the system with a small Raspberry Pi version 5 (4GB RAM model). The Keysight Technologies VNA was replaced using a NanoVNA V2 (S-A-A-2) is a 4GHz vector network analyzer (VNA) built/sold by HCXQS group (Nanjing, Jiangsu, China). This simple and inexpensive VNA (~$199) is capable of measuring antennas, filters, duplexers, and amplifiers. The VNA measurement and data storage was controlled by a custom program in Python. The entire system was connected to

a DC/DC step-down converter to a Shanqiu UPS system (Feixing Technology, Shenzhen, China) to ensure continuous powering during unexpected power interruptions.

The sensor installed was a similar 5-turn planar inductor (Ag-based print) onto an alumina dielectric plate, similar to that shown for the Cu corrosion testing shown in Task 4. The Ag-inductor was sandwiched between another alumina barrier plate to protect the sensor from the environmental elements. The interrogation antenna (same size as Cu demonstration in Task 4) was bonded and secured to the surface of this sandwich to hold it in position during the entire test. In an actual application, this antenna would be moved over the sensor to read the current state of the metal corrosion, but in this case, we wanted to get a long-term continuous reading of the sensor in the current environment. All the electronics were adhered to the wall of a Craftsman tool box, and strapped to the safety protection fence on the outside of the high-temperature cyclone (at the top of the cyclone roof on the top of the four-story stack).

The interrogator antenna was connected to the VNA via a SMA coaxial connector. To ensure continuous monitoring, a small, router-style UPS capable of supplying 12 A at 2 V was used to the unit. The power was stepped down using a buck converter to 5 V at 5 A, which the Raspberry Pi requires to ensure power delivery to all peripherals. Sweeping parameters are configured in a GUI on the Raspberry Pi. The frequency sweep is logged to a USB drive (and/or local memory) as a CSV file.

The measurement frequency sweep was 50 and 125 MHz. The step size was set to 101 points calculated at sweep time (Stop_Hz - start_Hz) / (points - 1). The parameters measured were the S11 (reflection coefficient) and S21 (transmission coefficient), both magnitude (dB) and phase (degrees). Each measurement sweep took 101 readings, which were later averaged for each reading.

6.3 Results and Discussion:

As described above, the passive wireless sensor was installed initially on May 7th, 2025. Figure 6.1 shows a picture of Dr. Edward Sabolsky installing the sensors on the roof of the cyclone at Calgon Carbon. One item that should be noted, the picture shows the general high corrosion level that already existed on the cyclone. This was true for all components within the area of the high-temperature reactor. The company did not have plans to replace any metal parts in this area for us to attach to a virgin stainless steel part. The team found a location with the least corrosion level to install the sensor in order to at least monitor continued corrosion and cracking of the metal layers. In addition, it must be noted that most components in this plant, and other industrial and energy plants approached in this work, indicated that many of their piping and components were already coated with corrosion protection, personnel protection, and/or thermal insulation. This must be noted, so that other researchers doing work in this area must attempt to reserve the installation of the sensor during a rebuild or installation of a new metal component (to access virgin metal surfaces). Figure 6.2 shows an optical picture of the placement of the sensor on the roof of the cyclone, and then Figure 6.3 shows an optical picture of other alumina fiber insulation and refractory brick placed around the sensor to protect the coaxial cable running to the interrogator

antennae (and to physically hold the whole sensor in place so it does not get blown off the top of the cyclone). Again, this sensor is installed on the roof of the cyclone which is on the fourth story of the reactor tower.

One issue with the installation, that was not previously considered, is that the sensor installation would be within a system that would be exposed to environmental elements and weather. The entire electrical system needed to be enclosed within a sealed box (except for the sensor) and the seal needed to be secured to the cyclone roof (to ensure it would not be blown off the roof of the reactor). The project attempted to develop a method to secure the sensor to the corroding metal in Task 3, but issues due to thermal expansion (CTE) mismatch and sintering shrinkage issues (during initial thermal bonding) limited final chemical bonding to the metal. In the end, physical pressure was applied to the sensor at this point with refractory bricks to hold in place. Future work should focus on welded clips or frames to secure the sensor into place, but permanent bonding to the metal will lead to continuous issues with sensor delamination due to CTE mismatch. In retrospect, this seems obvious at this point, but during the proposal writing, it seemed plausible to bond this sensor onto the metal with a perfectly CTE matched glass, glass/metal composite, and/or metal braze. The failure of many experiments aligned with this bonding can be reviewed in the initial reports in year 1. Also as discussed above, weather proved to be an issue, since many of these energy and industrial plants include significant components outside, which the student teams all worked on technologies in the indoor laboratories. The large wind and rainstorms throughout May and June 2025 caused timing issues for installation and operation of the sensor system (power outages).

Figure 6.1: Picture of Dr. Edward Sabolsky (PI) installing the sensor on the roof of the material cyclone at Calgon Carbon plant in Neville Island, PA on May 7th, 2025.

Figure 6.2: Picture of the packaged sensor with embedded interrogator antenna connected to a coaxial cable connected by an SMA connector to the nano-VNA (that is out of picture view).

Figure 6.3: Picture of sensor embedded under ceramic tiles to protect against the weather elements, and alumina fiber insulation to protect the coaxial cable from touching the metal cyclone surface (insulation brick pieces just used to hold all parts from moving due to wind).

The sensor operated on the cyclone for one month and the initial sensor was de-installed and data pulled from the system on June 6th, 2025. The data was reviewed for this initial installation and showed that the multiple power outages from the fierce storms have disrupted the data acquisition. No continuous data was recorded. In addition, the power cables were melted due to the excessive heat during the run. The system was returned to WVU for one month (July 2025), and the entire sensor system was re-engineered. This included more thermal insulation was placed around the coaxial cables, a new UPS system was installed to deal with future electrical disruptions, and all electronics were wall mounted within the electrical box (to ensure protection against electrical box flooding, which was also identified as an issue in initial demonstration).

The system was supposed to be re-installed on July 15th, 2025 into the same location at Calgon Carbon. Calgon needed to shut down the entire system before this reinstallation of the sensor. The cyclone is currently being re-furbished, and the reinstallation has been pushed back to late-August or early-September 2025. The demonstration will be more applicable in this case, since the location of installation will be set against a new wall/roof of the cyclone, since this steel is currently being replaced. The entire system is ready to be installed once notified by the plant manager.

6.4 Conclusions:

The transition from laboratory testing and demonstration to actual industrial real-life testing was experienced by the student team. The unexpected effects of environment and extrinsic effects on the sensor system were experienced first-hand by the entire team. The initial demonstration attempt was shown to be a failure due to the weather, electrical outages, and temperature near the electronics. Further optimization of the system was completed by the team after the projects end, and the team was insistent to complete a successful deployment of the system they worked hard on for the entire project. The sensor system was planned to be re-deployed into the same location in July, but the team is waiting on permission by plant managers to attach to the new cyclone

GRAPHICAL MATERIALS LIST(S):

None

REFERENCES:

[1] Racasan, A.; Munteanu, C.; Topa, V.; Pacurar, C.; Hebedean, C.; Lup, S. Advances on Parasitic Capacitance Reduction of Emi Filters. *Ann. Univ. Craiova Electr. Eng. Ser.* **2010**, *34*, 220–223.

[2] Müller, J.E.; Ablassmeier, U.; Schelle, J.; Kellner, W.; Kniepkamp, H. Design of Planar Rectangular Microelectronic Inductors. *Integr. Circuits Wirel. Commun.* **1998**, *2*, 581–584.

[3] Havel, A.; Borski, M.; Spicka, J.; Tvrdon, M. The Boost Converter with Air Core Coil. In Proceedings of the 2014 15th International Scientific Conference on Electric Power Engineering (EPE), Brno, Czech Republic, 12–14 May 2014; IEEE: Piscataway, NJ, USA, 2014; pp. 559–562.

[4] Kopp, M. *An Introduction to HFSS: Fundamental Principles, Concepts, and Use*; Ansys Inc.: Canonsburg, PA, USA, 2009.

[5] Mrowec, S.; Stokłosa, A. Oxidation of Copper at High Temperatures. *Oxid. Met.* **1971**, *3*, 291–311.

[6] X. Zheng, Y. Sakurai, Y. Okayama, T. Yang, L. Zhang, X. Yao, K. Nonaka, and C. Xu, "Dielectric measurement to probe electron ordering and electron-spin interaction," Journal of applied physics, vol. 92, no. 5, pp. 2703–2708, 2002.

[7] L.-Y. Chen, "Dielectric performance of a high purity htcc alumina at high temperatures-a comparison study with other polycrystalline alumina," Addi tional Papers and presentations, vol. 2014, no. HITEC, pp. 000271–000277, 2014.

[8] L.-Y. Chen and G. W. Hunter, "Temperature dependent dielectric properties of polycrystalline 96% al2o3," MRS Online Proceedings Library (OPL), vol. 833, pp. G7–6, 2004.

[9] P. Thongbai, T. Yamwong, and S. Maensiri, "Correlation between giant dielectric response and electrical conductivity of cuo ceramic," Solid state communications, vol. 147, no. 9-10, pp. 385–387, 2008.

[10] Tylecote, R.F. The Oxidation of Copper at 350–900 °C in Air. *J. Inst. Met.* **1950**, *78*, 327–350.

[11] Baur, J.P.; Bridges, D.W.; Fassell, W.M. Oxidation of Oxygen-Free High Conductivity Copper to Cu_2O. *J. Electrochem. Soc.* **1956**, *103*, 273.

[12] Park, J.H.; Natesan, K. Oxidation of Copper and Electronic Transport in Copper Oxides. *Oxid. Met.* **1993**, *39*, 411–435.

[13] Zhu, Y.; Mimura, K.; Isshiki, M. A Study of the Initial Oxidation of Copper in 0.1 MPa Oxygen and the Effect of Purity by Metallographic Methods. *Corros. Sci.* **2004**, *46*, 2445–2454.

[14] Zhu, Y.; Mimura, K.; Isshiki, M. Oxidation Mechanism of Cu_2O to CuO at 600–1050 °C. *Oxid. Met.* **2004**, *62*, 207–222.

[15] Grabke, H.J. Segregation and Oxidation. Presented at the Thursday Evening Talk at Gordon Research Conference on High Temperature Corrosion, New London, NH, USA, 20–25 July 2003.

[16] Shima, Y.; Ishikawa, Y.; Nitta, H.; Yamazaki, Y.; Mimura, K.; Isshiki, M.; Iijima, Y. Self-Diffusion along Dislocations in Ultra High Purity Iron. *Mater. Trans.* **2002**, *43*, 173–177.

[17] Schramm, L.; Behr, G.; Löser, W.; Wetzig, K. Thermodynamic Reassessment of the Cu-O Phase Diagram. *J. Phase Equilibria Diffus.* **2005**, *26*, 605–612

[18] Khanna, Anand S. "High temperature oxidation." *Handbook of environmental degradation of materials*. William Andrew Publishing, 2005. 105-152.

[19] M. Huntz, A. Reckmann, C. Haut, C. Severac, M. Herbst, F. C. T. Resende and A. C. S. Sabioni, Material Science and Engineering A 447, 266 (2007).

[20] M. Jepson, PhD thesis, Loughborough University, Loughborough, (2008).

[21] R. Guillamet, J. Lopitaux, B. Hannoyer and M. Lenglet, Journal of Physics IV 3, 349 (1993).

[22]. E. R. de Carvalho, G. M. da Costa, A. B. Cota and E. H. Rossi, Material Research Bulletin 9, 393 (2006).

[23] N. Karimi, F. Riffard, F. Rabaste, S. Perrier, R. Cueff, C. Issartel and H. Buscail, Applied Surface Science 254, 2292 (2008).

[24] C. Wagner, Atom Movements, (American Society for Metals, Cleveland, 1953), p. 153.

[25] Strader, Noah, et al. "Near-field passive wireless sensor for high-temperature metal corrosion monitoring." *Sensors* 24.23 (2024): 7806.

[26] Huntz, Anne Marie, et al. "Oxidation of AISI 304 and AISI 439 stainless steels." *Materials Science and Engineering: A* 447.1-2 (2007): 266-276.

[27] Lussana, Danilo, et al. "Thermodynamic and kinetics aspects of high temperature oxidation on a 304L stainless steel." *Oxidation of metals* 81 (2014): 515-528.

[28] Yoo, Keun-Bong, et al. "Study of the scale formed on super 304H boiler tube steels after long-term steam oxidation at high temperatures." *Materials Characterization* 146 (2018): 71-80.

[29] Strader, N., Jordan, B. R., Bilac, O., Tennant, K. M., Reynolds, D. S., Sabolsky, E. M., & Daniszewski, A. C. (2024). Near-field passive wireless sensor for high-temperature metal corrosion monitoring. Sensors, 24(23), 7806.

BIBLIOGRAPHY

None

LIST OF ACRONYMS AND ABBREVIATIONS

SEM	Scanning Electron Microscopy
Ag	Silver
SS304H	Stainless Steel 304H
Cu	Copper
Pt	Platinum
Al_2O_3	Aluminum Oxide
ε	Dielectric Constant
OM	Optical Microscope
ε_0	Permittivity of Free Space
WSN	Wireless Sensor Network
C:	Capacitance
C_p	Capacitance in parallel
L_p	Inductance in parallel
T	Temperature (℃)
σ	Electrical Conductivity
n	Number of Electrodes
f_r	Resonant Frequency
w	Finger width of capacitor/inductor
w	Inductor line width
d_{in}	Inner diameter of the planar inductor
d_{out}	Outer diameter of the planar inductor

APPENDICES

List of Publications:

1. Strader, N., Jordan, B. R., Bilac, O., Tennant, K. M., Reynolds, D. S., Sabolsky, E. M., & Daniszewski, A. C. (2024). Near-field passive wireless sensor for high-temperature metal corrosion monitoring. *Sensors*, *24*(23), 7806.
2. Near-Field Passive Wireless Sensor Realized by Pt Electrodes for High-Temperature Corrosion Monitoring and Hars Environment Applications. The article will be submitted to the journal Sensors (MDPI) in September 2025.

List of Presentations:

1. O. Bilaç, N. Strader, K. Tennant, W. Bullock, J. Herter, B. Jordan, D. Reynolds, K. Sabolsky and E. Sabolsky, " Near-Field Passive Wireless Sensor for High-Temperature Metal Corrosion Monitoring", Oral presentation at the Materials Science & Technology 2024 (MS&T'24), October 6-9, 2024
2. B. Jordan, N Strader, D Reynolds, E. M. Sabolsky. "Passive Wireless Sensors for Temperature and Corrosion Monitoring of Coal Boiler Components under Flexible Operation". Oral presentation at the Materials Science & Technology 2022 (MS&T'22), Pittsburgh, PA, October 9th - 12th, 2022
3. B.R. Jordan, K. Sivaneri, E. M. Sabolsky and D. Reynolds "High Temperature Corrosion Sensors for Boiler Grade Stainless Steel in Power Plants," Oral presentation at the Material Science and Technology 2021 (MS&T21) Virtual meeting, October 17-20, 2021.

List of Students and Post-docs Supported by This Project:

- Oguzhan Bilac (Post-doc)- Studied June 2024- May 2025
- Brian Jordan (PhD)- Studied Sept. 2020- May 2025
- Noah Strader (MS)- Graduated May 2024
- Kevin Tennant (MS)- Graduated May 2024
- Javier Antonio Mena Arenas (Ph.D)- Graduated Aug. 2024
- K.S. Varadharajan Idhaiam (PhD) - Graduated May 2022
- Rex Elliot McAllister (Undergraduate)- (expected graduation May 2027) Studied Jan. 2025-May 2025
- William Bullock (Undergraduate)- Graduated May 2025
- Andrew Gautier (Undergraduate)- Graduated May 2025
- Nathaniel Patrick O'Brien (Undergraduate)- Graduated May 2025
- Joshua Caswell (Undergraduate)- Graduated May 2024
- Zachary Lynch (Undergraduate)- Graduated Jan. 2021
- Samuel Alexander Swestock (Undergraduate)- Graduated May 2023
- Derek Joseph Hockenberry (Undergraduate)- Graduated May 2022